STUDIES OF UNUSUALLY GAS-RICH GALAXIES IN ALFALFA AT BOTH ENDS OF THE MASS SPECTRUM

A Dissertation

Presented to the Faculty of the Graduate School

of Cornell University

in Partial Fulfillment of the Requirements for the Degree of

Doctor of Philosophy

by

Gregory Lewis Hallenbeck

August 2014

© 2014 Gregory Lewis Hallenbeck
ALL RIGHTS RESERVED

STUDIES OF UNUSUALLY GAS-RICH GALAXIES IN ALFALFA AT BOTH ENDS OF THE MASS SPECTRUM

Gregory Lewis Hallenbeck, Ph.D.

Cornell University 2014

I present two major investigations enabled by the sensitivity and volume of the ALFALFA survey: one of dwarf early-type dwarfs (ETDs) in the Virgo Cluster, and the other of the high HI mass, gas-rich HIghMass sample.

The Virgo Cluster contains hundreds of ETDs, which are mostly red, non-starforming, and relatively gas-free galaxies. According to standard evolutionary scenarios, most such galaxies are the result of the stripping of faint late-type dwarfs which fall onto the cluster. These galaxies have their gas removed, and eventually cease forming new stars. However, ALFALFA has detected 6 ETDs which are both as gas-rich as a typical dwarf irregular or blue compact dwarf but which have the star formation properties of a typical 'red and dead' ETD. I investigate possible explanations for this population of galaxies: that they are infalling unstripped galaxies, that they are dwarfs with 'bursty' star formation between phases of star formation, that their gas is recycled, and that their gas is newly reaccreted. I argue that the properties of these ETDs are most consistent with gas reaccretion.

Observationally, it is observed that galaxies with higher stellar masses are the most efficient at forming stars from their gas, and thus tend to have lower gas fractions (M_{HI}/M_*). This is in agreement with both the semi-analytic theory of hierarchical clustering and the 'down-sizing' found observationally. However, in ALFALFA we have identified a sample of 34 galaxies which have both high stellar masses and high gas fractions for their stellar masses, which we call HIghMass. I present an in-depth study of two of these galaxies, UGC 9037

and UGC 12506, using high-resolution HI observations obtained at the Very Large Array. UGC 9037 has very high HI surface densities and strong non-circular motions, and appears to be a galaxy in transition, and will go through a period of heightened star formation in the near future. UGC 12506 has very low surface densities for its HI mass, and is stable kinematically, making it a prime candidate for a galaxy which has intrinsically high dark matter halo spin. I also present preliminary results for the combined HI and H_2 for three additional HIghMass galaxies, but no firm conclusions are drawn.

BIOGRAPHICAL SKETCH

Gregory Lewis Hallenbeck was born in 1985 in Rochester, New York. As a toddler, his crowning achievement was completing puzzles with more than four pieces. He soon grew toward more noble pursuits, mostly surrounding the NES games Contra, Super Mario Brothers 3, and Final Fantasy. As a boy, he looked at the sky one time, which qualified him to become an astronomer.

He attended Carnegie Mellon University where he majored in physics and statistics, but pretty much spent all of his time trying to avoid doing work and instead spent his time playing games. One time he got onto the tension grid in the Fine Arts building, but don't let the administration know that.

In 2008, Gregory was accepted into the physics department at Cornell, which he applied to because he didn't know that the astronomy department was separate. This has generally been hailed as a 'good move' on his part by everyone he has informed of this mistake. He joined the Extragalactic Group led by Professors Haynes and Giovanelli, where he remains as of this writing.

In the fall, Gregory will be a visiting assistant professor at Union College in Schenectady New York, whose illustrious graduates include John Lewis Hallenbeck (father), Lewis Hallenbeck (grandfather), and Johnson Potter Hallenbeck (great grandfather).

To everyone else who has to write a thesis.

"They tried and failed, all of them?"
"Oh no." She shook her head. "They tried and died."
—Frank Herbert, *Dune*

ACKNOWLEDGEMENTS

Martha and Riccardo, thank you for taking in a physicist and teaching him to be a proper astronomer.

Mom and Dad, I'm not great with specifics, but you two were pretty great parents. You let me do whatever I was passionate about, and now you have the embarrassment of having an astronomer for a son.

Ruth, you are basically the best, and thank you for always supporting me when I am ready to give up (which is more or less always).

Dorothy, I haven't charged you for the utilities in our apartment for a year. You owe me like $300. Also, thanks for being my best friend for the past ten years.

Ann, Betsey, and Manolis, the three of you were my role models as graduate students. It was quite helpful to have some senior students to look up to.

Luke and Mike, you two have enabled me to work in an office where I both have company but can pretend that I'm alone whenever I want.

The Author of the Apocryphal Book of Enoch, you have given me more to talk about at parties than pretty much anything else.

TABLE OF CONTENTS

LIST OF TABLES

LIST OF FIGURES

CHAPTER 1

INTRODUCTION

Substantial reservoirs of hydrogen gas are necessary to fuel star formation in galaxies. Such star formation follows a broadly understood process of atomic hydrogen (HI) cooling to form molecular hydrogen (H_2), which eventually collapses into new stars. It is thus natural to assume that there should exist a significant link between the HI mass, tracers of star formation, and the stellar masses of galaxies. However, the reality is not so simple. Catinella et al. (2010) propose a "gas fraction plane," defining scaling relations between three global galaxy observables: stellar mass surface density (μ_*), colors (NUV$-r$), and HI gas fraction (M_{HI}/M_*). However, while the overall trends are well defined, there remains significant scatter among individual galaxies. Predicted gas fractions have typical scatter of ~ 0.3 dex. Such scatter exists even after taking into account the variation due to environmental differences and interactions with neighboring galaxies (Cortese et al. 2011).

Why do galaxies deviate? Perhaps there are unaccounted-for internal factors which regulate the conversion of HI into H_2 and finally into stars, such as the dark matter halo spin parameters (Peebles 1971). Alternatively, perhaps there are alternate, uncommon mechanisms at work, such as recent accretion of gas or ways of merging galaxies without exciting star formation. My goal is to understand populations of galaxies which strongly deviate from such global scaling relations, specifically those that have much higher HI gas fractions than their optical properties would suggest. Understanding how, why, and how frequently galaxies deviate can then help us understand the origin of this large gas fraction scatter.

Such a study would not be possible without the recent advances of the ALFALFA survey (Arecibo[1] Legacy ALFA; Giovanelli et al. 2005) over previous blind HI surveys. ALFALFA

[1]The Arecibo Observatory is operated by SRI International under a cooperative agreement with the National Science Foundation (AST-1100968), and in alliance with Ana G. Mndez-Universidad Metropolitana,

is a wide-area ($\approx$ 7000 deg^2, or $\sim$ 1/6 of the sky) blind[2] survey searching for galactic and extragalactic sources of HI out to a distance of approximately 260 Mpc. The ALFALFA survey began in 2005 and observations completed in the fall of 2011; data reduction is still ongoing.

1.1 ALFALFA at Both Ends of the Mass Spectrum

Before ALFALFA, the state of the art wide-area blind HI survey was HIPASS (HI Parkes All-Sky Survey; Barnes et al. 2001), which utilized the 13 beam 21 cm Multibeam receiver on the Parkes 64m telescope. HIPASS detected a total of 4315 extragalactic sources over $\sim$ 21000 deg^2 of sky, or 0.2 sources/deg^2 out to a nominal maximum distance of $\sim$ 180 Mpc.[3] The later "Northern HIPASS" catalog of Wong et al. (2006) extends the survey to declinations $\delta < 25°30'$ and adds an additional 1002 sources (but does maintains roughly the same source density).

While a 305 m dish naturally gives Arecibo a much higher sensitivity than the 64 m Parkes dish, Arecibo's single pixel receiver (compared with the 13 beam receiver at Parkes) meant that mapping a large area of sky was impractical. The addition of the 7 beam ALFA (Arecibo L-Band Feed Array) receiver to Arecibo enabled a great increase in the speed at which the sky could be mapped in comparison with previous surveys at Arecibo, such as the ADBS (Arecibo Dual-Beam Survey; Rosenberg and Schneider 2000). Shortly thereafter, ALFALFA, an ambitious 4000 hour $\sim$7000 deg^2 survey wide-area blind HI survey, commenced. As of this writing, the most recent public data release covering approximately 40% of the final sky

and the Universities Space Research Association.

[2]A blind survey scans the sky looking for whatever sources may be there, rather than targeting specific, previously known sources.

[3]For a survey of a spectral line, such as HI, the nominal redshift coverage is dictated by the bandwidth of the receiver

area ($\alpha.40$; Haynes et al. 2011), ALFALFA has detected 15041 extragalactic sources. The data release covers 2800 deg^2, meaning that ALFALFA detects roughly 5.4 sources/deg^2.

Compared with HIPASS, the source density of ALFALFA is 27 times higher. Two major factors which contribute to this large improvement include the sensitivity of Arecibo (and thus the ALFALFA survey), and the cosmologically representative volume probed by ALFALFA.

1.1.1 Sensitivity and Low Mass Galaxies

At all distances from Earth, ALFALFA is capable of detecting fainter signals than HIPASS (for a comparison, see Martin et al. 2010, Figure 12). This high sensitivity allows us to probe fainter, less HI-massive galaxies. Recently, the ALFALFA source extraction team[4] discovered a previously unknown low-mass ($M_{HI} \sim 10^6$) galaxy near the edge of the local group, Leo P (Giovanelli et al. 2013; Rhode et al. 2013; Skillman et al. 2013; McQuinn et al. 2013). Efforts are underway to find even less massive so-called ultra faint dwarf satellite galaxies to our own Milky Way using the ALFALFA data cubes; such work can be found in the catalog of Adams et al. (2013). Out to a few Mpc, ALFALFA detects a substantial population of galaxies with HI masses in the range of $10^6 < M_\odot < 10^7$, including the 12 galaxies of the ALFALFA follow-up program SHIELD (Survey of HI in Extremely Low-Mass Dwarfs; Cannon et al. 2011; McQuinn et al. 2014).

Further beyond the local group, even ALFALFA is not sensitive enough to detect such low mass galaxies. The nearest rich cluster to the Milky Way is Virgo ($d \sim 17$ Mpc), with over 1000 known members. At the distance of the Virgo Cluster, the earlier HIJASS (HI

[4]Riccardo.

Jodrell Bank All Sky Survey; Davies et al. 2004), had a detection limit of $10^{7.7}$ $M_\odot$ (for a velocity width of 50 km s^{-1}), although it only covered a small fraction of the cluster's total area. ALFALFA's detection limit, for a galaxy with the same velocity width, is $10^{7.4}$ $M_\odot$, and is thus a factor of two improvement.

Included in the ALFALFA detections in Virgo, but below the sensitivity of the HIJASS survey, are 6 gas-bearing red dwarf ellipticals in the Virgo Cluster. Such galaxies appear, from their optical properties, to be "red and dead," and are not expected to contain any significant reservoir of gas. Other, deeper HI surveys of the Virgo cluster exist, but are either specifically targeted surveys of gas-rich (Hoffman et al. 1987) and gas-poor galaxies (Haynes and Giovanelli 1986; Huchtmeier and Richter 1986; van Driel et al. 2000; Conselice et al. 2003), or cover only a small region of the Virgo Cluster (Taylor et al. 2012; Taylor et al. 2013) and thus this sample has not been identified prior to the ALFALFA observations of the Virgo Cluster (Giovanelli et al. 2007; Kent et al. 2008; Gavazzi et al. 2008).

1.1.2 Volume and Rare, High Mass Galaxies

The total HIPASS survey (the original plus northern extension) covers a much larger sky area than even the final ALFALFA footprint will. It covers the sky at declinations of $\delta < 25°30'$ (total area of $\sim$ 29000 deg^2), while ALFALFA covers portions of the spring and fall sky between $-2° < \delta < 38°$ (total area of $\sim$ 7000 deg^2). However, the volume of the surveys probed is quite different. HIPASS nominally detects galaxies out to 180 Mpc, but the comparatively low sensitivity of HIPASS is such that very few galaxies are actually detected even at 100 Mpc, and so the practical volume is lower than this maximum might suggest. ALFALFA, on the other hand, detects many galaxies out to its limit of 260 Mpc. The ratio of volumes sampled is thus approximately $V_{\rm HIPASS}/V_{\rm ALFALFA} \sim \frac{1}{6}$. Any particular source can

only be detected out to a certain distance, beyond which it is too faint, and thus "total survey volume" is a poorly defined quantity. However, this larger volume makes ALFALFA much less biased by the local large scale structure and cosmic variance when deriving statistical measures of the global population, such as the HI mass function (Martin et al. 2010), the baryonic mass function (Papastergis et al. 2012), velocity width function (Papastergis et al. 2011), and the correlation function (Papastergis et al. 2013), which measures the clustering of galaxies.

In addition, a large volume makes ALFALFA capable of finding rare objects. The most HI-massive galaxies are also extremely rare objects. The HIPASS survey detects 231 objects with $M_{HI} > 10^{10}$ $M_\odot$ (or $\sim 0.01/deg^2$), compared with the 1916 ALFALFA detects in $\alpha.40$ (or $\sim 0.7/deg^2$). As a consequence, Zwaan et al. (2005), using HIPASS, infer an order of magnitude fewer extremely massive $M_{HI} > 10^{10}$ $M_\odot$ galaxies compared with ALFALFA (Martin et al. 2010).

Among these HI-massive ($> 10^{10}$ $M_\odot$) galaxies, we identify a smaller sample which also have unusually high gas fractions (GF$\equiv M_{HI}/M_*$) for their stellar masses. Some even have $GF > 1$, which is only typical for galaxies with stellar masses at least two orders of magnitude lower. These galaxies we call the HIghMass sample. Optically they appear to be "normal" spiral galaxies, and have star formation rates typical for their stellar masses.

1.1.3 Summary

This dissertation presents two ongoing investigations, motivated as described above. Both involve galaxies which appear optically normal, but strongly deviate from established trends of HI gas fractions. They also sit at opposite ends of the HI mass spectrum, and together

require a survey with both high sensitivity and volume, like ALFALFA, to be selected by their HI properties. First, I focus on very low HI mass dwarf galaxies in the Virgo cluster. While they have low HI masses, they have extremely high HI masses for red, low stellar mass galaxies. From their HI and stellar masses alone, indistinguishable from gas-rich, star-forming dwarf irregulars. I then consider objects at the other end of the mass scale: massive galaxies, similar to the Milky Way in stellar mass but with high HI masses for their stellar masses. Such galaxies are so rare that only 34 are detected in the 2800 deg^2 footprint of ALFALFA's α.40 catalog.

1.2 Overview of the Thesis

In Chapter 2, I present the results of research on the gas-bearing ETDs in the Virgo cluster, previously published in Hallenbeck et al. (2012). That chapter is a self-contained investigation, from sample selection to final conclusions. In it, I consider in what ways their optical and HI properties compare with other populations of dwarf galaxies in the Virgo cluster. This chapter also includes discussions about four possible histories for these galaxies: that they are in the process of being stripped, that the galaxies are experiencing highly stochastic star formation, that their gas is recycled, and that the gas has been recently accreted.

Chapters 3–6 present the work I have done so far on the HIghMass sample (Hallenbeck et al. 2014). These chapters represent a substantial body of work, but more work remains to be done. Chapter 3 briefly motivates the selection of the HIghMass galaxies, places them within the larger context of all ALFALFA detected galaxies, and gives an overview of the HIghMass team's observing strategy. In Chapter 4, I present the data pipeline and data reduction techniques used to analyze high resolution radio observations of the HI and H_2 gas

in the HIghMass galaxies.[5] These include a novel method for measuring the dark matter halo spin parameter (λ) observationally.

Chapter 5 presents the in-depth study of the HI in two of the HIghMass galaxies, and represent the first two galaxies to be completed via the pipeline discussed in Chapter 4. These two galaxies are massive even among the HIghMass galaxies (with $M_{HI} > 10^{10.5}$ $M_{\odot}$). While they appear very similar to each other optically, the details of their HI distributions and kinematics prove to be quite different, and demonstrate the substantial range of possible origins across the HIghMass sample. However, for these two galaxies, only their HI has been observed.

In Chapter 6, I present the results for three additional HIghMass galaxies: UGC 6168, UGC 7899, and NGC 5230. These galaxies have both resolved HI and H_2 observations. Thus, we can probe not only the kinematics and dark matter properties of these galaxies, but also the link between HI, H_2, and star formation more closely.

The last chapter, Chapter 7, presents future directions for both the dwarf elliptical and HIghMass projects. For the dwarf ellipticals, I present new avenues for inquiry beyond the existing ALFALFA HI, optical, and ultraviolet observations. Much of the future work for the HIghMass galaxies is self-evident: less than half of the data reduction is complete for the resolved HI observations. However, there are several ways that the data pipeline can be improved, and new analysis tools which can be developed, which I discuss in Chapter 7.

[5] A more technical discussion of these techniques can be found in Appendix A.

CHAPTER 2

GAS-RICH DWARF ELLIPTICALS IN THE VIRGO CLUSTER

2.1 Introduction

Dwarf ellipticals (dEs)[1] are rare in the field and in galaxy groups, but are the most common galaxies in clusters (Binggeli et al. 1985; Caldwell 1987; Trentham and Tully 2009). An ongoing question is whether cluster dEs form in situ, or whether the cluster environment strips infalling late-type galaxies of their gas, transforming them into dEs (Tully and Shaya 1984; Boselli and Gavazzi 2006; Boselli et al. 2008a). Driving this evolution are such processes as ram-pressure stripping (Gunn and Gott 1972), starvation (Larson et al. 1980), and galaxy harassment (Lin and Faber 1983). There is significant evidence that at least some subset of the dwarf elliptical population were once late-type galaxies. In the most luminous of early-type dwarfs (ETDs), late-type features such as stellar disks and faint spiral arms can be observed (Lisker et al. 2006b). Furthermore, rotational support or even rotational flattening is observed in a significant fraction of ETDs (van Zee et al. 2004; Beasley et al. 2009; Toloba et al. 2011), and such galaxies share a Tully-Fisher plane with the dwarf irregulars. Rotationally supported ETDs are also observed to have younger stellar populations and are most likely to be found in the cluster outskirts (Toloba et al. 2009).

The Virgo cluster is a rich (>1000 members), relatively nearby (d ∼17 Mpc) cluster. There is no clear single core, but rather two: a compact subcluster around M49, and a more massive and extended subcluster around M87. There are also several near-background 'clouds' which are falling onto the cluster. Both its three dimensional structure (Mei et al. 2007) and the velocity dispersion of its galaxies (Binggeli et al. 1993; Drinkwater et al.

[1]The bulk of this chapter has been previously published as Hallenbeck et al. (2012).

2001; Conselice et al. 2001) suggest that the Virgo cluster is dynamically young. Due to its proximity, Virgo has been the target of many surveys, and all of its members have been targeted observationally. The most recent comprehensive compilation of Virgo member data can be found in GOLDMine (Gavazzi et al. 2003; Gavazzi et al. 2005), a multiwavelength aggregate of many data sources. Because it is so close, Virgo is also optimal for sensitive HI observations of both the dwarf galaxies and more massive members. It is the first cluster in which HI deficiency, a measure of how much less HI a galaxy contains compared to a field sample of similar optical properties, has been measured (Davies and Lewis 1973). Targeted HI observations exist for all massive late-type galaxies (Gavazzi et al. 2005), bright dwarf irregulars (Hoffman et al. 1987), and a significant number of dwarf ellipticals (Haynes and Giovanelli 1986; Huchtmeier and Richter 1986; van Driel et al. 2000; Conselice et al. 2003). Moreover, blind HI surveys have covered large fractions of Virgo, such as the HI Jodrell Bank All Sky Survey (HIJASS; Davies et al. 2004) and the Arecibo Legacy Fast ALFA survey (ALFALFA; Giovanelli et al. 2005). Recently, the VLA Imaging of Virgo in Atomic Gas (VIVA; Chung et al. 2009) survey has produced high-resolution HI maps of late-type galaxies in Virgo; this has allowed extensive study of stripping as it takes place (Chung et al. 2007; Vollmer et al. 2008). Direct HI evidence of galaxy harassment has been found by ALFALFA, which observed a $\sim$250 kpc tail off of NGC 4254 (Haynes et al. 2007).

The focus of this chapter is the dwarf galaxy population in the Virgo cluster, and specifically how dwarf galaxies form and evolve in the cluster environment, primarily through the study of their HI content using ALFALFA. In its current $\alpha.40$ data release, ALFALFA covers the Virgo cluster at declinations between 4° and 16°. Examining the HI content of Virgo has always been a goal of ALFALFA (Giovanelli et al. 2007; Kent et al. 2008), with the first global study performed by Gavazzi et al. (2008), who investigated the scaling relations between the HI and luminous properties of ALFALFA-detected galaxies in the cluster. More

recently, colors and star-formation properties using $\alpha.40$ and Hα observations were described by Gavazzi et al. (2012) and Gavazzi et al. (2013).

If dwarf ellipticals are the products of evolved dwarf irregulars and low luminosity spirals, then the efficient stripping of HI precedes quenched star formation and morphological transformation. In fact, dwarf irregulars in Virgo have detectable reservoirs of HI, and the bulk of dwarf ellipticals are relatively gas-free, having low gas fraction (M_{HI}/M_*). Nonetheless, a small fraction of ALFALFA detections are elliptical galaxies. Early-type HI-detected galaxies included in previous ALFALFA data releases have been studied both in Virgo (di Serego Alighieri et al. 2007) and in the field (Grossi et al. 2009). They found that very few Virgo early-type galaxies (ETGs; the ellipticals and S0 galaxies) had HI, and those that did were either massive galaxies which may be accreting from a companion, or dwarfs with peculiar morphologies. In the field, they found that a surprising 44% of massive ETGs were detected, possibly the results of major mergers, but only 13% of dwarf ellipticals were detected—both much higher than the 2% detection rate in Virgo.

With the near complete coverage of Virgo made available by $\alpha.40$, I compile a sample of 12 low-luminosity ($M_B > -16$) ETDs which are detected in HI by ALFALFA; this sample represents an almost two-fold increase from samples based on earlier ALFALFA catalogs. I also probe beneath the detection limit of ALFALFA using spectral stacking methods. In addition to their HI properties, I investigate their stellar populations and star formation activity using optical and ultraviolet photometry from the seventh data release of the Sloan Digital Sky Survey (SDSS DR7; Abazajian et al. 2009) and the GALEX satellite. An overview of the ALFALFA dwarf population, selected by HI mass, is presented in Huang et al. (2012b). An important result is that the within the ALFALFA dwarf sample, Virgo cluster members have lower gas fractions at a given M_{HI} with a wide spread in the distributions of specific star formation rate (SFR/M_*).

Lastly, I consider possible evolutionary paths that would lead to the existence of HI-bearing dwarf galaxies with early-type morphologies in a cluster environment. The scenarios considered include the possibility of intrinsically gas-rich objects that have recently infallen onto the Virgo cluster, stripped objects with newly recycled HI from stars near the end of their lifetimes, galaxies which have intrinsically stochastic star formation with long duty cycles, and recent accretion of gas by formerly gas-free galaxies.

This chapter is organized as follows: In section 2.2 I present the dwarf galaxy sample, and describe the selection process, as well as the HI, optical and UV data extraction process. Section 2.3 describes the HI content, colors and star formation of the sample and the reference samples, and I discuss differences among dwarf galaxies with different morphologies. In section 2.4 I present possible evolutionary paths for our sample of HI-detected ETDs, and argue about their consistency with our data.

2.2 Data and Sample Selection

Our main sample is drawn from the Virgo Cluster Catalog (VCC) (Binggeli et al. 1985), with updated morphologies and assignments found in Binggeli et al. (1993). I consider only VCC galaxies which are spectroscopically confirmed members of Virgo (with the cut $v \lesssim 3000$ km s^{-1}) and whose blue absolute magnitude in the VCC is fainter than $M_B = -16$ (corresponding to $m_B \gtrsim 15$ at the distance of Virgo). Furthermore, I exclude galaxies that belong to one of the near-background complexes which appear to be infalling on Virgo, such as the W and W$'$ clouds (de Vaucouleurs 1961), M cloud (Ftaclas et al. 1984) and the southern extension (Tully 1982). This results in a main sample composed of 365 dwarf galaxies which are Virgo members.

2.2.1 Optical Classification

Galaxies are then subdivided into classes according to their VCC morphology, which is based on high quality B-band photographic material. Unless specified otherwise, I use the term 'early-type dwarf' (ETD) to refer to galaxies classified as dwarf ellipticals (dE) and dwarf lenticulars (dS0), and the term 'late-type dwarf' (LTD) to refer to galaxies classified as Magellanic irregulars (Im) and blue compact dwarfs (BCD) by the VCC. There also exist other dwarf galaxies, generally classified as faint spirals, peculiar galaxies, or simply '?' by the VCC. In general, these 'other' dwarfs share many qualities of late-type dwarfs: blue colors and disk structure or disturbed morphology, and so as a whole I group them with the late-type dwarfs.

Overall, 275 out of the 365 galaxies in our main sample belong to the ETD class and 90 to the LTD class. I note that while VCC 2062 was classified as a dwarf elliptical by Binggeli et al. (1985), work by Duc et al. (2007) suggests that it is a tidal dwarf. As a result, I categorize it as one of the 'other' LTD dwarfs.

2.2.2 HI Characteristics

The blind HI survey provides a statistically complete census of the atomic hydrogen content of galaxies in our main sample. The $\alpha.40$ catalog covers the Virgo cluster at declinations $4^\circ < \delta < 16^\circ$ with a sensitivity of $M_{HI} \approx 10^{7.4}$ $M_\odot$ for a typical dwarf galaxy at the Virgo distance (Haynes et al. 2011, Section 6). This data release supercedes and expands the earlier ALFALFA releases (Giovanelli et al. 2007; Saintonge et al. 2008; Kent et al. 2008), which included Virgo coverage only between $8^\circ < \delta < 16^\circ$. Table 2.1 lists the number of galaxies detected by ALFALFA. In total, 80 galaxies in the main sample are included in

Selection	Total	ETDs	LTDs	Other
BST Dwarfs	502	413	89	–
$M_B < -16$	365	275	65	25
ALFALFA	80	12	51	17
SDSS	271	211	43	17
GALEX-NUV	252	197	50	5
GALEX-FUV	140	89	46	5

Table 2.1: Total number of galaxies and number of galaxies by morphology in samples discussed in §2.2. BST Dwarfs are the galaxies identified as dwarfs in (Binggeli et al. 1985) which have redshifts, while $M_B < -16$ consists of all VCC galaxies with redshifts and faint M_B. The 'other' sample here remains separate from the LTDs because they are identified via the M_B threshold and not directly by morphology, and so they have no direct BST counterparts. The ALFALFA, SDSS, and GALEX samples are each direct subsets of the blue magnitude based sample.

α.40: 68 LTDs (85% of the class) and only 12 ETDs (5% of the class). There are now four total classes of galaxies, based on a combination of optical morphology and ALFALFA HI detection status: gas-bearing ETDs, gas-poor ETDs, gas-bearing LTDs, and gas-rich LTDs.

I further divide these HI-detected ETDs into two subclasses, one blue and one red, based upon their SDSS $g - r$ color (see §2.2.3 for details on colors). This unusual subsample of 12 HI-detected dwarf galaxies with early-type morphologies is the main focus of the present paper. Their HI, optical, UV, and fitted quantities (see §2.2.3-§2.2.4) are presented in Table 2.2.

Subclass	VCC	AGC	Morph.	m_B	log M_{HI} $M_\odot$	log M_* $M_\odot$	SN	W_{50} km s^{-1}	$V_\odot$ km s^{-1}	log SFR $M_\odot$ yr^{-1}	M_r	g-r	NUV-r	FUV-r	t_{infall} Myr	t_{evap} Myr
	(1)	(2)	(3)	(4)	(5)	(6)	(7)	(8)	(9)	(10)	(11)	(12)	(13)	(14)	(15)	(16)
Blue	93	223286	dE2	16.3	7.56	7.41	6.0	50	841	-1.92	-14.8	0.35	2.44	2.96	64 – 334	180 – 560
	281	220321	dS0	15.3	7.50	8.04	5.4	32	248	-2.15	-15.8	0.52	3.22	3.85	42 – 220	156 – 488
	304	223407	dE1pec?	16.3	7.53	7.56	6.2	35	132	-2.28	-15.0	0.40	2.76	3.16	61 – 318	167 – 523
	1142	222021	dE1	19.0	7.67	6.18	13.7	27	1306	-3.33	-11.2	0.26	0.36	0.49	70 – 360	
	1202	223724	dE?	20.0	8.20	6.75	8.0	286	1215	-2.63	-13.4	0.24	2.04	2.20	38 – 195	
	1391	223819	dE1	18.5	7.39	6.34	5.4	42	2308	-2.94	-12.3	0.20	1.95	3.00	94 – 488	121 – 379
Red	190	223355	dE4	18.0	7.57	7.75	10.2	32	2352	-4.59	-14.6	0.45	3.98	6.72	54 – 283	183 – 573
	421	223445	dE2	17.0	7.55	7.48	5.1	111	2098	<-3.45	-14.2	0.51	4.52	—	62 – 325	110 – 344
	956	222857	dE1,N:	18.8	8.00	7.34	10.3	102	2151	-2.85	-13.1	0.53	3.84	5.82	42 – 220	
	1533	223873	dE2,N	18.0	7.44	*	10.5	21	648	*	-13.9	0.59	2.89	3.98	< 91 – 474	136 – 425
	1649	223913	dE3,N:	15.7	7.11	8.21	3.3	28	972	<-3.70	-16.0	0.60	4.40	>6.95	41 – 212	64 – 198
	1993	220977	E0	15.3	7.67	8.65	5.8	119	925	<-2.45	-16.6	0.63	5.90	>8.76	24 – 126	231 – 722

Table 2.2: Properties of the dwarf ellipticals detected in HI by ALFALFA, split based on g-r color from the SDSS. Subclass: The blue subclass is defined by lower g-r color as a function of absolute r-band magnitude; Column 1: VCC identifier (from Binggeli et al. 1985); Column 2: Arecibo General Catalog number (Haynes et al. 2011); Column 3: Galaxy morphology (Binggeli et al. 1985; Binggeli et al. 1993); Column 4: VCC apparent B-band magnitude (Binggeli et al. 1985); Column 5: HI mass, from α.40; Column 6: stellar mass as detailed in §2.2.4; Columns 7 through 9: HI detection signal to noise, HI line width at 50% level, and heliocentric velocity, from α.40; Column 10: star formation rate, as discussed in §2.2.4; Columns 11 through 14: absolute r-band magnitude, SDSS and GALEX colors, for galaxies where data exists. Colors are corrected for galactic extinction only, using the SDSS pipeline correction; Column 15: Range of Estimated gas infall times based on Equation 2.1, assuming infall from the optical radius (lower bound) or half the size of Arecibo beam (upper bound); Column 16: Estimated gas evaporation time based on Equation 2.2, assuming accreted gas cloud was half the size of the Arecibo beam (lower bound) or the optical radius (upper bound). The fits for VCC 1533 fail because the z-band photometry is bad: it is fainter in z-band than in other bands, while all of our models have z band as the brightest band.

Follow-Up Observations

Because the subsample of interest is comprosed of such a limited number of objects, it is important to consider the reliability of these ETD HI detections individually. The HI spectra of all 12 galaxies can be seen in Figure 2.1, where the top 6 spectra are the blue subclass, the bottom 6 the red subclass). The horizontal dashed line indicates the zero flux density level after baseline subtraction, and the vertical dotted line indicates the HI line center (see also Table 2.2 for their HI properties). All galaxies are well-separated from nearby, more massive HI emission, and their detections cannot be attributed to sidelobe contamination.

All but one of the $\alpha.40$ HI detections with S/N$<$ 10 (Table 2.2) have been re-observed using more sensitive pointed observations, centered on the optical positions using Arecibo's L-band wide (LBW) single pixel receiver. Of those, only VCC 421 was not confirmed. However, the HI emission of VCC 421 has a large ($1.1'$) angular offset from the optical galaxy, and our failure to confirm it may merely be due to the LBW observing strategy of pointing at the optical galaxy, rather than centroided HI emission. Likewise, the emission of VCC 1649 has been confirmed to be offset (by $1.4'$) from the optical galaxy, and so the association of the HI emission with this galaxy is uncertain. The ALFALFA spectrum of VCC 1202 is poor and very wide (W50= 286 km s^{-1}) because it is both near M87 and has only half the typical integration time for ALFALFA. The follow-up observations have better baselines. Of the 5 galaxies not yet re-observed, all are classified as 'Code 1' sources in $\alpha.40$, that is they are confidently detected sources ($S/N_{\rm HI} > 6.5$) with well-defined spectral profiles, and so are not of concern.

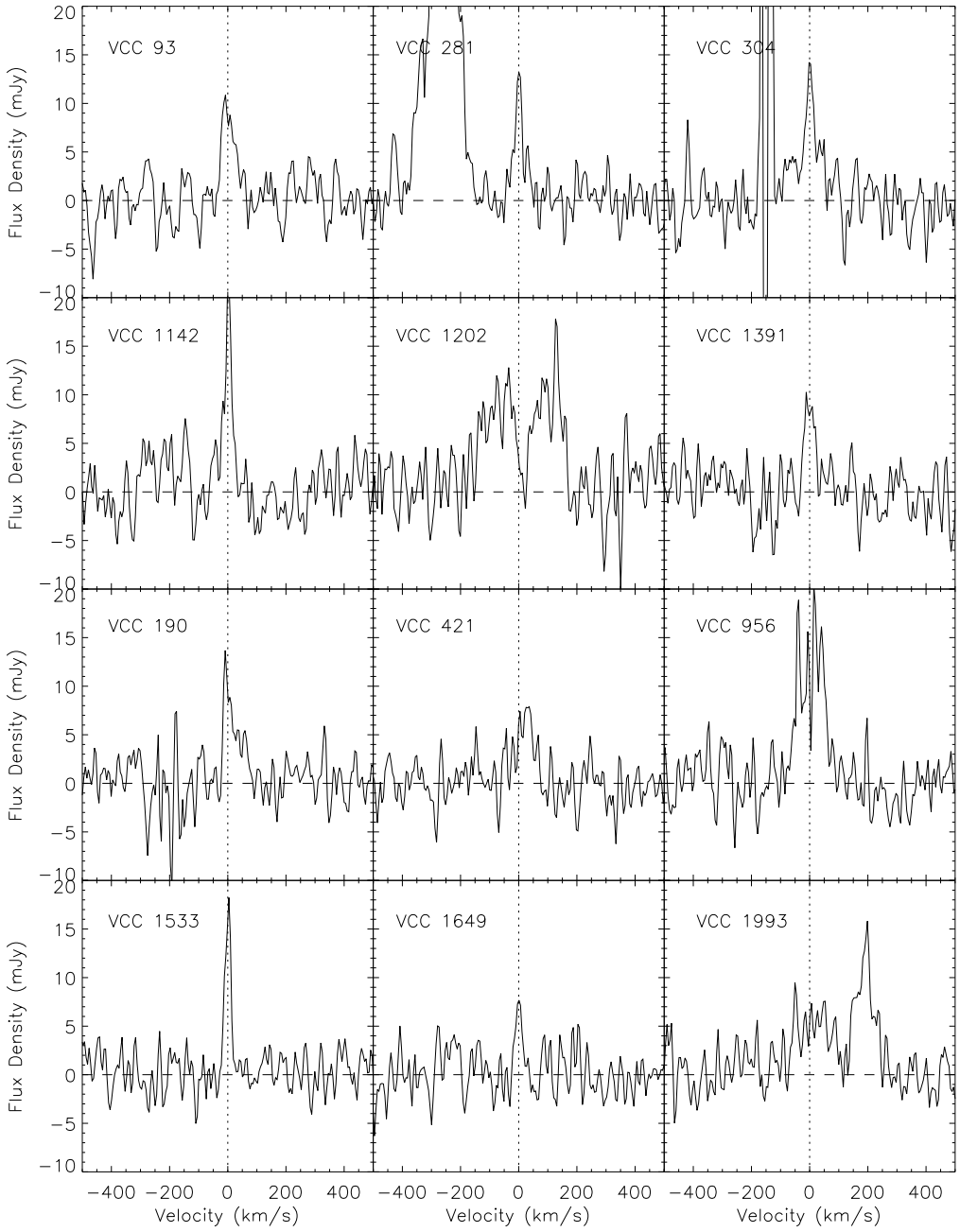

Figure 2.1: The spectra of the 12 HI-detected ETDs, split into a blue subclass (top 6) and red subclass (bottom 6) based on SDSS the $g - r$ colors. Horizontal dashed lines indicate the 0 mJy flux density level after baseline subtraction; vertical dotted lines indicate the line center velocity as reported in $\alpha.40$.

Comparison With Other HI Samples

Only about half of the 12 HI-detected ETDs have previously reported HI observations in the literature. In particular, seven (VCC 93, 304, 1142, 1202, 421, 956, 1993) are included in the sample of HI-detected early-type Virgo galaxies of di Serego Alighieri et al. (2007), which was based on earlier ALFALFA data releases. The HI sample of Gavazzi et al. (2008), also based on earlier ALFALFA releases, includes two ETD detections (VCC 93, 304). Targeted HI observations (Huchtmeier and Richter 1986; Burstein et al. 1987; Duprie and Schneider 1996) have reported 4 more gas-bearing dEs in Virgo; however none of them is included in our sample since they are all brighter than the $M_B > -16$ threshold. On the other hand, neither of the dwarf ellipticals (VCC 390 and 713) detected by the deep 21cm observations of Conselice et al. (2003) using Arecibo were detected by ALFALFA, despite having reported HI masses well above the ALFALFA completeness limit. The Arecibo Galaxy Environment Survey (AGES; Auld et al. 2006) observations of the Virgo cluster (Taylor et al. 2012) detected 7 ETDs over 20 $\deg^2$ of which three appear in our sample (VCC 190, 611, and 1142); the other four do not pass our selection criteria. Of the three, only VCC 611 was not directly detected by ALFALFA (but see §2.3.1). Lastly, 6 of the 12 HI-detected ETD galaxies (VCC 93, 281, 304, 1142, 1533, 1649) are included in the complete sample of low HI mass ($\log M_{HI}/M_\odot < 7.7$) ALFALFA dwarfs of Huang et al. (2012b).

2.2.3 Optical and Ultraviolet Photometry

In order to derive global stellar properties for the 12 HI-detected ETDs (stellar masses and star formation rates), I use optical images from the 7th data release of the Sloan Digital Sky Survey (SDSS DR7; Abazajian et al. 2009) and ultraviolet (UV) data from the GALEX

mission. Figure 2.2 contains inverted SDSS images for all 12 galaxies; the images are $1'.5$ on a side (7.3 kpc at $d = 16.7$ Mpc) and combine the i, r, and g SDSS bands into the RGB color channels. Five galaxies (VCC 190, 956, 1142, 1391, 1533) are evidently very low surface brightness objects and their SDSS pipeline photometry was deemed 'problematic.' To remedy this, the SDSS images of all 12 HI-detected ellipticals were manually reduced and their photometry was obtained individually with the use of IRAF/STSDAS tasks. Briefly, the corrected frames (`drC` files) in the u, g, r, i, z bands were first smoothed to $2.5''$ resolution, and then background subtracted. After masking contaminating background and foreground sources, we fit elliptical isophotes to the r-band image of each galaxy. The derived apertures were applied to all other bands, and Petrosian magnitudes based on these elliptical apertures was calculated, separately for each band.[2]

Ultraviolet photometry for the 12 HI-detected ETDs was obtained from the publicly available GALEX General Release 6 (GR6) database. Eight galaxies have deep ($t_{exp} \gtrsim 1000$ s) GALEX coverage, while the remaining four galaxies (VCC 281, 1391, 421, 1993) have only shallower coverage through the GALEX All-Sky Imaging Survey (AIS; $t_{exp} \approx 100$ s) images. Three galaxies (VCC 421, 1649, 1993) are not detected in the FUV band; in these cases the FUV flux measured at the position of the NUV detection by the GALEX pipeline (`fuv_ncat_flux`) was adopted as an upper limit on the galactic FUV flux. All magnitudes in Table 2.2 are corrected only for galactic extinction, based on the dust maps of Schlegel et al. (1998). We do calculate internal extinction (see §2.2.4), but these corrections have high fractional uncertainty and are generally small (0.2-0.4 magnitudes) for these galaxies. In order to compare with similar works (Lisker et al. 2007; Kim et al. 2010), we do not

[2]The process described here is very similar, but not identical, to the SDSS pipeline measurement of Petrosian magnitudes (as described in `http://www.sdss.org/DR7/algorithms/photometry.html`). The main difference consists in the fact that the SDSS pipeline extracts measurements in circular rather than elliptical apertures. However, since the galaxies under consideration have generally low ellipticity, the difference in methodology is inconsequential for this study.

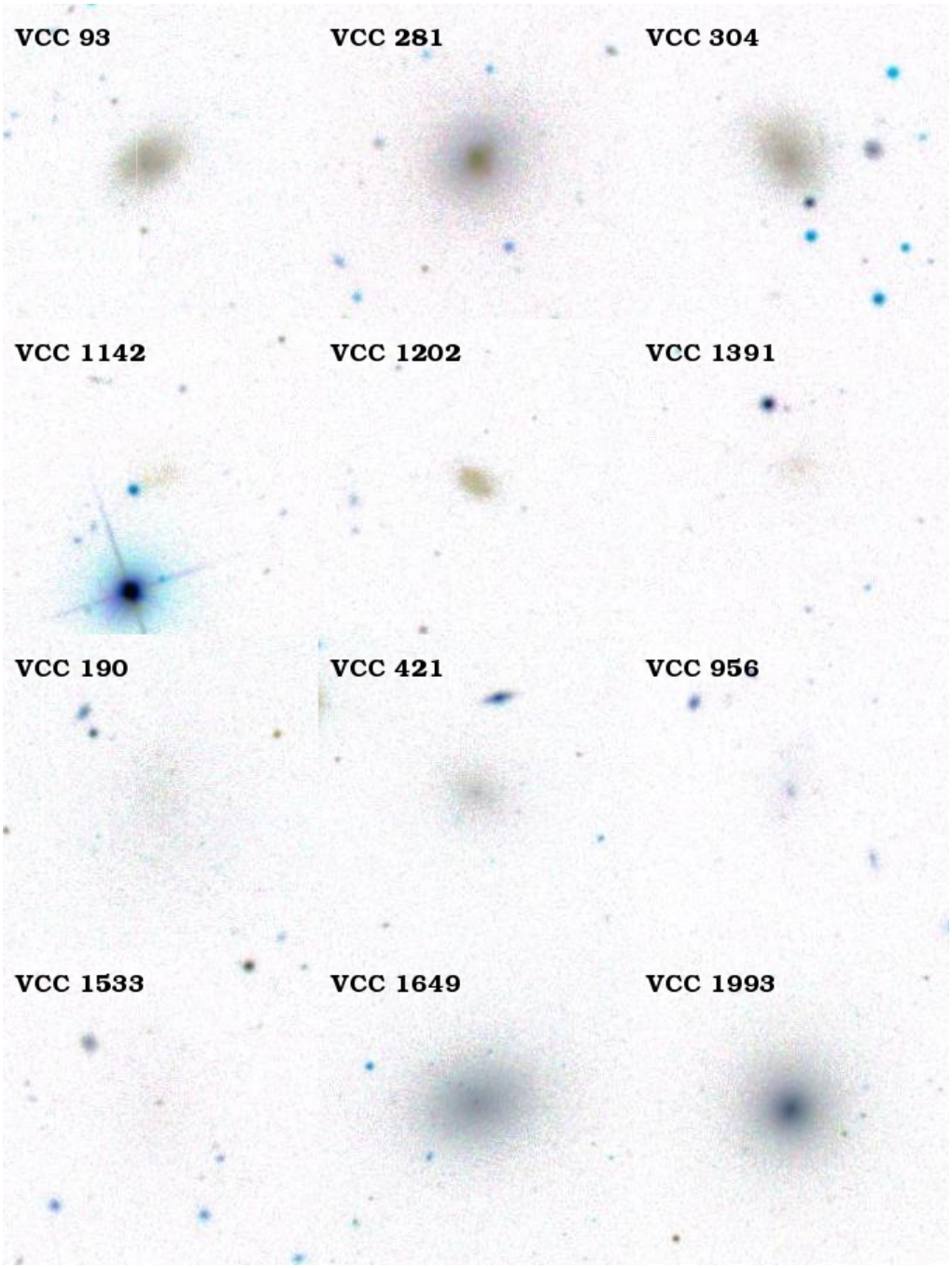

Figure 2.2: Inverted SDSS images of all 12 VCC dwarf ellipticals detected by ALFALFA, 1.5′ (7.2 kpc at D=16.7 Mpc) on a side. The images combine the g,r, and i SDSS bands (in the blue, green, and red color channels, respectively). The top 6 belong to the blue ETD class (see §2.3.2), the bottom 6 the red ETD sample. The surface brightness of VCC galaxies 190, 956, 1142, 1391 and 1533 are so low that the SDSS pipeline failed to yield suitable photometry.

include these extinction corrections in our reported magnitudes and colors.

2.2.4 Derived Quantities

Atomic hydrogen (HI) masses are taken directly from α.40. Distances to Virgo galaxies are based upon individualized subcluster assignments. I adopt a distance modulus of 31.11 for galaxies belonging to the A subcluster (M87 group), 31.08 for those belonging to the B subcluster (M49 group), and a weighted average of 31.09 for galaxies with uncertain subcluster assignment, according to the surface brightness fluctuation work of (Mei et al. 2007). I use primary distance measurements from the literature where available.

We estimate stellar masses and star formation rates (SFRs) for our galaxies using all available optical and UV bands following the method of Salim et al. (2007), as described in Huang et al. (2012b) and Huang et al. (2012a). The computation involves fitting a library of model spectral energy distributions (SEDs) to the 5 SDSS and (when available) the 2 GALEX magnitudes. Full details of the method, as well as comparisons with other common estimators (e.g. Bell et al. 2003), can be found in Huang et al. (2012b). Here I summarize the main points: model SEDs are generated by the Bruzual and Charlot (2003) stellar population synthesis code, assuming a Chabrier (2003) stellar initial mass function. The star formation histories are a combination of continuous star formation and random bursts of star formation. We consider a large library of models with a broad range of internal extinctions ($0 \leq \tau_V < 6$), μ factors (the fraction of optical depth that affects stellar populations older than 10 Myr; $0.1 < \mu < 1$), and metallicities ($0.1Z_\odot \leq Z \leq 2Z_\odot$). These parameter spaces are consistent with those of Salim et al. (2007). The final physical properties are computed as the weighted average of all models, according to their fit likelihood. We stress that these extinction and metallicity values are not intended to encompass all possible values for a

particular dwarf galaxy, but are expected to represent typical values for an ensemble of galaxies. Additionally, our stellar mass estimates are robust with respect to the exact value of the extinction parameter.

In cases where the FUV magnitude is not available, model SEDs are fit only to the 5 SDSS bands. I have verified that the derived stellar masses are not significantly affected by the exclusion of the UV photometry from the fitting process. On the other hand, SFRs derived from fitting just the optical bands tend to significantly overestimate the SFRs derived from fitting the full optical+UV SED (by up to $\approx$ 2 dex, especially for galaxies with very low SFR). As a result, for galaxies not detected in the FUV I treat the SFR derived just from the optical data as an upper limit.

2.2.5 Reference Sample

In order to place the sample of 12 HI-detected ETDs in context, I analyze HI, optical and UV data for the rest of our main sample as well. This includes 68 HI-detected galaxies of late-type or 'other' morphology and 285 HI non-detections, mostly of early-type morphology. I determine the average gas mass of ETD non-detections by spectral stacking of the full ALFALFA datacubes. I follow the method of Fabello et al. (2011) and stack HI spectra using optical positions from the VCC and optical redshifts from the literature. In total 238 non-detected ETDs had acceptable spectra for stacking; galaxies whose emission would fall within the Galactic HI emission and galaxies that could be confused with more massive nearby sources were discarded. Figure 2.3 shows the spectrum produced by stacking all usable ETD spectra. The noise level in the stacked spectrum has clearly decreased with respect to the case of a single spectrum, but no HI emission is detected down to $M_{HI}/M_{\odot} = 10^{5.5}$. The greater area coverage of $\alpha.40$ allows for a significant improvement over the stacked mass

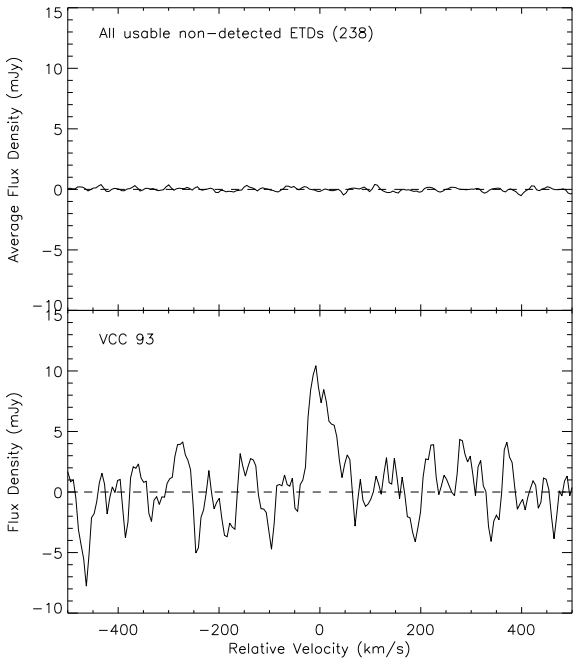

Figure 2.3: (top) Spectrum obtained by co-adding all useable 238 HI non-detected ETD spectra. While the final noise level is greatly reduced, from ∼2.2 mJy rms to 0.17 mJy, no HI emission signal is recovered. (bottom) Spectrum of VCC 93, for which the signal to noise of the spectrum extracted from the ALFALFA database is 6. The x-axis values are velocities relative to the line center; as the stacked spectrum is produced by redshifting all component galaxies to 0 km s^{-1}, there is no true redshift for this subset.

sensitivity of $M_{HI}/M_{\odot} = 10^{6.1}$ achieved by the Virgo coverage of AGES (Taylor et al. 2012).

I obtain optical and UV photometry for galaxies in the main sample through the SDSS DR7 and GALEX GR6 databases. The quality of the SDSS pipeline photometry of every galaxy was individually evaluated; galaxies that were 'shredded' by the pipeline (i.e. assigned multiple photometric objects of comparable brightness) and low surface brightness objects with missing flux issues were flagged as 'problematic' and excluded from further analysis. This quality cut affects mostly galaxies with $M_B \gtrsim -13.5$, of which about half have problematic photometry. A similar individual inspection of the quality of the GALEX pipeline photometry was performed for all galaxies in our main sample. Due to the lower resolution of the GALEX images ($\approx 5''$ seeing), problems related to shredding and missing

flux of low surface brightness galaxies are far less common compared to SDSS. Overall, 314 galaxies have available NUV magnitudes, of which 240 were derived from deep GALEX images ($t_{\rm exp} \gtrsim 1000$ s) and 74 from shallower AIS images ($t_{\rm exp} \approx 100$ s). About 43% of these galaxies were too faint to be detected in the FUV band; not surprisingly, all except 4 of the FUV non-detections correspond to early-type objects. All derived quantities for our main sample (HI mass, stellar mass, SFR etc.) are computed as described in §2.2.4. I note again that for galaxies that are not detected in the FUV, SFRs are based on fitting just the 5 SDSS bands and are used only as upper limits.

I also use the sample of low HI-mass ALFALFA dwarfs of Huang et al. (2012b) as a comparison sample, representing the properties of gas-bearing field dwarfs. The HI masses, SDSS photometry and physical properties of the galaxies in the Huang et al. sample are calculated as in this work (§2.2.3-§2.2.4). However, UV magnitudes in Huang et al. (2012b) are manually measured with the use of the GALPHOT image reduction package (Haynes et al. 1999), written in the IRAF/STSDAS environment. The difference between manually measured and pipeline magnitudes is small in the NUV band (≈ 0.20 mag), while manually measured magnitudes tend to be brighter than pipeline values in the FUV band because the pipeline often misses low surface brightness flux (see Fig. 8 in Huang et al. 2012b).

2.3 Results

2.3.1 Gas Content

It is well known that the Virgo cluster environment efficiently removes gas and advanced galaxy evolution. Even massive spirals are observed to be HI poor (Davies and Lewis 1973;

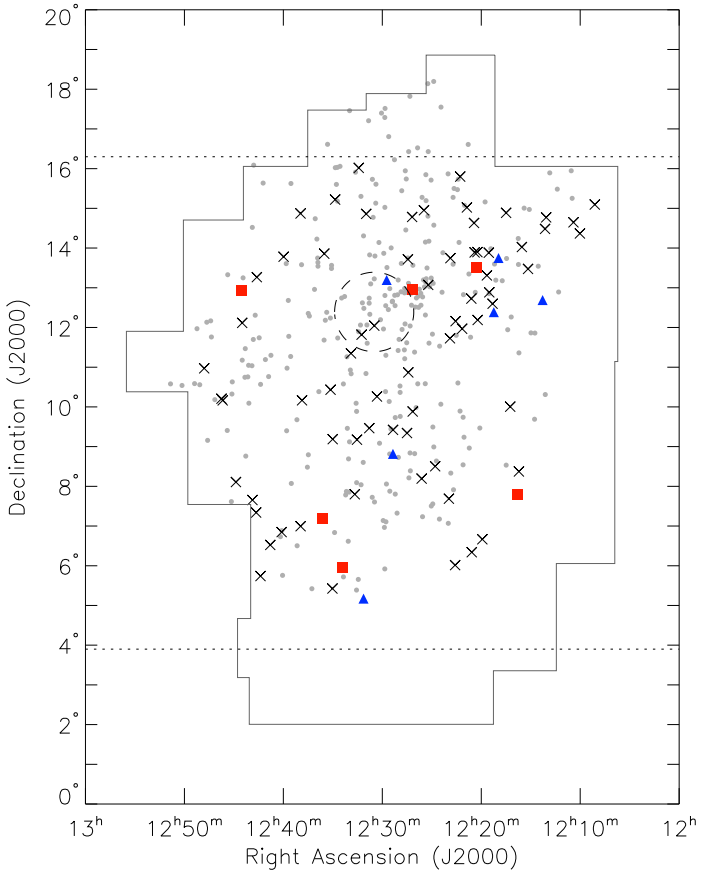

Figure 2.4: Locations of the α.40-detected dwarfs assigned membership in the Virgo cluster: xs are late-type dwarfs, blue filled triangles are the blue subclass of ETDs and red filled squares are the red subclass of ETDs. HI non-detections with known redshifts are gray small filled circles. The dashed circle indicates a 1° ring around the location of M87. Within this radius, the Strong (213 Jy; Condon et al. 1998) continuum emission of M87 causes an increase in system temperature and standing waves, therefore reducing the detectability of HI line sources (Giovanelli et al. 2007; Kent et al. 2008). The horizontal dotted line indicates the Northern and Southern-most range of coverage of the α.40 survey (Haynes et al. 2011).

Haynes and Giovanelli 1986), with small HI disks stripped inside the optical disk observed near the core, while relatively unperturbed disks are seen in the outskirts (Cayatte et al. 1990; Chung et al. 2009). Because of the removal of HI, the distribution of HI detections of dwarf galaxies in a survey like ALFALFA in Virgo is far from uniform. Figure 2.4 shows the sky distribution of the galaxies in our dwarf sample. Xs indicate the location of HI detected late-type dwarfs, and small gray filled circles the non-detected dwarfs. The HI detected early-type dwarfs are plotted with different symbols based on subclass: the red ETDs are red filled squares, while the blue ETDs are blue filled triangles. Near M87, its strong continuum emission increases the system noise and sets up standing waves in the telescope optics and makes detection difficult; a 1° circle is drawn to indicate the region of contamination. Dashed lines indicate the northern and southern-most extent of the $\alpha.40$ survey. The outline corresponds to the plates of the original Virgo Cluster Survey (Binggeli et al. 1985). With the exception of two objects close to M87, the HI detected ETDs are found near the edges of the cluster along with the HI detected LTDs.

Figure 2.5 shows the gas fraction as a function of SED-derived stellar mass for the HI-detected dwarfs. The late-type dwarfs define a clear trend from high gas fraction at low stellar mass to low gas fraction at high stellar mass; a dashed line shows a linear fit to the LTDs with a dotted line showing a 2σ variation around the line. This distribution exhibits the same behavior observed by Gavazzi et al. (2012) and Gavazzi et al. (2013) for all Virgo galaxies; The HI-bearing dwarf galaxies in this sample are simply the low stellar mass end of all HI-bearing Virgo galaxies. Also plotted are the $\alpha.40$ dwarfs (small open purple circles; see §2.2.5), which fit into the same ranges as the LTDs, but with slightly more total scatter. The HI-stellar mass properties of the gas-bearing dwarfs in Virgo are thus similar to the field dwarf galaxies. At this level of inspection, there does not appear to be any significant difference between the two subclasses of HI-detected ETDs: both are well within the distribution of

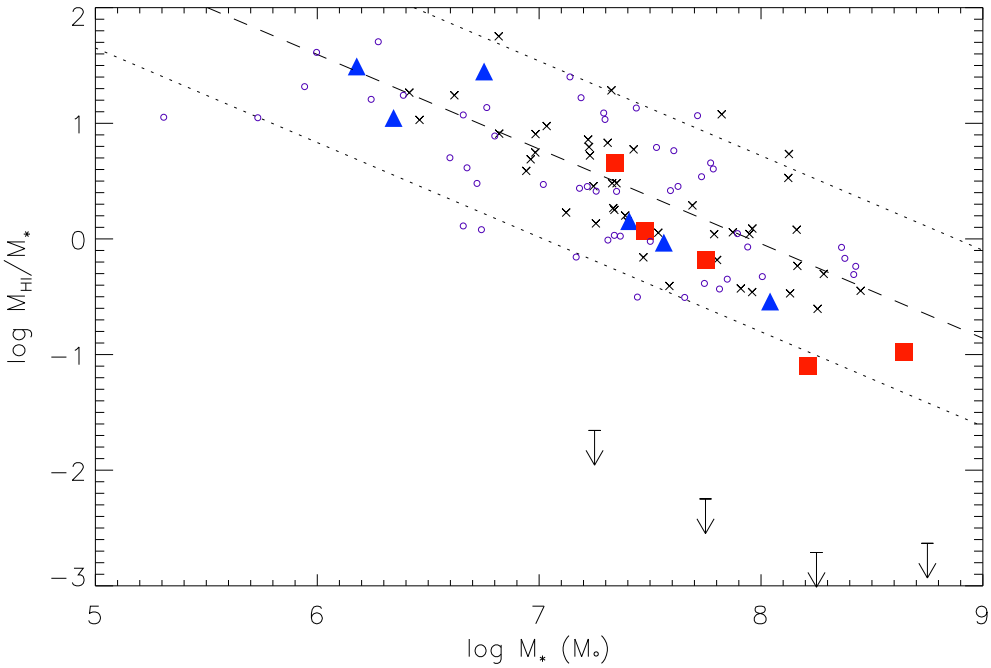

Figure 2.5: Relationship between stellar mass and log gas fraction for the HI-detected sample. Symbols are the same as for Figure 2.4. The lines show the linear trend and 2-σ variation for the late-type galaxies only. The arrows show 3σ upper limits on the non-detections determined via stacking (see §2.2.2; Fabello et al. 2011). The small open purple circles are the ALFALFA dwarfs not in the Virgo cluster (Huang et al. 2012b). As is typical for any population, the average gas fraction decreases with increasing stellar mass. It is unusual, however, that both the red and blue ellipticals appear HI-normal for late-type cluster galaxies of equivalent stellar mass.

the late-type dwarfs at their respective stellar masses. The arrows in Figure 2.5 show the 5σ upper limit of the non-detections as determined by spectral stacking. Even at this upper limit, the average non-detection is at least 2.5 dex poorer in HI gas fraction compared to the typical HI detected dwarf.

I visually inspected all 238 HI non-detected ETD spectra extracted for stacking (see §2.2.5) to look for any sign of gas just below ALFALFA's detection limit. Of these, 9 galaxies had spectra with suggestive HI candidate signals of too low S/N to have been included in the α.40 catalog. More sensitive pointed HI observations have been conducted of 8 of these

9 and confirmed the reality of one: VCC 611. The absence of a significant population just below the ALFALFA detection limit indicates that the HI detected ETDs are unlikely to be the tail of a wide distribution of HI masses, but are a separate population from the average very gas-poor ETDs.

2.3.2 Colors and Star formation

Lisker et al. (2007) have shown that the optical colors of Virgo dwarf ellipticals follow a relationship similar to that of the more massive ellipticals: the fainter galaxies are in the r-band, the bluer their colors tend to be. The same trend towards redder colors at brighter magnitudes was observed by Kim et al. (2010) in the NUV$-r$ and FUV$-r$ colors. In the FUV, these trends break down for the more massive ellipticals; this reddening is halted in ellipticals by the ultraviolet upturn (Boselli et al. 2005; Boselli et al. 2008a; Boselli et al. 2008b). Kim et al. (2010) also found that both the late and early-types outside the cluster core are well separated in NUV$-r$ colors from the inner ellipticals; this separation is even greater in the FUV$-r$. They argued that the bluer UV colors of galaxies in the cluster outskirts could be ascribed to higher star formation rates and higher gas fraction. Figure 2.6 shows the $g-r$, NUV$-r$, and FUV$-r$ colors plotted as a function of absolute r band magnitude, with the same ranges plotted as Kim et al. (2010) Figure 1. The 12 gas-bearing ETDs as a class do not fit cleanly into either the red sequence or blue cloud: half lie within the red sequence, while the other half lie in the blue cloud. For convenience, I have split the HI detected ETDs into two subclasses, galaxies that appear to belong to the blue cloud and galaxies that appear to belong to the red sequence. I find that the line of $g-r=-0.08M_r-0.73$ (plotted as a dashed line in Figure 2.6) adequately separates them, with the two faintest dwarfs in r-band (VCC 1142 and 1391) chosen to be blue. Two of the

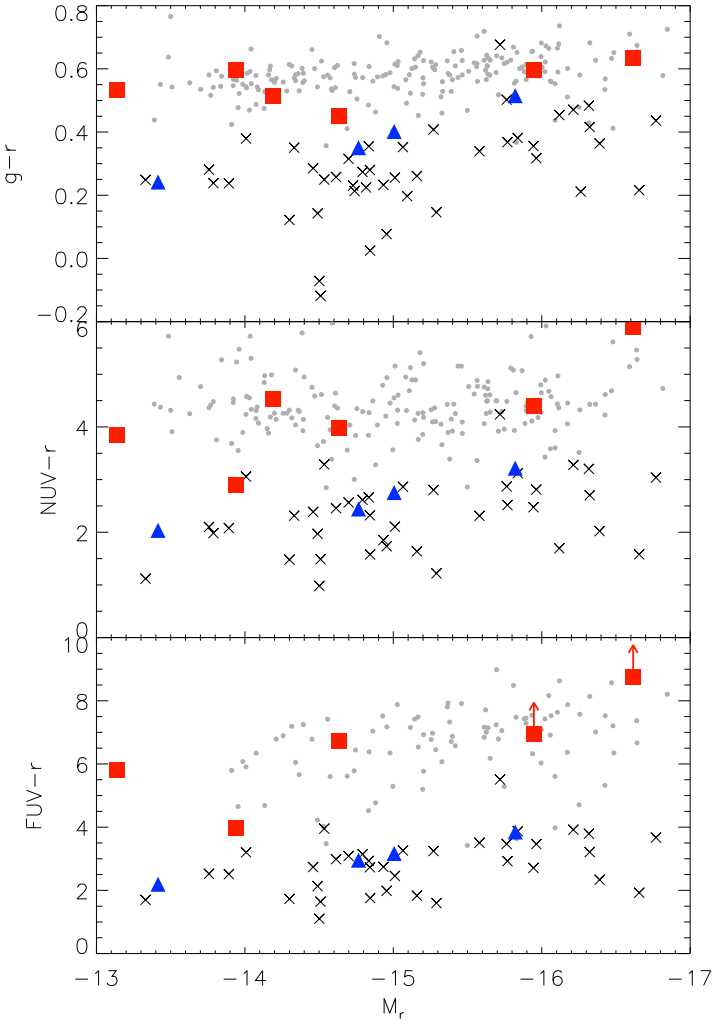

Figure 2.6: Optical (SDSS) and UV (GALEX) colors for the dwarf galaxy sample for which acceptable photometry is available. Symbols are the same as for figure 2.4. The dashed line shows our chosen split between the red and blue subclass; galaxies where $g - r < -0.08M_r - 0.73$ are considered blue. Two of the blue ETDs (VCC are so faint that they have $M_r \sim -11$; they are left unplotted as there are no other nearby galaxies for comparison. Arrows indicate galaxies for which the NUV$-r$ and FUV$-r$ colors are lower limits.

detected ETDs (VCC 190 and 281) are very close to the line, but clearly belong to the red sequence and blue cloud, respectively, when examining the NUV$-r$ and FUV$-r$ colors.

As blue color is a commonly used, albeit crude, indicator of star formation, we investigate star formation rates to begin understanding the difference in the red and blue subclass of

the ETDs. Figure 2.7 shows the trends of specific star formation rate (SFR/M_*) and star formation efficiency (SFR/M_{HI}) for all the HI-detected dwarfs as functions of stellar mass. The LTDs form a band with width of $\sim$2 dex in log yr^{-1}; the blue ETDs are also found in this region. At very low stellar masses, the SSFR and SFE have a much wider spread; this may be due to bursty, rather than continuous star formation history. The $\alpha.40$ field dwarfs (open purple squares; Huang et al. 2012b) have a similar distribution in stellar mass, SSFR, and SFE as the LTDs and blue ETDs. With one exception, the red ETDs have low SSFR and SFE compared to the LTDs and blue ETDs of similar stellar mass. VCC 956, though a red galaxy, has a SSFR comparable to the bluer galaxies. The other red ETDs lie at the bottom of the blue galaxies' distribution or a dex lower.

2.4 Evolutionary Hypotheses

We turn our attention to the possible histories of the HI-detected early-type dwarfs. Figure 2.8 is a schematic overview of the standard gas-stripping evolutionary scenario. Galaxies in the right column are HI-rich, while galaxies in the left column have sub-ALFALFA masses of HI. Galaxies in the top row have LTD optical features and generally are observed to have blue colors, while galaxies in the bottom row have ETD optical features and generally have redder colors. Overlaid on each image (taken from the SDSS) is the number of galaxies in our sample which fit into each category. Galaxies are believed to arrive in the cluster as gas-rich, star forming LTDS (top right). These new arrivals are stripped as they pass through the cluster, and for a short period are relatively gas-free, but still appear blue because their massive stars have not yet died and some residual star formation continues (top left). Eventually, star formation ceases and (bottom left). The HI-detected ETDs (bottom right) do not fit in.

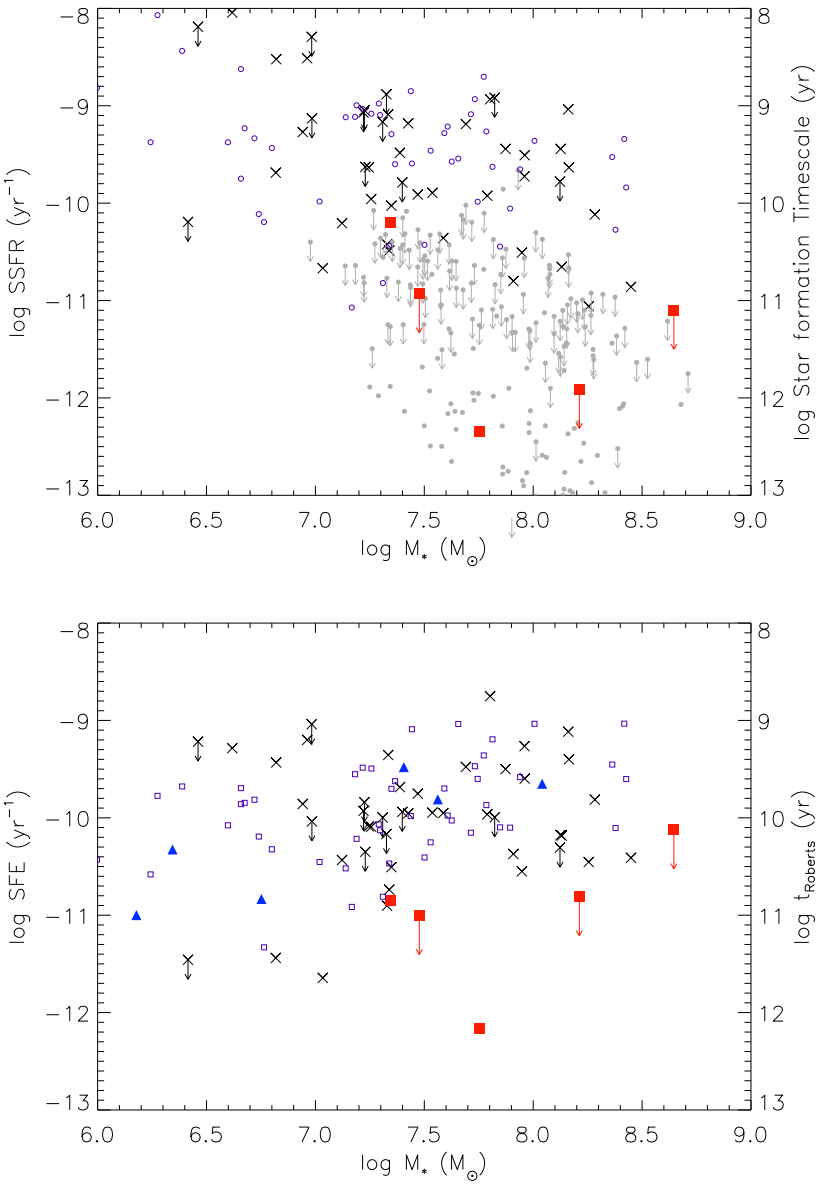

Figure 2.7: Specific star formation rates (SFR/M_*; top) and star formation efficiencies (SFR/$M_{\rm HI}$; bottom) for the HI-detected dwarf galaxies as a function of stellar mass. Symbols are identical to Figure 2.4 and arrows indicate upper limits. The small open purple squares are the α.40 dwarfs not in the Virgo cluster. While there is large spread in SFR at the lower stellar masses, at high stellar mass ($M_*/M_\odot \gtrsim 10^{7.5}$), the spread decreases and the detected late-type dwarfs have somewhat elevated SFR compared to the red class of ETDs, while the galaxies in the blue class of ETDs fit into the lower half of the LTD SFR.

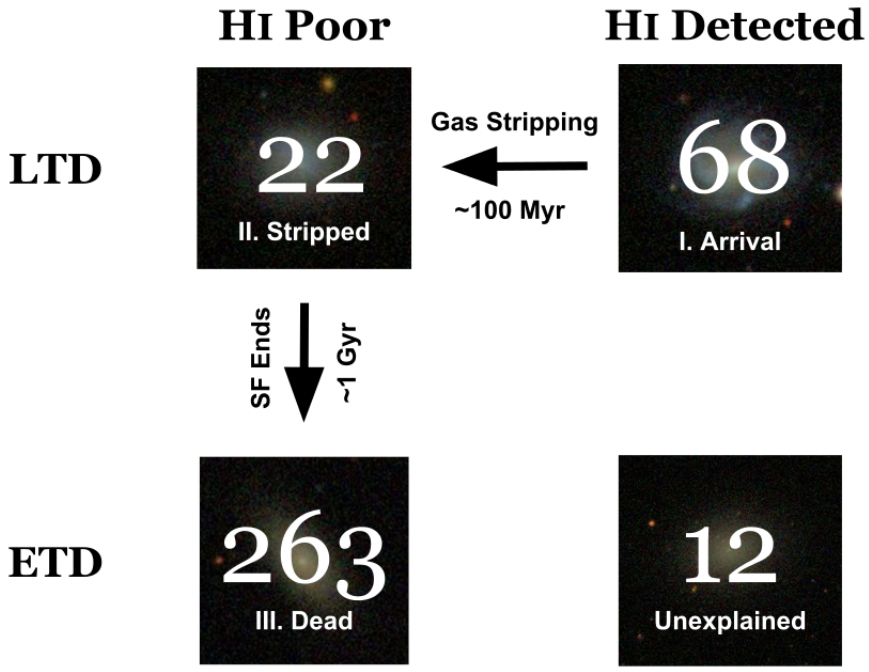

Figure 2.8: Schematic diagram of cluster dwarf galaxy evolution, in three stages. (I, top right) A gas-rich LTD arrives at the cluster. (II, top left) The gas has been stripped from the LTD, but it retains residual star formation and a few young blue stars, maintaining its optical appearance. (III, bottom left) Star formation has completely ceased in the galaxy and all young stars have died, leaving a 'red and dead' ETD. (bottom right) Gas-rich ETDs are not explained by this evolutionary framework. Numbers overlaid are the relative number in our Virgo Cluster samples, and images are optical images acquired from the SDSS browser.

What mechanisms could allow a population of gas-bearing dwarf ellipticals to exist in a cluster environment today? In the following sections, I discuss the merits of four possibilities for this particular population. The first is that they are mis-classified galaxies, which were initially gas rich dwarf spirals or irregulars which are currently being stripped of their gas. The second is that the gas is recycled, originating from massive stars returning their hydrogen to the interstellar medium. The third is that these galaxies are unstripped galaxies which have an unusually erratic or 'bursty' star formation history. The final scenario is that they are ellipticals which were previously red and 'dead,' but have recently accreted a fresh supply

of HI.

2.4.1 Galaxies Being Stripped

One evolutionary scenario is that ETDs are late-type galaxies, typically dwarf irregulars and low luminosity spirals, which have been or are being evolved by the cluster. A variety of mechanisms have been proposed for the evolution from late-type galaxy to ETD in cluster. A strong contender is ram-pressure stripping (Gunn and Gott 1972), where a galaxy moving through a cluster has the gas in its outskirts removed by the hot intra-cluster medium (ICM). The effect in the Virgo cluster is apparent enough that it has been observed directly in spirals at projected distances 0.6 Mpc $< d <$ 1 Mpc (Chung et al. 2007; Vollmer et al. 2008). The long-term consequence of ram-pressure stripping is a quenching of star formation, leading to a red, quiescent galaxy. Boselli et al. (2008a) found that if a galaxy is in a first-pass highly eccentric orbit through the Virgo cluster center, this change can occur in as little as 100 Myr, much shorter than a cluster crossing time. In contrast, significant changes in color and star formation rate take longer, on the order of a Gyr. The dwarfs with the lowest stellar masses, including our sample, are expected to be the most susceptible to the evolving effects of the cluster. The ongoing ram-pressure stripping scenario may thus explain the gas-rich, star-forming ETDs we observe. These galaxies exhibit similar star formation rates and gas masses to unstripped Virgo and field dwarfs. They may appear to be ETDs as they undergo current evolution by the cluster, or may be so faint that any LTD features are not readily apparent, and may be apparent with deeper optical observation or the application of unsharp masks following Lisker et al. (2006b). However, for the HI-detected red ETDs, this explanation does not work: these galaxies have very low star formation rates, even though their HI has not yet been removed.

In another cluster evolution mechanism, galaxy harassment (Moore et al. 1996), a galaxy is perturbed by multiple close encounters with its neighbors. Smith et al. (2010) found in simulations that, for dwarf galaxies infalling on Virgo, harassment significantly contributes to galaxy evolution in a relatively small number of cases ($< 15\%$). However, in those cases, morphological transformation was strong, producing short-lived spiral arms in initially smooth disks, and signficant concentration of gas and star formation in the central part of the galaxy. Lisker et al. (2006a) found a population of early-type dwarfs with disk-like features and star formation occuring in their central regions, and galaxy harassment may be the best explanation for these. Of our HI-detected sample, I note that VCC 281, one of the blue ETDs, exhibits this 'blue center' quality; for this one object galaxy harassment is a strong possibility. However, other possibilities exist: for example, ram-pressure stripping can also produce such a blue color gradient (Boselli et al. 2008a).

At this stage, we will focus on the six red, HI-detected ETDs, for which we can safely rule out any more mundane processes.

2.4.2 Recycled Gas

While ram-pressure stripping will efficiently remove gas from a dwarf galaxy after a single pass through the cluster, small quantities of HI can be replenished internally. As stars evolve, they return metal-enriched HI to the interstellar medium. This would mean that these ETDs have been completely evolved by the cluster, but are entering a new evolutionary stage due to internal processes, as shown in Figure 2.9.

I now consider the possibility that gas is recycled gas, following the analysis of Boselli et al. (2008a). For an efficient ram-pressure stripping model, the amount of recycling can be

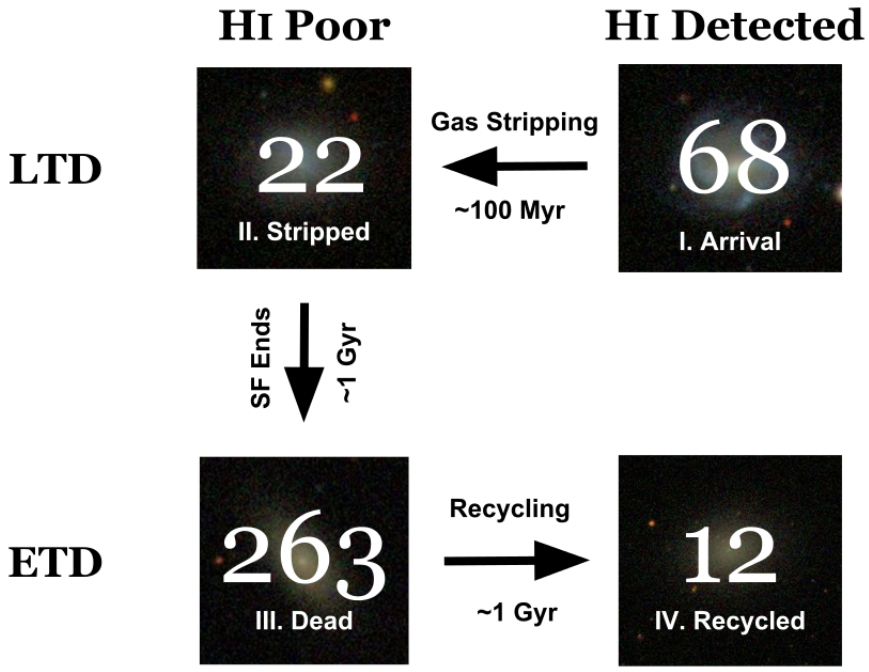

Figure 2.9: Schematic diagram of cluster dwarf galaxy evolution for the recycled gas hypothesis. Stages I-III are identical to 2.8. As the massive stars in each dwarf galaxy die, they explode and return a non-negligible amount of gas to the interstellar medium, moving the galaxies from III to IV. Given time, such galaxies may even re-ignite significant star formation.

quite significant. After a pass through the cluster core, star formation can then continue, at a star formation rate 1-2 dex below that found in a similar mass non-stripped dwarf, by feeding off of this recycled gas. This quenching of star formation will effectively move such a galaxy on the color-magnitude relation in FUV$-r$ from the blue cloud to the red sequence. We observe the red ETDs to have signficantly lowered SSFRs (by factors of 1-2 dex compared to the blue ETDs and LTDs), and they also fit solidly into the red sequence. However, the HI masses predicted by recycling are too low. For a dwarf galaxy beginning with 10^8 $M_\odot$ of HI, after significant ram pressure stripping and gas recycling, the final gas mass is $\lesssim 10^7$ $M_\odot$, below the ALFALFA detection limit. Additionally, Boselli et al. (2008a) predict that such galaxies should have significantly less HI than the relatively unstripped LTDs in Virgo

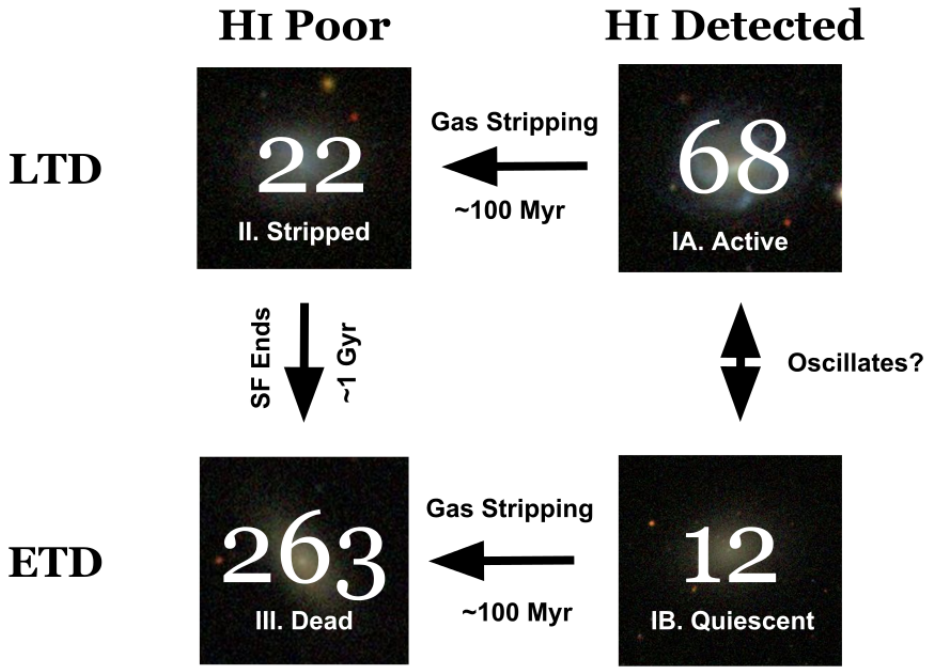

Figure 2.10: Schematic diagram of cluster dwarf galaxy evolution for the bursty star formation gas hypothesis. Stages I-III are identical to 2.8. Because the star formation in these low-mass galaxies may be erratic, there may be long periods of time (> 1 Gyr) in which these galaxies—while gas-rich—do not form any stars, putting the galaxy in the quiescent Stage IB. Gas stripping may occur in either Stage IA or IB. But, if the galaxy is stripped in Stage IB, no residual star formation occurs, sending the galaxy straight to Stage III: red and dead.

of the same stellar mass, instead we observe similar masses of HI in both populations.

2.4.3 Bursty Star Formation and Dwarf Transitionals

It has long been understood that dwarf galaxies can have highly variable star formation rates, both because the number of stars being formed in the galaxy at any one time is small (and thus subject to small number statistics), and due to the possible strong effects of feedback mechanisms such as winds and supernovae, which expel gas and quench star formation (e.g.

Gerola et al. 1980; Dekel and Silk 1986). Between major star formation events, many of the massive (greater than a few solar mass) stars will die out, removing the UV and Hα emission used as a star formation tracer. If the period between the events is long enough, the galaxy will become red, even though it still contains significant HI reservoirs. We may simply be observing the red ETDs between major star formation events, as shown in Figure 2.9.

Dwarf transitionals are galaxies in group environments which are identified in a similar way to our red ETDs: they have M_{HI}/L_B properties to dwarf irregular galaxies, but have little to no star formation (Mateo 1998). Explanations for these transitional galaxies typically fall into two categories: there's been some strong tidal interaction with its host galaxy ("tidal stirring"; Mayer et al. 2001a; Mayer et al. 2001b), or these low mass galaxies are in a quiescent period between major star formation events (e.g. Skillman et al. 2003). Recent evidence suggests that the true answer may lie in a combination of the two, especially for those transitionals with significant gas reservoirs (i.e. $\log M_{HI}/M_* > -1$). However, two key features distinguish the red ETDs from typical transitional dwarfs: their mass properties and their UV-measured star formation rates.

Weisz et al. (2011) studied the detailed star formation history of 60 nearby dwarf galaxies ($d < 4$ Mpc) observed as part of Hubble's ACS Nearby Galaxy Survey Treasury (ANGST), including 12 dwarf transitional galaxies. Figure 2.11 shows the gas fraction-stellar mass relationship of the ANGST dwarf transitionals in comparison to our ETDs. Symbols are identical to Figure 2.5, with the addition of the dwarf transitionals of Weisz et al. (2011), represented by filled purple boxes. For the most part, the dwarf transitionals are significantly lower in both gas fraction and stellar mass than the red ETDs. Only one (UA438) stands out as having the same range of both stellar mass and gas fraction, although DDO6 and KDG52 are close. These dwarf transitionals may be the link between dwarf irregulars and dwarf spheroidals. If our red ETDs are a type of transition galaxy, they are the link between

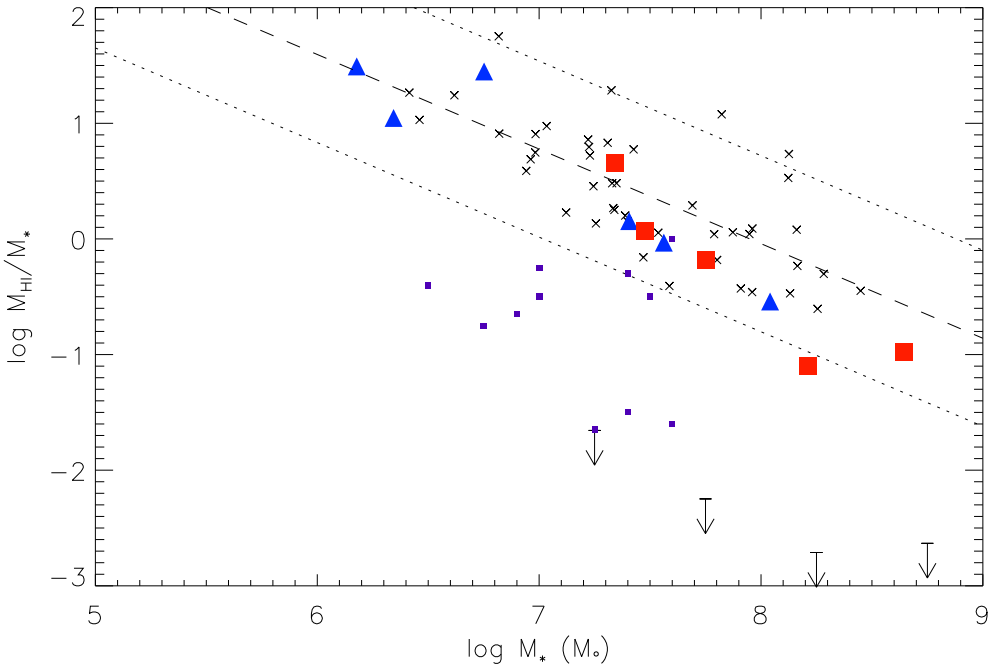

Figure 2.11: Gas fractions and stellar masses of dwarfs in the Virgo cluster plus 12 local dwarf transitionals studied by Weisz et al. (2011). Symbols are identical to Figure 2.5. Filled purple boxes are dwarf transitional galaxies.

more massive galaxies, possibly faint spirals and dwarf ellipticals.

Additionally, transition dwarfs are generally identified as having no recent star formation using Hα imaging. Hα emission traces formation of massive (10-15 $M_*/M_\odot$) stars, and is thus only a reliable tracer of star formation more recent than a few dozen Myr. Ultraviolet emission tracers lower mass stars, and thus gives a picture averaged over the last few hundred Myr—highly important when dealing with a group of galaxies which may have highly stochastic star formation histories. Lee et al. (2011), studying galaxies in the local universe using GALEX NUV/FUV imaging, found that low-mass dwarf galaxies not detected in Hα were commonly detected in the NUV/FUV GALEX bands, and had implied star formation rates similar to the Hα detections. Our star formation rates are based on UV, rather than Hα, photometry, and yet we still find that the red ETDs have very low SFRs compared

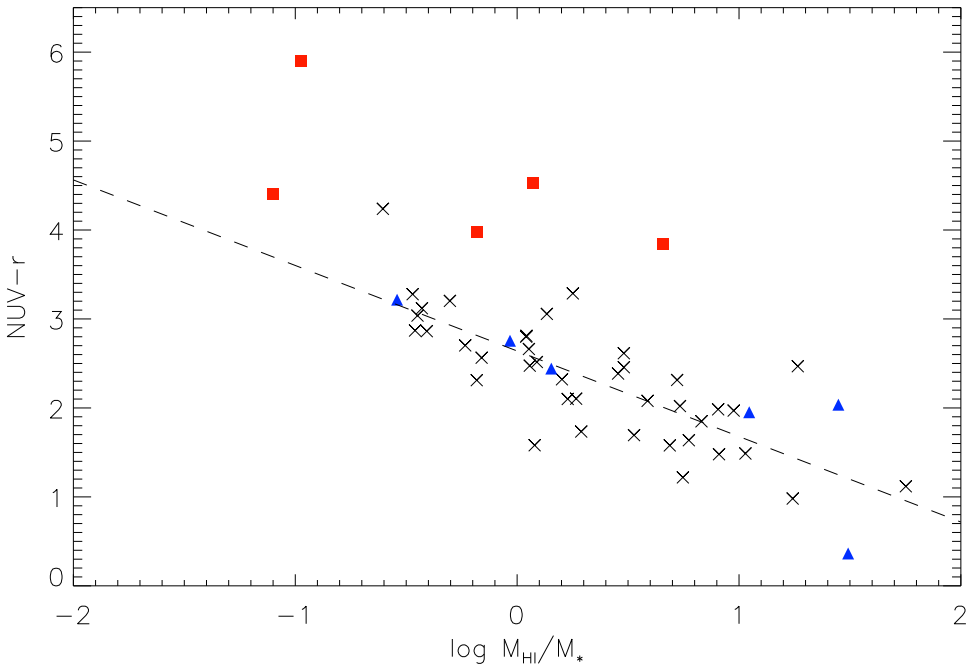

Figure 2.12: NUV$-r$ color as a function of HI gas fraction, with the same symbols as Figure 2.4. The blue gas-bearing ETDs and LTDs form a clear line, with best-fit line plotted. The red ETDs have higher gas fraction than their NUV$-r$ color would indicate. Catinella et al. (2010) suggest that significant outliers, such as the red ETDs, are strong candidates for galaxies transitioning to or from the red sequence and blue cloud.

to galaxies of similar HI and stellar masses. So, while the dwarf transitionals may be between major star formation episodes, the red ETDs appear to have been depressed for longer periods of time prior to our observations.

2.4.4 Re-Accreted Gas

Catinella et al. (2010) and Cortese et al. (2011) found a tight relationship between HI gas fraction, NUV$-r$ color, and stellar mass surface density, with NUV$-r$ being the best indicator of M_{HI}/M_*. Outliers are galaxies which are either forming too many or too few stars for their gas mass and are indicative of transition objects. More massive galaxies which are

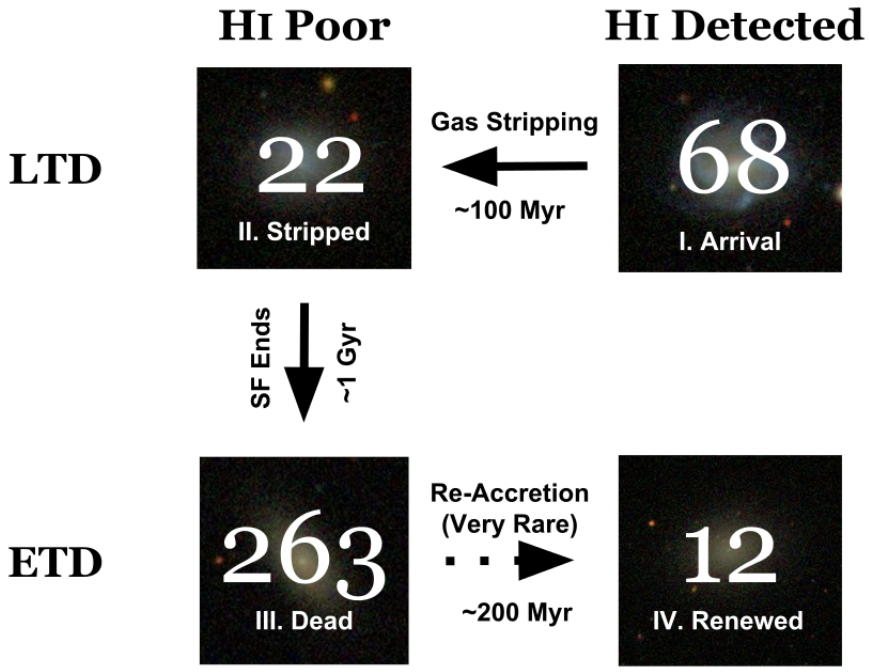

Figure 2.13: Schematic diagram of cluster dwarf galaxy evolution for the reaccreted gas hypothesis. Stages I-III are identical to 2.8. In a rare set of circumstances, an evolved galaxy may encounter and capture an intergalactic mass of gas which is falling onto the cluster, moving it from Stage III to Stage IV. This gas may be only loosely bound to the galaxy, and may take a very long time to reignite star formation.

very red in NUV−H color which are otherwise HI normal show indication of recent mergers or gas accretion (Cortese and Hughes 2009). Figure 2.12 plots the gas fraction as a function of NUV−r color for all HI detections in Virgo. The blue ETDs and LTDs form a distinctive line with a best-fit line plotted. The red ETDs are all very strong outliers with high HI mass but low star formation: could they be reaccreting gas? Figure 2.13 shows a schematic overview of this process.

Dwarf galaxies in the Virgo cluster tend to be on highly eccentric, nearly free-fall orbits. The majority of such orbits will be spent relatively far from the cluster core, where neutral gas from the cosmic web will also be falling onto the cluster. At their furthest distance

from the cluster, they will be moving at low velocity with respect to the cluster and distant gas, and while falling back into the cluster will have velocities similar to that of gas which is also free-falling onto the cluster. We can then follow the argument of Wei et al. (2010), who examined a sample of low mass ($M_* < 10^{10} M_\odot$) elliptical galaxies that appeared to be accreting gas in the field, and use the dynamical timescale to get a rough idea of the time needed to accrete gas. As HI in these sources is unresolved by ALFALFA (beam ∼4'), we don't know the actual size of the gas clouds accreted. I choose half the Arecibo beam size at the distance of Virgo (∼5 kpc) as an upper bound, and the optical sizes of the galaxies (∼1.7 kpc) as a lower bound. Assume that the total mass, accounting for dark matter content, is ∼10 times the baryonic content of the stars, HI, and Helium (∼30% of the HI) together. We can then make an estimate of the gas infall time (Binney and Tremaine 2008) as

$$t_{\rm infall} \simeq \sqrt{\frac{\pi R^3}{G \times 10(M_* + 1.3 M_{\rm gas})}} \tag{2.1}$$

We get infall times for our sample that range from 24-470 Myr (see Table 2.2). Given that most of the time of the galaxy's 1.5 Gyr orbit is spent at the outskirts of the cluster, these accretion timescales are all quite reasonable.

But the Virgo ETDs galaxies are not isolated systems like those of Wei et al. (2010), but rather are found in a cluster where the hot ICM will inhibit accretion and cooling of gas. Figure 2.14 shows the location of all HI detected ETDs in our sample with overlaid 3σ and 5σ X-ray contours (in the 0.4-2.4 keV range) from Böhringer et al. (1994). The dashed line indicates the onset of confusion with the north polar spur, an X-ray feature of the Milky Way, and only contours associated with Virgo are plotted. As with Figure 2.4, the plates of Binggeli et al. (1985) and a 1° circle around M87 are plotted for reference. The 3σ contour of the ROSAT map corresponds roughly to where the cluster hard ($0.4 - 3$ keV) X-ray flux is half of the background hard X-ray flux, with fluxes falling off as a power law (Urban et al. 2011). Of the 12 detections, 9 are at or clearly beyond this distance. Two of the exceptions,

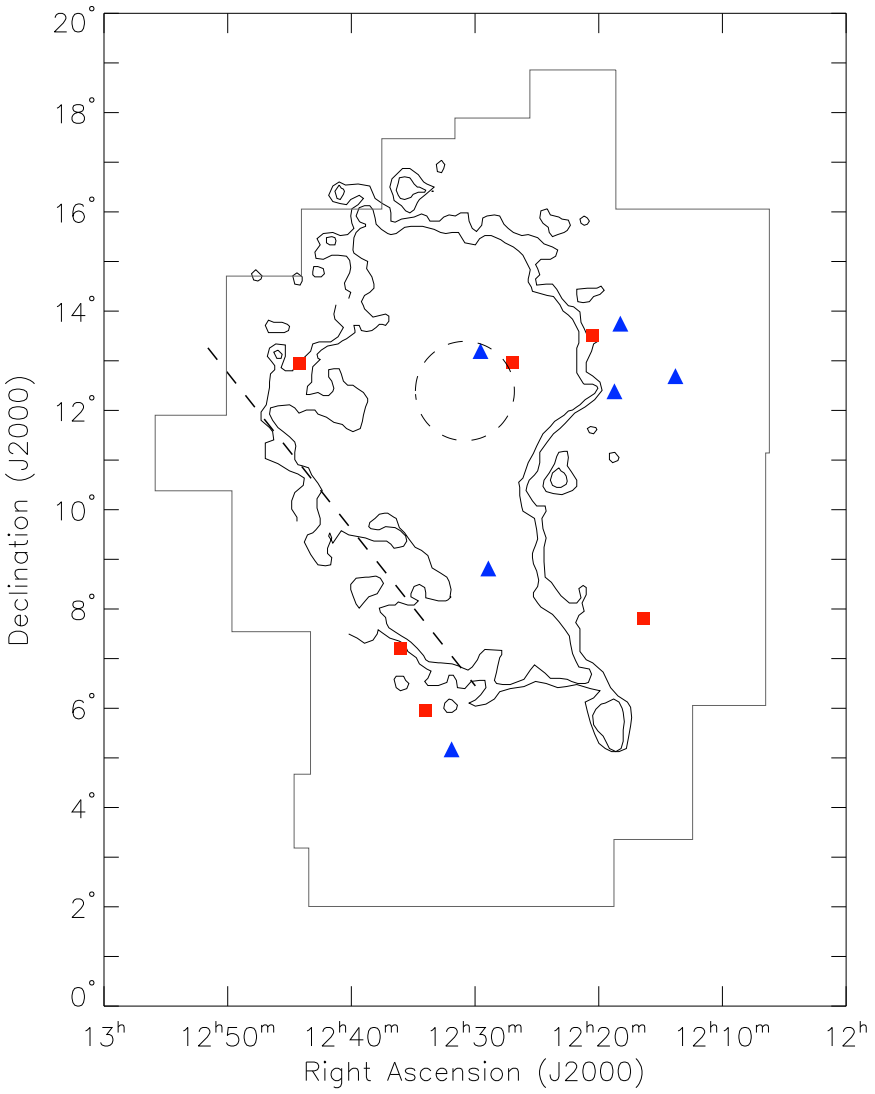

Figure 2.14: Locations of the $\alpha.40$-detected early-type dwarfs. Blue triangles are the blue subclass, while red squares are the red subclass. Contours are the 3σ and 5σ detection limit of Rosat X-ray observations in the $0.4 - 2.4$ keV energy range (Böhringer et al. 1994). Only contours associated with Virgo are plotted. The dark dashed line indicates onset of confusion with X-ray features of the Milky Way. The dashed circle indicates a 1° ring around M87, which is responsible for $\sim$71% of the X-ray emission.

VCC 956 and 1202 are projected very close to M87 where the X-ray luminosity is very high; they may however be located far from the core, only projected onto M87. Likewise, VCC 1142's projected position puts it in a region of strong emission. For all three galaxies, we cannot be sure of how embedded they are in the ICM. For the other galaxies, we can make a rough estimate of how long it would take for the X-ray gas to evaporate accreting gas (Cowie and McKee 1977; Cowie and Songaila 1977)

$$t_{\rm ev} \simeq 4.6 \times 10^3 \text{ yr} \left(\frac{M_{\rm HI}}{M_\odot}\right) \left(\frac{R_{\rm HI}}{\rm kpc}\right) \left(\frac{T}{10^6 \text{ K}}\right)^{-5/2} f_{\rm mag}^{-1} \tag{2.2}$$

Where R_{HI} is the radius of the cloud (again, either 1.7 or 5 kpc), T is the temperature of the ICM medium, assuming an upper limit of 1.08 keV at 3.9° from M87 (Urban et al. 2011). $f_{\rm mag}$ measures how the entanglement of the magnetic fields in the ICM quenches heat transfer; it is expected to be of order $\lesssim 1/3$ (Sarazin 1986). With the exception of the low HI mass galaxy VCC 1649, the estimated evaporation times are 121-721 Myr (see Table 2.2), typically larger the dynamical infall times.

So, the gas-bearing ETDs are generally outside radii from the cluster core where the cluster's X-ray emission dominates, their dynamical infall rates are significantly less than cluster crossing times and typically less than the lower-limit time for the X-ray medium to evaporate the cool gas, making recent accretion a definite possibility for all but four of the dwarf ETDs (the three inside significant X-ray emission, and the low HI mass VCC 1649). For the red subclass of gas-bearing ETDs, recent accretion is also the only evolutionary history of the three discussed which can adequately explain their optical, UV, and HI properties.

2.5 Conclusions

I examined the sample of all 365 VCC dwarf ($M_B > -16$) galaxies with known redshifts. While not as sensitive as observations targeting individual galaxies, ALFALFA's blind coverage gives us a statistically complete view of the atomic gas content of the Virgo cluster population, both for detected and non-detected galaxies. I use ALFALFA's current $\alpha.40$ (Haynes et al. 2011) data release, which expands the previous Virgo coverage (Giovanelli et al. 2007; Kent et al. 2008) to declinations $4^\circ < \delta < 16^\circ$. Of the 365 dwarf galaxies, 80 are detected in HI in the $\alpha.40$ catalog. As is to be expected, a large fraction of these galaxies (68 out of 80) are late-types and peculiar galaxies, but 12 are classified as early-types by the VCC.

The gas-bearing population of dwarf galaxies show a clear tendency to avoid the regions of Virgo closest to M87 and M49. Despite being early-type galaxies, the HI-detected ETDs have HI gas fractions similar to the HI-detected LTDs of the same stellar mass. However, the upper limit on the gas fraction for the non-detected ETD population is approximately 2.5 dex lower than the HI detected dwarfs, and there does not appear to be a significant population bridging the gap between the gas bearing and the gas poor populations.

In agreement with Lisker et al. (2007) and Kim et al. (2010), I find that the dwarf ellipticals follow a tight color-magnitude relation with bluer $g - r$, NUV$-r$, and FUV$-r$ colors at fainter M_r. The HI-detected late-type dwarfs trace a very broad distribution which is well-separated from the red sequence in $g - r$ (0.4 magnitudes); the separation is larger in NUV$-r$ and FUV$-r$ (2 and 4 magnitudes, respectively). The HI detected ETDs are unusual in that they do not as a class sit wholly in either the red sequence or blue cloud: half are clearly red while the other half are blue. The blue gas-bearing ETDs have SSFRs and SFEs similar to the LTDs, while the red ETDs typically have rates a few dex lower than

the blue subclass. The fact that the blue ETDs seemingly have properties identical to the LTDs, except that they are typically fainter, suggests that there may a mis-classification of the blue ETDs, and that the two populations are actually one.

Lastly, we consider the various possible evolutionary histories of the bas-bearing ETDs. It is likely that the blue ETDs are on their first pass through the cluster—either because they are only recently disturbed or are so faint that they are actually LTDs mistakenly classified as ETDs. VCC 281 stands out from the other blue ETDs in that it has a 'blue-center' suggestive of a disk galaxy evolved by galaxy harassment but is also consistent with ram pressure stripping. However, stripping cannot explain the red subclass of ETDs, which are gas-rich but not forming stars. Models of gas returned into the ISM by stars at the end of their lives (Boselli et al. 2008a) cannot account for the mass of HI observed in either the blue or red subclass. Additionally, they appear to be too massive, gas-rich, and forming stars too inefficiently to be similar to dwarf transitionals (Lee et al. 2011; Weisz et al. 2011): only one of the dwarf transitionals in the sample of Weisz et al. (2011) has a gas mass and gas fraction similar to our sample.

The gas-bearing red ETD subset is most consistent with having already traveled through the cluster core, been stripped, and now at lying the edge of the cluster where HI is being accreted from the cosmic web. All of the red ETDs, with the exception of VCC 956 ($\sim 1^\circ$ from M87), are in a region of the cluster where the dominant hard X-ray flux arises from background sources, rather than the ICM. The dynamical timescales for these galaxies to re-accrete their gas are significantly less than one orbital time and typically larger than the time it would take the ICM to evaporate the newly accreted gas.

CHAPTER 3

THE HIGHMASS SAMPLE

3.1 Introduction

In the standard hierarchical clustering framework of ΛCDM cosmology, smaller halos form first, with dark matter halos merging to produce progressively larger structures (for a recent review, see Baugh 2006; Benson 2010)[1]. Galaxies form as these halos accrete gas: either shocked as it falls into the halos in a so-called 'hot-mode' accretion or along cold filaments of gas which never shock in 'cold-mode' accretion (e.g. Kereš et al. 2005).

Observationally, in a mechanism known as 'down-sizing', at high redshifts the most massive galaxies are the most efficient at forming stars (Cowie et al. 1996), with bursts of star formation triggered via mergers of gas-rich disks at high redshift. By $z \sim 0$ galaxies with high stellar masses tend to have relatively low gas fractions (GF$\equiv$M$_{\rm HI}$/M$_*$) compared to less massive galaxies (e.g. Catinella et al. 2010; Cortese et al. 2011; Huang et al. 2012a). For an optically selected field galaxy sample with M$_* > 10^{10}$ M$_\odot$, typical gas fractions are $0.01 <$ GF < 0.1 (e.g. Cortese et al. 2011). At these stellar masses, significantly more gas-rich galaxies are expected to be quite rare, as was found in previous blind HI surveys such as HIPASS (Zwaan et al. 2005).

One of the most surprising results of ALFALFA (Giovanelli et al. 2005) is the detection of a significant population of massive galaxies which are also extremely gas rich (Martin et al. 2010; Haynes et al. 2011). From ALFALFA, we have identified the HIghMass sample: 34 galaxies with high HI mass (M$_{\rm HI} \gtrsim 10^{10}$ M$_\odot$) which are also the most gas-rich (GF $\gtrsim 0.4$)

[1]This introduction has been excerpted from Hallenbeck et al. (2014), which will appear shortly in the AJ.

for their stellar masses. Over half of this sample has GF > 1. How do such massive galaxies acquire and maintain substantial reservoirs of gas? We consider two possibilities.

One possibility is that the gas is recently acquired. This recent gas may be from a 'galactic fountain' of gas previously ejected by supernovae raining back down (Shapiro & Field 1976; Bregman 1980), from accretion of many small companion galaxies, or from accretion of pristine gas along filaments. It is not clear what percentage of the gas comes from each source, although simulations suggest that the majority of gas comes from cooling previously ejected gas, with a smaller—but not negligible—amount coming from cold or hot-mode accretion (Fraternali and Binney 2006; Fraternali and Binney 2008; Oppenheimer et al. 2010). Regardless of whether such processes dominate, such infalls do not appear to have strong short-scale star formation or stability effects on galaxies but over long times refuel the disk's potential for star formation (Hopkins et al. 2013). Unfortunately, these effects are difficult to find observationally. Direct observation finds gas inflow rates of $\dot{\mathrm{M}} \sim 0.2$ $\mathrm{M}_{\odot}$ yr^{-1} in local spiral galaxies, a factor of $5-10$ less than is required to sustain star formation (Sancisi et al. 2008). However, rates of both HI and unobserved ionized gas $\dot{\mathrm{M}} \sim 1-3$ $\mathrm{M}_{\odot}$ yr^{-1} have been indirectly inferred (Fraternali and Binney 2008).

The second possibility is that the gas is old, but has not been able to form stars. Answers may lie in the HIghMass galaxies' spin parameter λ (Peebles 1971), a dimensionless measure of the halo's angular momentum and oft-cited governing mechanism of a galaxy's evolution. Simulations and theory predict that at fixed total mass, galaxies in the local universe with higher spin parameters are bluer, have lower surface brightness, and are more gas-rich (e.g. Jimenez et al. 1998; Mo et al. 1998; Boissier and Prantzos 2000; Macciò et al. 2007). Unfortunately, the dynamics of the dark matter content of a galaxy are not directly observable, and a number of assumptions are required about the relationship between the spin parameter of the galactic disk (λ_d) and that of the halo; however, this overall trend appears to

be confirmed for inferred spin parameters (e.g. Hernandez et al. 2007; Cervantes-Sodi and Hernández 2009; Huang et al. 2012a). If the HIghMass galaxies have unusually high spin parameters, then this gas may be be unable to efficiently form stars.

This chapter is a brief motivation of how the HIghMass galaxies were selected (§3.2), and also places these galaxies in the context of the larger ALFALFA survey population (§3.3). The chapter ends with a description of our observation strategy for observing gas in these galaxies in §3.4. A complete definition of this sample and a more in-depth comparison with the ALFALFA population can be found in Huang et al. (2012a) and Huang et al. (2014, in review).

3.2 Gas Fractions

Figure 3.1 presents the gas fractions of the galaxies in the ALFALFA $\alpha.40$ data release as a function of their fitted stellar masses (from Huang et al. 2012a). The general trend is that more massive (higher M_*) galaxies typically are less gas rich. This matches both the expectations of both hierarchical clustering theory and the "down-sizing" seen observationally.

However, ALFALFA is highly biased towards the most HI-rich galaxies: gas poor galaxies simply aren't detected in ALFALFA. If we compare to a sample of "HI-normal" galaxies identified by their optical properties (the green line; Cortese et al. 2011), we see that at every stellar mass, ALFALFA galaxies are typically more gas-rich by 0.5 dex. If we examine the gas-rich ALFALFA outliers, we observe galaxies even at the very high HI mass end ($M_{HI} > 10^{10}$ $M_\odot$) with high gas fractions (some > 1). Such galaxies have gas fractions which are 1.0 dex higher than "HI-normal" galaxies of the same stellar mass. Put another way, one would have to look 2.0 orders of magnitude lower on the stellar mass scale to find

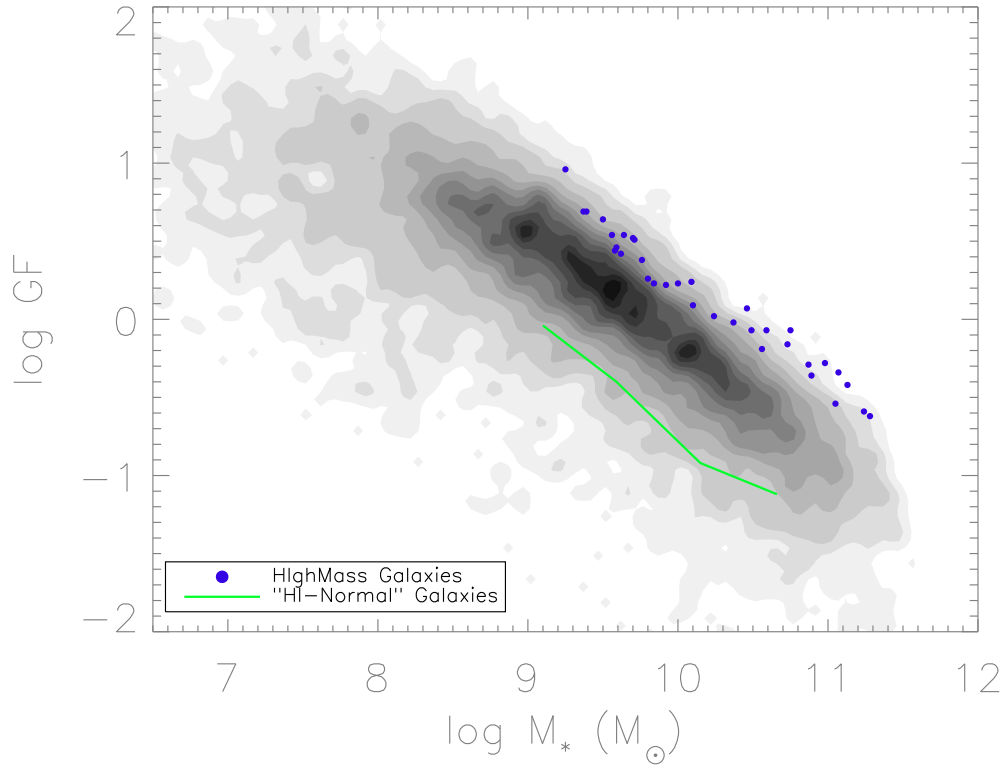

Figure 3.1: HI gas fraction of ALFALFA galaxies plotted as a function of stellar mass. The green line shows the "HI normal" galaxies of Cortese et al. (2011). Dark blue points indicate the HIghMass galaxies.

"HI-normal" galaxies with similar gas fractions.

This small fraction of galaxies, which are both HI-massive ($> 10^{10}$ $M_{\odot}$) and also extremely gas-rich for their stellar masses ($> 1\sigma$ above the trend for the other $\alpha.40$ galaxies), are the HIghMass sample. The HI and optical properties of these galaxies are summarized in Table 3.1, found at the end of this chapter. In all, there are 34 such galaxies, out of the 15041 galaxies in the $\alpha.40$ data release. Galaxies in bold in the table are examined in detail later in this thesis.

3.3 Star Formation Properties

Figure 3.2 presents the star formation properties of the ALFALFA $\alpha.40$ data release (star formation rates from Huang et al. 2012a) as a function of stellar mass. The top panel presents specific star formation rates, or star formation rates normalized by stellar mass (SSFR$\equiv$SFR/M_*). The general trend of the ALFALFA galaxies is towards lower SSFRs at higher stellar mass (with a kink near $10^{9.5}$ $M_\odot$), and at the highest stellar masses, many galaxies drop off of the trend toward extremely low SSFRs. In general, the HIghMass galaxies sit at or just above the ALFALFA average trend (red line). The only outlier is UGC 4599, which unlike the rest of the HIghMass sample, is an elliptical, rather than spiral galaxy.

The bottom panel of Figure 3.2 presents the star formation efficiencies, or star formation rates normalized by HI mass (SFE$\equiv$SFR/M_*). Here we expect (and observe) a slow rise in SFE with stellar mass: the more massive galaxies are more efficient at converting gas into stars and, at the current star formation rate, will deplete their gas in much less time than less massive galaxies. Once again, at high masses ($\gtrsim 10^{9.5}$ $M_\odot$), for some galaxies star formation appears to be unregulated by the total HI mass, and have very low SFEs. The HIghMass galaxies (again, with the exception of UGC 4599) are typically just at or below the bulk of the ALFALFA sample (red line). In comparison with an optical sample with similar stellar masses (cyan dashed line; the GASS sample of Catinella et al. 2010), the HIghMass galaxies are even more inefficient in their star formation.

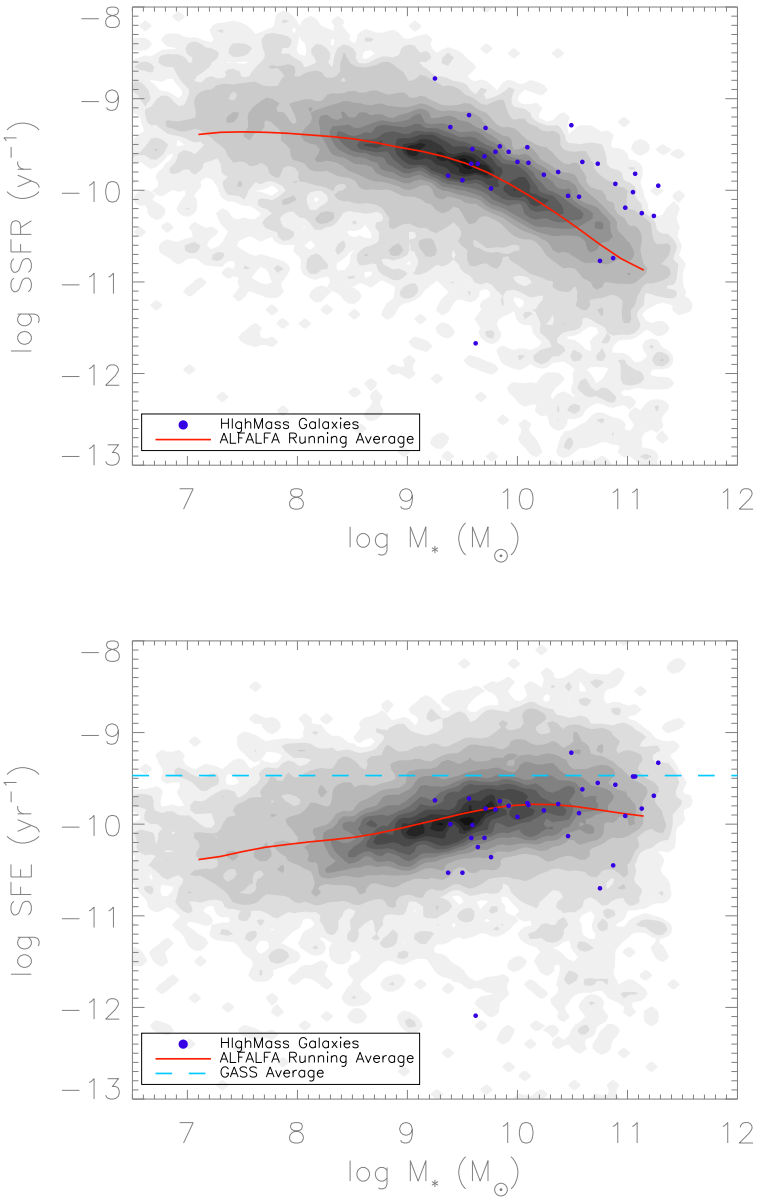

Figure 3.2: Specific star formation rates (SSFR≡SFR/M_*; above), and star formation efficiencies (SFE≡SFR/M_{HI}; below) of the galaxies in the α.40 sample. The red line is the moving average value. HIghMass galaxies are shown as dark blue points.

3.4 Observations and Strategy

In order to begin probing the evolutionary histories of these galaxies, the HIghMass team is performing follow-up observations (and examining archival data) at many different wavelengths: KPNO Hα and GALEX UV observations to trace star formation, SDSS optical to trace the stellar component, Herschel submillimeter observations to observe dust, and so on.

I am heading the effort to examine the resolved HI and H_2 (via CO, a common tracer) gas in these galaxies. HI is the best tracer of a galaxy's rotation out to large radii, and helps us the underlying dark matter distributions of each galaxy. Before star formation can occur, HI first is converted to cold, dense H_2. Molecular hydrogen is thus the best tracer for potential future star formation, and will answer whether the galaxies aren't forming stars efficiently because HI isn't being converted to H_2, or because H_2 is unable to finally collapse into stars.

There are 34 galaxies in the HIghMass sample, and for a resolved gas study, several hours of telescope time are needed to reach the required sensitivity for each galaxy. Our coverage has therefore been heterogeneous, and spread out amongst several different facilities. HI synthesis observations were performed using three facilities: the Karl G. Jansky Very Large Array (VLA)[2], the Giant Metrewave Radio Telescope (GMRT)[3], and the Westerbork Synthesis Radio Telescope (WSRT)[4]. In addition, five galaxies have been observed at the Combined Array for Research in Millimeter Astronomy (CARMA), using the ^{12}CO(1-0) line as a tracer of molecular Hydrogen (H_2). In Columns 9 and 10 of Table 3.1, I present the resolved HI and CO follow-up observation status of each of the HIghMass galaxies. In the

[2]The VLA is owned by the National Radio Astronomy Observatory (NRAO), a facility of the National Science Foundation operated under cooperative agreement by Associated Universities, Inc.

[3]The GMRT is operated by the National Centre for Radio Astrophysics of the Tata Institute for Fundamental Research (NCRA-TIFR), a national center of the Government of India.

[4]WSRT is a facility of ASTRON, the Netherlands Institute for Radio Astronomy

Galaxy	log M_{HI} $M_\odot$	log M_* $M_\odot$	W50 km s^{-1}	v km s^{-1}	d Mpc	GF	log SFR $M_\odot$ yr^{-1}	HI	H_2
(1)	(2)	(3)	(4)	(5)	(6)	(7)	(8)	(9)	(10)
188749	10.14	9.50	136	10972	160	4.37	-0.39	G	
4599	10.04	9.62	148	2071	32	2.63	-2.05		
190796	10.14	9.76	123	8895	131	2.38	-0.22		
721391	10.07	9.84	293	7537	112	1.70	0.32		
190277	10.22	9.70	286	8658	128	3.28	0.07		
5543	10.73	11.07	547	13737	201	0.46	1.25	V	
5648	10.14	9.92	322	6862	103	1.66	0.34		
5711	10.51	11.05	522	6253	94	0.29	1.03	V	
203522	10.21	9.25	190	10886	160	9.20	0.47	G	
6043	10.06	9.80	276	8148	121	1.81	0.22		
6066	10.71	11.13	667	11807	174	0.38	0.88	V	
6168	**10.35**	**10.37**	**363**	**8073**	**120**	**0.95**	**0.57**	**V**	**C**
6536	10.58	10.87	430	6962	104	0.51	0.13	W	
6692	10.37	10.56	390	6060	203	0.65	0.49		
213964	10.08	9.39	88	9876	146	4.95	0.08	G	
6895	10.65	11.24	490	6389	96	0.25	0.96	G	
6967	10.23	10.00	253	3453	52	1.70	0.31		
7220	10.52	10.59	443	8102	120	0.86	0.90	V	C
7686	10.22	9.71	273	7510	112	3.21	0.39	G	C
7899	**10.42**	**10.49**	**433**	**8696**	**129**	**0.85**	**1.20**	**V**	**C**
8089	10.06	9.37	117	7142	106	4.90	-0.47	G	
8408	10.26	10.24	290	7303	108	1.04	0.41		
8475	10.66	11.28	591	6835	102	0.24	1.33	G	
8573	**10.53**	**10.89**	**152**	**6857**	**102**	**0.44**	**0.96**	**G**	**C**
8797	10.70	10.98	559	17104	248	0.53	0.79	V	
9023	10.05	9.59	231	7203	106	2.87	0.04		
248881	10.10	9.56	192	7660	113	3.44	0.38		
9037	**10.33**	**10.09**	**294**	**5939**	**88**	**1.75**	**0.56**	**V**	
726428	10.02	9.58	208	8892	130	2.73	-0.13		
9234	10.68	10.75	589	10890	158	0.85	-0.02	W	
9334	10.57	10.73	413	7493	110	0.70	1.02	V	
714145	10.18	9.64	208	8892	121	3.44	-0.07		
9410	10.19	10.10	317	8421	123	1.24	0.40		
12506	**10.53**	**10.46**	**457**	**7237**	**98**	**1.18**	**0.40**	**V**	

Table 3.1: The 34 Galaxies of the HIghMass sample, including HI properties and follow-up observation status of each. Bolded galaxies are examined in-depth in this thesis. HI properties and distances are taken from Haynes et al. (2011). Column 1: AGC number of galaxy; Column 2: HI mass; Column 3: stellar mass, from Huang et al. (2012a); Column 4: Velocity width at half of peak emission; Column 5: heliocentric recessional velocity, in the optical convention; Column 6: distance to galaxy; Column 7: gas fraction, defined as M_{HI}/M_*; Column 8: star formation rate, from Huang et al. (2012a); Column 9: HI synthesis observation status, observed using either the (V)LA, (G)MRT, or (W)SRT or not observed (blank); Column 10: CO (tracer for H_2) synthesis observation status, observed using (C)ARMA or not observed (blank).

next Chapter, I present a brief sketch of the data reduction and analysis methods that I employ for these resolved gas studies.

CHAPTER 4

SYNTHESIS OBSERVATIONS & DATA REDUCTION

This chapter is an overview of the data reduction methodology used to obtain the results in Chapters 5 and 6. This chapter includes a description of my methods: I summarize our observations in §4.1, present the basic data pipeline is in §4.2, and give overviews of how numerical measures are obtained in §4.3. A much more in-depth discussion can be found in Appendix A.

4.1 Observations and Observing Strategy

This section is an extremely brief overview of the concepts of radio interferometry observations. A more thorough discussion of the basics of radio interferometry can be found in Thompson (1999).

The most simplistic description of a radio interferometer is that it is a number of radio receivers which work together to act as a single radio telescope with much higher resolution. An individual dish has a resolution $\theta \sim \lambda/D$, where λ is the wavelength of observation and D is the diameter of the telescope. An interferometer has a resolution of $\theta \sim \lambda/b$, where b is a typical distance between two receivers.

The basic data products of interferometer observation are known as visibilities. The signals received at every individual dish are sent to a correlator at a central location. Because each receiver is at a different physical location, they each measure a slightly different phase from the source in the sky, even if the source is emitting perfectly coherently (see Figure 4.1). The correlator multiplies and time averages every pair of observations (a "baseline")

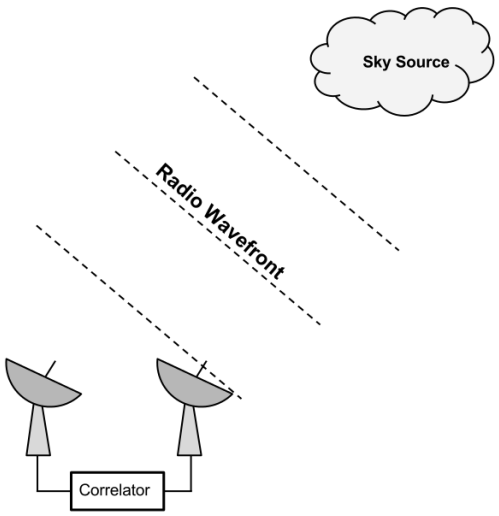

Figure 4.1: Schematic of radio interferometry with two dishes (and thus one baseline pair). The source in the sky emits radio waves, which reach Earth, with wavefronts depicted. The signals are transmitted to a central location where a correlator multiplies and time averages the signals from each individual baseline pair.

to get two quantities: an amplitude and a relative phase between the two receivers. Each baseline probes a Fourier component of the source's 2-D distribution, based on their distance and orientation.

Figure 4.2 shows a plot of the baselines for one two-hour observation block of UGC 9037. u and v are the east-west and north-south directions, respectively. Each point represents a single baseline pair (and thus, a sample of a single Fourier component). The "snowflake" pattern of the visibilities is a characteristic of the VLA, whose receivers are arranged in a Y-pattern, and the "smearing" of each point is due to the rotation of the Earth between individual integrations.

The CASA task CLEAN takes these visibilities and Fourier transforms them to produce a data cube. Two of the data cube's axes are the physical, in right ascension and declination on the sky, and the third is in frequency (or velocity space, for a known spectral line). Figure 4.3 is a channel map of UGC 9037, showing slices through its data cube at different

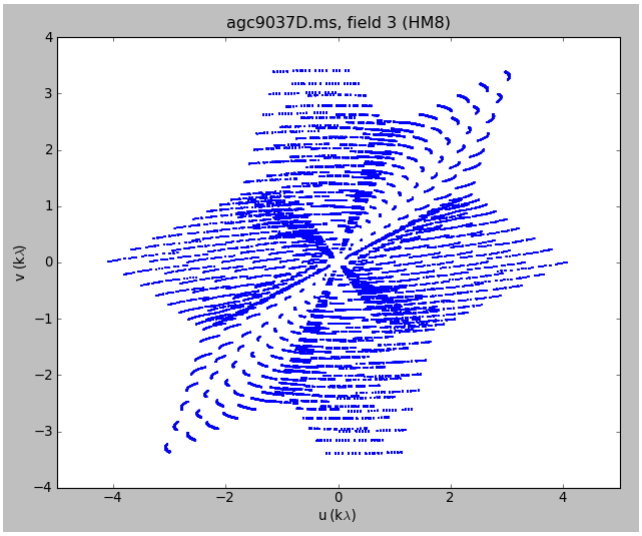

Figure 4.2: UV Coverage for a single two-hour observation block of UGC 9037. Each data point represents a baseline, integrated over a few minutes. u is east-west direction of baselines, v is north-south.

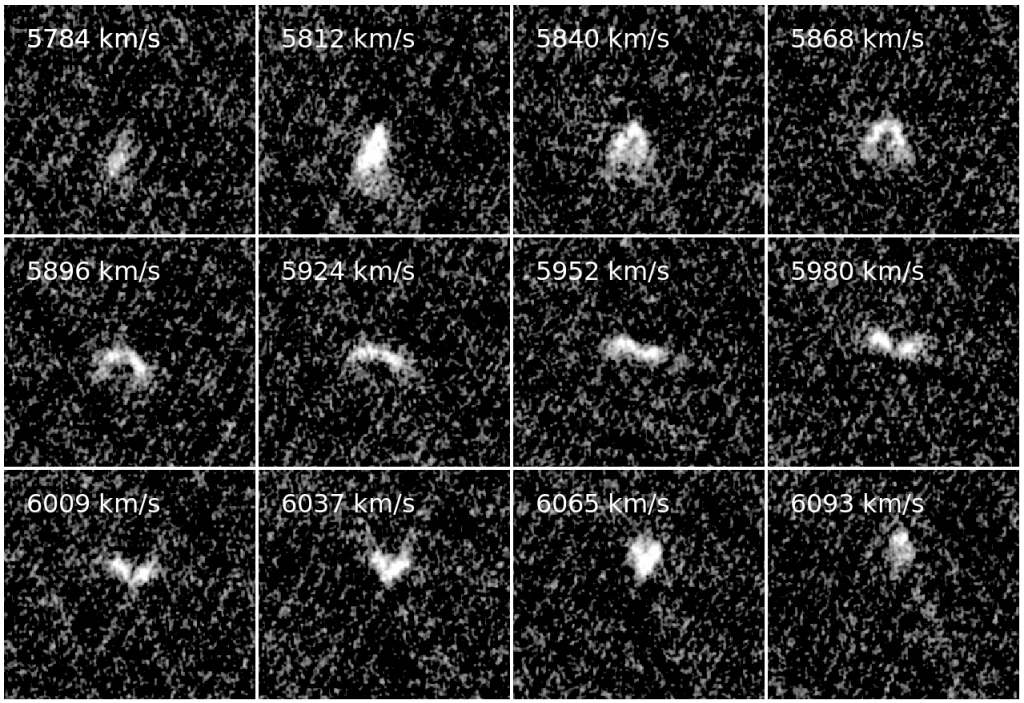

Figure 4.3: Channel maps of UGC 9037. Each shows the spatial structure of the galaxy at a particular velocity; each is separated by 28 km s^{-1}.

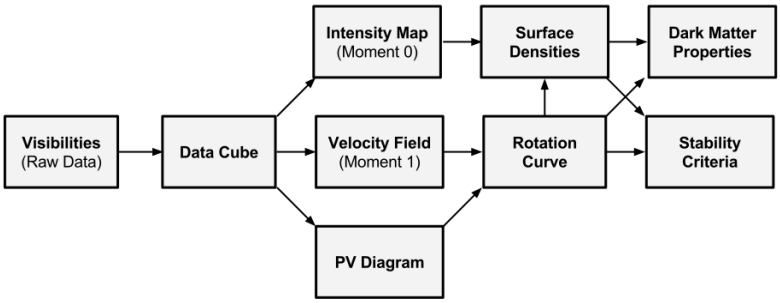

Figure 4.4: Schematic of our data reduction pipeline showing how the raw data (the visibilities) are used to create the data cubes, from which all of the data products are derived.

velocities. The HI in UGC 9037 is organized into a well-ordered rotating disk, yielding the classic "butterfly" pattern observed in its channel map.

4.2 Data Pipeline

Figure 4.4 shows a schematic overview of how each of the data products are related, from visibilities to data cubes to rotation curves. Data reduction is done mostly using NRAO's CASA[1] software. I use standard CASA routines to flag poor data, perform calibrations, and produce cleaned image cubes. CASA is also used to make moment maps. As CASA is still under development and is optimized for continuum, rather than spectral line analysis, I supplement CASA with the older GIPSY[2] software when necessary. GIPSY is used in fitting rotation curves and finding dark matter distributions.

[1]The Common Astronomy Software Applications package is under development by the NRAO.
[2]The Groningen Image Processing SYstem was developed at the Kapteyn Astronomical Institute.

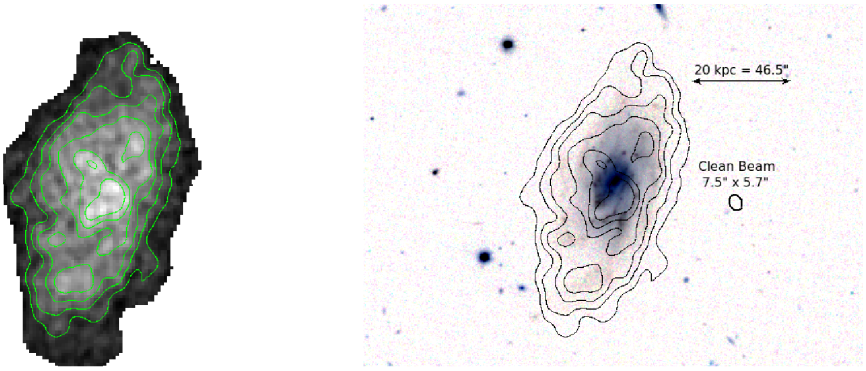

Figure 4.5: HI integrated flux map of UGC 9037. (left) Only the flux map, with contours overlaid. Contours begin at 4σ, with each each increase at 2σ. (right) Contours of the HI flux map overlaid onto an SDSS optical image of UGC 9037.

4.2.1 Moment Maps and Position-Velocity Diagrams

Because 3-D data cubes are difficult both to visualize and to operate on computationally, it is traditional to collapse the data along a particular axis, producing a 2-D map. I use three different types of 2-D representations of the data: integrated flux maps (or "moment 0" maps), velocity fields (or "moment 1" maps), and position-velocity (PV) diagrams.

An integrated flux map is simply a sum along the frequency axis of all of the emission in the galaxy, giving a quick spatial representation of where the gas in the galaxy is. The actual calculation of the flux map is actually slightly more complex than this: because the noise increases as $\sqrt{\text{channels}}$, I mask out regions where there is only noise and no emission, reducing the noise in the final image. Figure 4.5 (left) shows such an HI flux map of UGC 9037, with contours overlaid. One can quickly see from this map that the emission in the galaxy is peaked in the center, and its general orientation. If I add in an optical image (right), we can also measure how extended the HI emission is compared to the stellar light.

A velocity field is a weighted average velocity at each position in the galaxy. It gives a quick idea of whether the galaxy is rotating (as it should be for a spiral) or dominated by

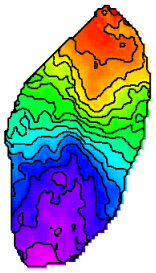

Figure 4.6: Velocity field of the HI of UGC 9037. Colors indicate velocity with isovelocity contours overlaid; each contour is a change by 20km s^{-1}.

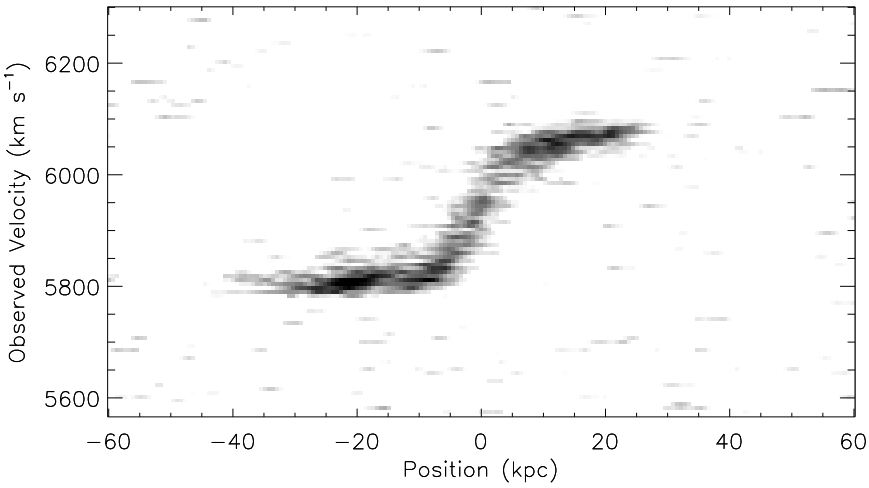

Figure 4.7: Position-Velocity Diagram of UGC 9037, taken along the major axis.

random motion (as happens in some gas clouds, galaxies with very low rotational velocities, and ellipticals). We can also look for deviations from smooth rotation. Figure 4.6 shows us the HI velocity field for UGC 9037. We can see that UGC 9037 appears to be rotating with a smooth gradient across the galaxy, with no warps or perturbations readily apparent. However, later we shall see with more complex analysis that the galaxy's disk is not to simple as it first appears.

A position-velocity diagram, instead of removing the frequency axis, removes a spatial

axis. Generally PV diagrams are aligned along the major axis of the galaxy, taking a "slice" through the cube. While showing a very different view than the velocity field, it gives much of the same information. However, its allow us for probing a more complex velocity structure that cannot be encompassed by a single value. Figure 4.7 shows the PV diagram for UGC 9037. We can see that the galaxy has a very smooth rotation, which increases nearly linearly from the center of the galaxy, until it reaches a maximum value and becomes flat.

4.3 Analysis

4.3.1 Rotation Curves

A rotation curve indicates the characteristic orbital velocity in a galaxy at a given radius from the center. In general, it is assumed that orbits in a galaxy are circular, with any deviation from circular orbits thrown into the catch-all category "non-circular motion," which encompasses everything from elliptical orbits to widespread inflows.

Tilted ring fits (GIPSY task ROTCUR) model the gas in each galaxy as a series of concentric rings, each of which can have an independent inclination (angle that the normal to the galaxy disk points away from the viewer), position angle on the sky (the alignment of the major axis of the galaxy, measured east of north), rotation velocity and a non-circular velocity. These tilted ring models are then compared to the velocity field of the galaxy, and adjusted until reasonable agreement is achieved. Tilted ring fits do an excellent job of fitting galaxies which have reasonably low inclinations ($i \lesssim 80°$), but for highly inclined galaxies, the velocity field is a poor tracer of a galaxy's velocity structure, and we fit directly on the PV diagram.

4.3.2 Mass Models

I treat each galaxy as being composed of up to five different components: HI, H_2, Helium, Stars, and Dark Matter. The Helium is assumed to be well-mixed with the hydrogen, and is merely a 1.33 multiplicative conversion factor to the HI and H_2 masses, and thus I only consider four independent components.

HI

Given the position angles and inclinations as derived from our rotation curves, it is straightforward to calculate deprojected HI surface densities. This is done by placing the rings from the tilted ring fits onto the integrated flux map, and averaging the intensity over each ring (using GIPSY task ELLINT). The intensity is then converted to total HI mass using standard methods:

$$M_{\rm HI} = 2.356 \times 10^5 \frac{S_{int}}{\rm 1Jy\ km\ s^{-1}} \times \left(\frac{d}{\rm 1Mpc}\right)^2 \tag{4.1}$$

where S_{int} is the integrated flux and d is the distance to the galaxy. The deprojected surface densities are simply a factor of $\cos i$ lower than the calculated value.

For highly inclined galaxies, this method is a poor estimate of the surface density, as each position on the sky will cross several rings. For this I use the Lucy method (Lucy 1974; Warmels 1988; GIPSY task RADIAL). Briefly, the Lucy method reduces the problem to one dimension by summing the integrated flux map along the minor axis of the galaxy, then iteratively producing models until one closely matches the observed sky flux distribution.

In addition to finding the surface density profile, I also measure a quantity known as the HI radius. Broeils and Rhee (1997) found a tight linear relationship between a galaxy's total HI mass (log $M_{\rm HI}$) and the diameter at which its deprojected surface density. This

relationship was later extended to higher gas-fraction objects of the 'BlueDisks' sample (Wang et al. 2013; see Equation 3 of Broeils and Rhee 1997):

$$\log R_{\rm HI} = 0.51 \log M_{\rm HI} - 3.63 \tag{4.2}$$

I calculate an HI radius for each galaxy by fitting an exponential profile to the HI density and using it to estimate the radius where where $\Sigma_{\rm HI} = 1$ M$_\odot$ pc^{-2}. For galaxies for which an exponential profile is inappropriate, I fit a straight line over a few channels where the surface density approaches 1 M$_\odot$ pc^{-2}.

Molecular Hydrogen (H_2)

For the H_2 masses, calculations are a bit more complex. One must assume a conversion factor between the observed CO luminosity $L'_{\rm CO}$ (in units of K km s^{-1} pc^2) and the total H_2 mass, known as $\alpha_{\rm CO}$. The conversion factor is known to vary significantly with metallicity and redshift (e.g. Wilson 1995, Arimoto et al. 1996). Even though the HIghMass galaxies are gas-dominated and have poor star formation rates, they all have stellar masses $\gtrsim 10^{10}$ M$_\odot$, and thus I expect them to have metallicities similar to the Milky Way. I thus follow Saintonge et al. (2011a) and use a Milky Way value for $\alpha_{\rm CO}$ averaged over several recent measurements (Strong and Mattox 1996; Dame et al. 2001; Blitz et al. 2007; Draine et al. 2007; Heyer et al. 2009; Abdo et al. 2010), $\alpha_{\rm CO} = 3.2 {\rm M}_\odot ({\rm K\ km\ s^{-1}\ pc^2})^{-1}$. Given the conversion factor, we can then compute the total H_2 mass following Solomon et al. (1997):

$$M_{\rm H_2} = L'_{\rm CO} \alpha_{\rm CO} = 3.25 \times 10^5 \alpha_{\rm CO} S_{\rm CO} \nu^{-2} d^2 \tag{4.3}$$

where $S_{\rm CO}$ is the total integrated CO flux in Jy km s^{-1} (which are our intensity map units) and ν is the rest frequency of the line in GHz, which for ^{12}CO(1-0) is 115.271 GHz. With this conversion made, the deprojected surface densities of H_2 can be calculated in a manner

analogous to that of HI, depending on whether the galaxy is nearly face-on, inclined, or nearly edge-on.

Stellar Masses

Compared to our global stellar mass estimates (Huang et al. 2012a; Huang et al. 2012b), finding from optical photometry a robust measure of how a galaxy's stellar mass distribution is more complex. Among other considerations, it requires an understanding of how the metallicity and extinction change with radius. However, our primary interest in a stellar mass density model is in determining its contribution to rotation curves in order to model each galaxy's dark matter content. Since the HIghMass galaxies have $M_{HI} \sim M_*$ and stellar mass is quite concentrated towards the center of galaxies compared to the gas, the accuracy of the local stellar mass model is less important than the total stellar mass. To that end, we roughly approximate stellar mass using the following method: elliptical apertures are fit to the optical SDSS image and corrected for Galactic extinction. Internal extinction is ignored because its variation with radius is unknown. Then, the magnitudes are converted into stellar masses using the the M_*/L_i and $g - r$ color relations and diet Salpeter initial mass function of Bell et al. (2003). The surface densities are deprojected by rescaling the stellar mass surface densities such that the total integrated mass is equal to the global value. This procedure assumes that the stars are distributed in a infinitely thin disk. I again stress that this method is not intended to give the most accurate distribution of stellar mass, but rather to give a rough estimate of where the bulk of the stellar mass is located.

Dark Matter

I use the GIPSY task ROTMAS to fit dark matter distributions to rotation curves. The ROTMOD task calculates the gaseous (HI, Helium, and, where detected, H_2) and stellar contributions to the galaxy rotation. The amplitude of rotation unaccounted for by the stellar and atomic gas components is ascribed to the dark matter:

$$V_{\rm obs}^2 = V_{\rm gas}^2 + V_*^2 + V_{\rm DM}^2 \tag{4.4}$$

I model two different spherically symmetric dark matter density profiles: the pseudo-isothermal model (ISO), and the Navarro-Frenk-White (NFW; Navarro et al. 1997) model. More details and the exact functional form of the velocity for the two models can be found in §A.6.4.

The ISO model is motivated by two observations: the rotation curves of galaxies approach a constant value (they are "flat") at large radii, and they go to zero smoothly at a radius of zero. The ISO model generally does an excellent job of fitting a range of galaxies, from dwarf galaxies to massive spirals. However, it has no theoretical motivation. The NFW profile, on the other hand, is motivated by distributions of collisionless ΛCDM dark matter halos observed in numerical simulations. However, in the literature it is observed that NFW profiles do a very poor job of fitting the rotation curves of both gas-rich dwarf galaxies (e.g. Weldrake et al. 2003; Salucci et al. 2003; Trachternach et al. 2008) and low surface brightness galaxies (LSB; e.g. McGaugh and de Blok 1998; Kuzio de Naray et al. 2008; Kuzio de Naray et al. 2009). For a recent review, see de Blok (2010).

4.3.3 Spin Parameters

The spin parameter λ of the dark matter halo is a dimensionless measure of a halo's angular momentum and is defined as (Peebles 1971):

$$\lambda = \frac{J\,|E|^{1/2}}{GM^{5/2}} \tag{4.5}$$

where J, E, and M are the halo's total angular momentum, energy, and mass. One unfortunate problem for anyone hoping to fit a dark matter halo's spin parameter is that almost any λ can fit fixed NFW halo parameters c and R_{200} or pseudo-isothermal R_C and ρ_0. In simulations, λ has shown to be only weakly correlated to other halo parameters, with quite large spread (Neto et al. 2007; Macciò et al. 2007), and so we cannot simply use our rotation curve derived halo properties to constrain the value of λ. Instead, I use a novel method to estimate the spin parameter by a more direct calculation, finding J, E, and M in turn.

To simplify computation, it is often assumed that the coupling between the dark and baryonic matter is such that the angular momentum per unit mass j of the dark matter and for the baryons j_b are equal (e.g. Mo et al. 1998, Boissier and Prantzos 2000). The same is true for studies of observed galaxy populations (e.g. Hernandez et al. 2007, Cervantes-Sodi and Hernández 2009, Huang et al. 2012a), which we desire to compare our results with. As such, these calculations are really tracing the so-called modified spin parameter $\lambda' = j_b/j \times \lambda$. For the rest of this dissertation, when I refer to the spin parameter, or λ, we are properly talking about the modified spin parameter λ'. I then calculate the total angular momentum of the dark matter halo:

$$J = \frac{M}{M_{\rm HI}} \sum_i M_{{\rm HI},i} V_i r_i \tag{4.6}$$

under the assumption that the gas adequately traces the baryonic angular momentum per unit mass. In most cases, one cannot adequately fit tilted rings out to the edge of emission in neither UGC 9037 nor UGC 12506. However, in spiral galaxies, the rotation will either

completely flattened or is be very flat out to this point, and so I assume that a constant velocity continues out to the edge of the HI emission.

I assume that the halos are virialized, and so can estimate their total energy from their kinetic energy. As discussed later in §5.5, a pseudo-isothermal dark matter model fits both galaxies well. The energy of a pseudo-isothermal dark matter halo can be calculated approximately out to large radii ($r \gg R_C$), where most of the mass and energy reside. Here the pseudo-isothermal model approaches an isothermal halo, which has energy:

$$|E| = |T + U| = T \approx \frac{1}{2} M V_C^2 \tag{4.7}$$

where V_C is the maximum circular velocity of the halo and M is the total mass of the dark matter halo. Using the NFW fit instead of the pseudo-isothermal changes the estimate in the total energy by only a few percent, and should have little effect on our final results.

I estimate our total halo masses using the results of Papastergis et al. (2012). Those authors use abundance matching to relate each observed galaxy's baryonic mass (defined as stellar and HI) to a simulated halo mass: the galaxies with the highest baryonic masses are matched with the most massive halos, and so on. In this way, every halo mass can be associated with an average baryonic mass of the galaxy it hosts.

I also use the above method to calculate spin parameters of dark matter halos for the THINGS galaxies (Walter et al. 2008; de Blok et al. 2008), using their rotation curves and mass models. The THINGS galaxies act as a reference sample of more 'typical' local galaxies than the HIghMass sample. However, note that while THINGS galaxies are *more* 'typical' than the HIghMass galaxies, THINGS is only observing very local ($d \sim 10$ Mpc) galaxies in order to get the best possible sensitivity and resolution, and is not in any way a representative sample of the local universe.

Instead, they will act as another way to verify the effectiveness of the above method to calculate spin parameters via comparison to spin parameters empirically-derived from optical properties (e.g. Hernandez et al. 2007, Huang et al. 2012a) or from simulation (e.g. Shaw et al. 2006). Discussion of spin parameters and evaluation of this method is presented in §5.5.

4.3.4 Stability and Star Formation Thresholds

I use three theoretical measures to investigate where star formation is expected to occur. These criteria are then compared with our Hα images, which accurately trace recent massive ($\gtrsim$ 10 $M_\odot$) star formation.

First is the Toomre Q parameter (Toomre 1964), which indicates the surface density at which an infinitely thin disk is unstable to radially symmetric perturbations, and thus the gas can rapidly collapse. In practice, this threshold is never reached, but below some finite fraction (usually ~ 0.4), star formation is observed to be inefficient. Our Toomre Q plotted curves will thus actually be $0.4 \times \Sigma_{\rm HI}^{\rm Q}$.

The second threshold is put forth by Hunter et al. (1998), who argue that the differential rotation in a galaxy between the gas at two different radii is the dominant stabilizing factor. Generally this criteria is best motivated for dwarf galaxies and low surface brightness galaxies, where the rotation curve is rising across most of the disk.

The third threshold is a model by Schaye (2004), and is designed to identify, based on surface densities and the local UV radiation field, when a cold phase of HI can form. As HI must form a cold phase before collapsing to H_2 and finally stars, Schaye (2004) argues that this criterion should identify regions of a galaxy where star formation can be efficient.

In addition to these theoretical measures, I also consider the gas surface densities at which HI becomes saturated and H_2 is observationally found to dominate over HI. Rarely is HI with surface densities above 10 $M_\odot$ pc^{-2} observed in the local universe. Generally, any gas in excess of 10 $M_\odot$ pc^{-2} is found to be in the form of H_2 rather than HI.

CHAPTER 5

HI CASE STUDIES: UGC 9037 AND UGC 12506

This chapter presents an in-depth examination of two galaxies from the HIghMass sample, UGC 9037 and UGC 12506 using the data reduction and analysis techniques discussed in §4. For both I have completed HI synthesis observations, but neither has been observed in CO and thus their H_2 masses and distributions are unfortunately unknown. Additionally, the two galaxies have quite different histories, spanning the range of our HIghMass galaxy hypotheses. UGC 9037 appears to have recently acquired its gas and is on the cusp of a major star formation event, while UGC 12506 appears to be a galaxy with a high spin parameter λ. This chapter is largely an excerpt from Hallenbeck et al. (2014), which has recently been accepted for publication in the AJ.

The layout of this chapter is as follows: in §5.1, I present the results of the VLA calibration of UGC 9037 and UGC 12506. In §5.2 and §5.3 I present an overview of each galaxy, including its basic optical, star formation, and gas properties. §5.4 presents the gas surface density profiles and stability for both galaxies, while §5.5 presents what I have derived about the dark matter content of each galaxy. §5.6 discusses what I believe to be the evolutionary history of each galaxy, and §5.7 summarizes my findings.

5.1 Calibration Checks

As global spectra and spectra-derived quantities are the primary data products of ALFALFA, I use these to evaluate the quality of the VLA observations, determine whether significant flux was missed, and double-check my data reduction approach. Figure 5.1 shows the global VLA spectra for UGC 9037 and UGC 12506. The spectra were produced by integrating

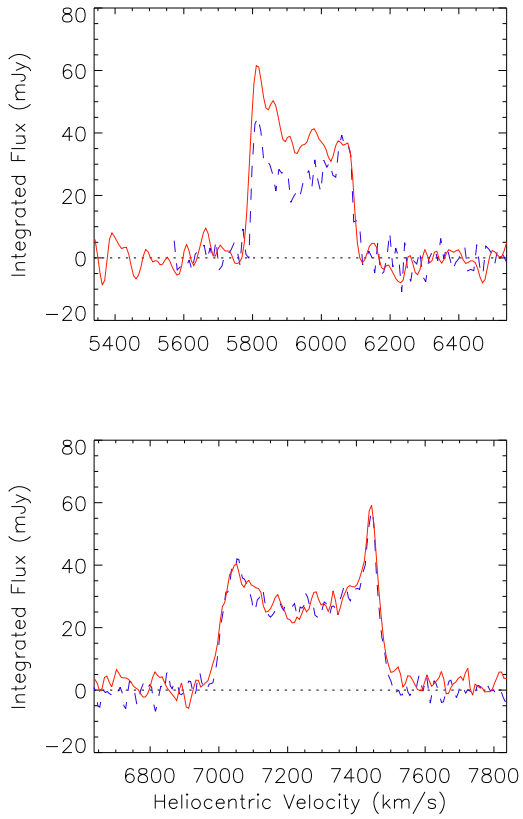

Figure 5.1: HI spectra of UGC 9037 (above) and UGC 12506 (below). Both the ALFALFA spectrum (blue dashed lines) and the VLA spectrum (red solid lines) are plotted. The VLA recovered fluxes agree within 5-10% of the ALFALFA values, but the VLA spectrum for UGC 9037 has significantly more flux in the blueshifted peak than what is observed in ALFALFA.

the data cubes where the flux map indicates that significant ($> 3\sigma$) emission exists. The single-dish ALFALFA spectra from the HI archive[1] are overplotted. Qualitatively, The VLA spectrum of UGC 12506 closely matches the ALFALFA spectrum. The one for UGC 9037 is less well-matched: the there is significantly more emission in the VLA spectrum compared to the ALFALFA spectrum, particularly in the blueshifted horn of the profile. I do not believe that this asymmetry is real and thus originates either from the higher noise characteristics of the VLA spectrum, or from the uncertainties in the overall flux scale in the VLA observations.

[1]http://arecibo.tc.cornell.edu/hiarchive/alfalfa/default.php

Galaxy	Instrument	Flux	W50	V_{sys}
		Jy km s^{-1}	kms s^{-1}	kms s^{-1}
		(1)	(2)	(3)
UGC 9037	VLA	12.68 ± 0.34	301.8 ± 2.6	5943.0 ± 1.8
	ALFALFA	11.51 ± 0.1	294 ± 2	5939 ± 1
	Difference (σ)	3.3	2.4	1.9
UGC 12506	VLA	14.45 ± 0.34	461.6 ± 3.0	7235.8 ± 1.5
	ALFALFA	14.82 ± 0.11	457 ± 5	7237 ± 2.5
	Difference (σ)	1.0	0.8	0.41

Table 5.1: Comparison of derived quantities from the VLA and ALFALFA spectrum of each galaxy (see Figure 5.1). Derivation of ALFALFA measurements is discussed in Haynes et al. (2011); VLA measurements are derived from spectra in the same way, but with W50 measurements corrected for instrumental broadening as discussed Springob et al. (2005); Column 1: The total integrated flux density of the galaxy; Column 2: The full velocity width at half of the peak emission; Column 3: The systemic heliocentric velocity of the galaxy, using the optical convention. All reported errors are 1-σ uncertainties using standard propagation of uncertainty.

Table 5.1 contains the fitted total integrated fluxes, velocity widths, and systemic velocities of the galaxies from the VLA and ALFALFA observations. A qualitative comparison shows that there are no detectable differences between the spectra for UGC 12506 from ALFALFA and the VLA ($\lesssim 1\sigma$). For UGC 9037, unsurprisingly, the two spectra match more poorly, with the systemic velocity and W50 values being only in reasonable agreement ($\lesssim 2\sigma$). The excess emission observed in UGC 9037 is such that there is overall 9% more integrated flux in the VLA spectrum of this galaxy compared to the ALFALFA spectrum, a 3σ difference. However, as calibration uncertainties for interferometric observations are typically 5%-10%, this is not a major concern.

5.2 Overview of UGC 9037

Figure 5.2 shows an optical image from the SDSS of UGC9037. It is a fairly inclined ($i \sim 60°$) spiral galaxy with a weak bar. Its spiral arms appear quite blue, indicating a healthy star formation rate (which is confirmed by Hα observations, discussed below), while its center

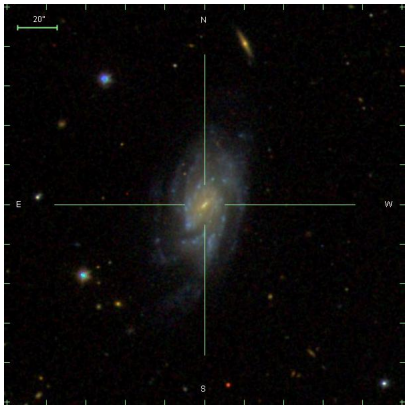

Figure 5.2: An optical false-color SDSS (g, r, and i bands) image of UGC 9037.

is red, indicating that the light there is dominated by older, less massive stars. While this could be an indication that the star formation in the center of the galaxy is weak, our Hα observations (below) indicate that star formation in the galaxy's center is healthy, and in fact is highly peaked (Huang et al. 2014, in review). Instead, it is likely that the red color is a result of a large old stellar population dominating the optical emission, rather than younger, bluer stars.

Figure 5.3 presents images of UGC 9037 in several different bands. At the Hubble flow distance of ~ 89 Mpc (assuming $H_0 = 70$km s^{-1} Mpc^{-1}), each arcsecond corresponds to 0.42 kpc, and so with a clean beam of $\sim 6''$, the VLA observations have a resolution of roughly 2.5 kpc. The top left panel is a SDSS optical image, with contours from our integrated flux map overlaid. The contours begin at 2σ significance ($N_{\rm HI} = 10^{21}$ cm^{-2}), and increase by 2σ at each additional contour. On the scale of the beam, significant substructure is clearly visible. The peak of central HI emission is slightly displaced from the optical center of the galaxy, and the spiral arm features to the south are clearly visible in HI. A weak bar is optically visible, but I do not have the resolution in HI to determine any relationship between the stellar population and HI there.

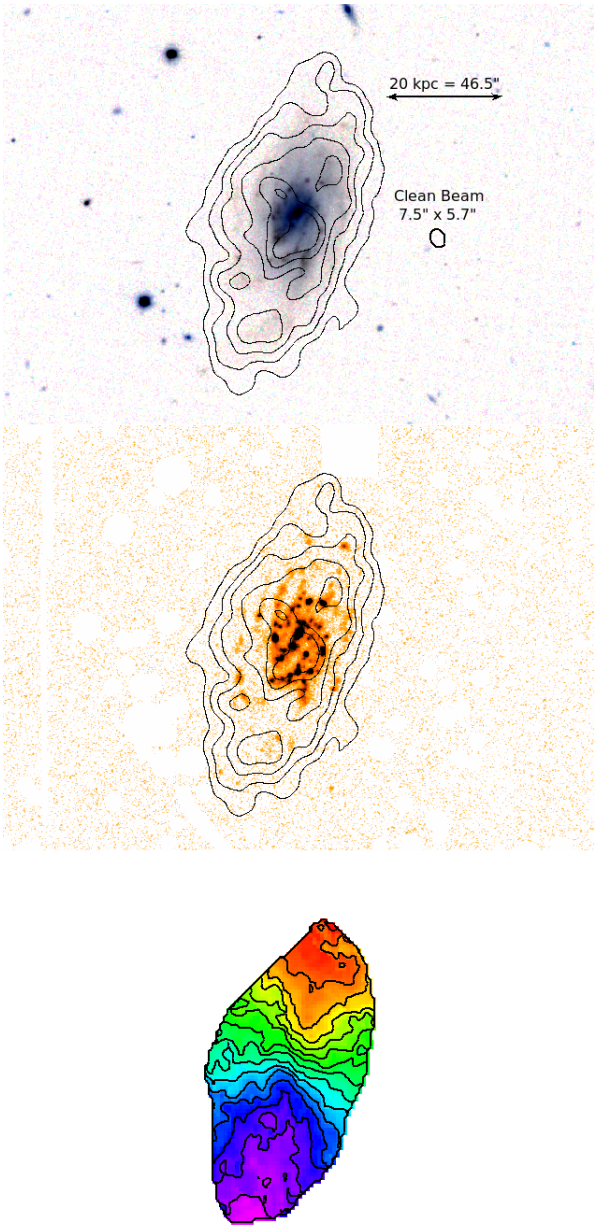

Figure 5.3: Images of UGC 9037, which has an inclination of $\sim 60°$. (top) HI intensity map. Contours begin at 4σ ($N_{\rm HI} = 10^{21}$ cm^{-2}), and increase by 2σ at each additional contour. The contours are overlaid on a false-color SDSS image (g, r, and i bands) with each color channel adjusted for maximum contrast. (middle) Hα image of UGC 9037 from Huang et al. (2014, in review), with HI density contours overlaid. HI emission is tightly peaked near the center of the galaxy and does not extend significantly beyond the stellar disk; the Hα shows significant star formation in the spiral arms which smoothly decreases with radius. (bottom) Moment 1 velocity field. Isovelocity contours are stepped at 20 km s^{-1}.

One interesting feature is that even though UGC 9037 is gas dominated (GF$>$ 1), its HI does not appear to be more extended beyond its optical radius compared to less gas-rich objects of similar stellar mass. The 'Bluedisks' sample examined by Wang et al. (2013) includes galaxies of similar stellar mass but GF $\sim$ 0.3. For that sample, typical ratios of HI radius ($R_{\rm HI}$; where the deprojected $\Sigma_{\rm HI} = 1$ M$_\odot$ pc^{-2}) to optical radius (R_{25}; where the B-band surface brightness reaches 25 mag $''^{-2}$) are $0.1 < \log(R_{\rm HI}/R_{25}) < 0.4$ at the same stellar mass. UGC 9037 has a value in the center of that range, $\log(R_{\rm HI}/R_{25}) = 0.26$.

If we consider only the radius of the HI itself, we also find that UGC 9037 is not extended compared to other galaxies of similar HI mass. For a galaxy with the HI mass of UGC 9037, Broeils and Rhee (1997) predict an HI radius of 44 ± 4 kpc, in good agreement with the observed 42.1 ± 0.7 kpc. From the optical and HI radii alone, it would appear that UGC 9037 is a 'normal' spiral galaxy which has simply been scaled up to a high HI mass and gas fraction.

The middle panel of Figure 5.3 is an Hα image of UGC 9037 with the same HI contours overlaid. Star formation is confined to the spiral arms and bar and decreases smoothly out to the edge of detectable emission at $\sim$25 kpc.

The bottom panel is the moment 1 velocity field, with contours spaced by 20 km s^{-1}. The field shows smooth, well-defined velocities across the extent of HI emission, but some deviations from perfect rotational motion can be seen: there is a twist in the isovelocity contours near the galaxy center along the major axis.

Figure 5.4 shows a position-velocity map, made by taking a slice through the data cube along the average position angle of the galaxy (11° west of north), 20″ wide, through the center of the cube. The velocity structure of UGC 9037 is very clean: at every position along the galaxy, there is a single, narrow range over which HI emission is present. The only

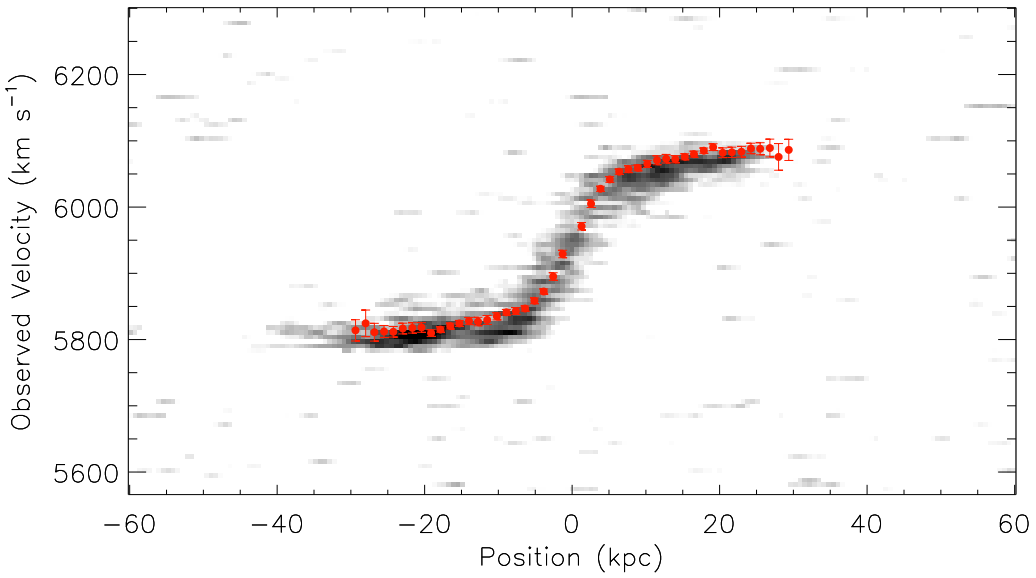

Figure 5.4: Position-Velocity (PV) diagram of UGC 9037, depicting a slice taken through the center of the data cube at the average position angle of the galaxy (-11°). Velocities are observed velocities on the sky, not corrected for inclination. Negative positions are south of the galaxy center, positive positions are to the north. Overplotted points are the fitted rotation curve (see Figure 5.5), projected onto the sky. The PV diagram is consistend with a rapidly rising rotation curve which quickly reaches the maximum rotation velocity; some evidence of decline is seen on the approaching side.

asymmetry in the galaxy is the mismatch of the radial extent of the approaching and receding sides of the galaxy also apparent in Figure 5.3. While the rotation of the receding (north) side of the galaxy can be traced only to 25 kpc, the approaching (south) side is more extended, with emission still easily visible to $\gtrsim$ 40 kpc. The derived rotation curve is over-plotted on the diagram, projected onto the sky, and matches very well, but the asymmetric nature of the emission is not captured in the rotation curve, which is assumed to be symmetric.

The decomposition of UGC 9037 into tilted rings appears in Figure 5.5. All four panels are plotted as a function of deprojected radius to the fitted rotational center. The black filled points and solid lines are for the best-fit model. In the top left panel is the rotational velocity. The rotation curve of UGC 9037 rises quickly, and by 20 kpc has reached its

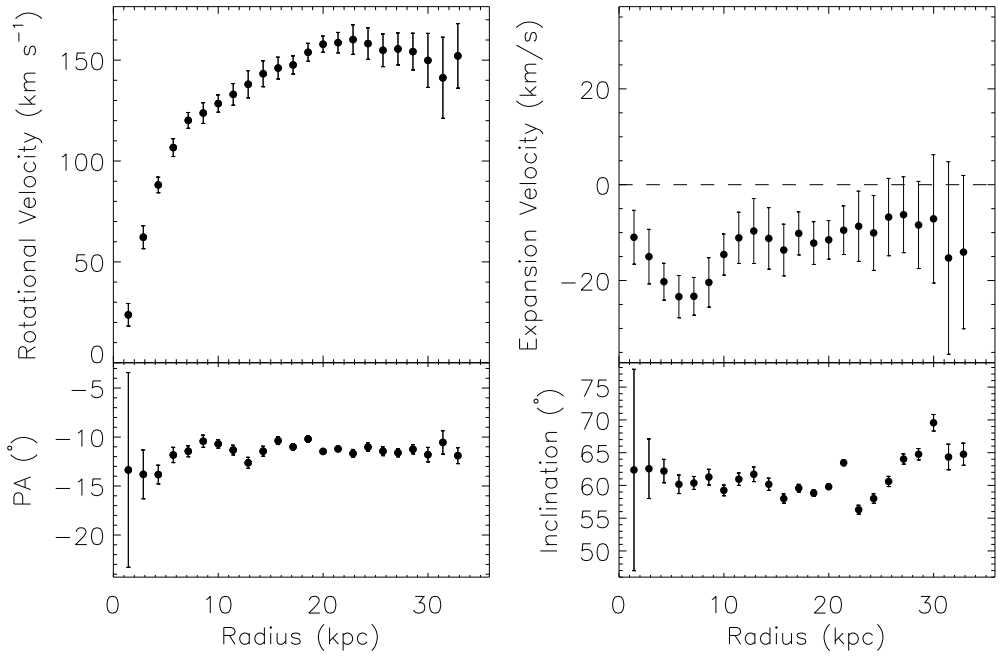

Figure 5.5: Decomposition of UGC 9037 into tilted rings fit to the velocity field. Subgraphs are (top left) rotational velocity, corrected for inclination; (top right) expansion, or radial velocity of the rings; (lower left) position angle of rings, measured east from north (all fitted angles are negative, and thus the semimajor axis is slightly west of north); (lower right) inclination of rings; 0° is face on. The rotational velocity rises quickly to a maximum rotational velocity of ∼160 km s^{-1} after 20 kpc, qualitatively matching the PV diagram (see Figure 5.4). Across the disk, there are clear indications of noncircular gas motions: the gaseous disk is rapidly rotating, but also showing non-circular velocities. The disk geometry is quite flat, with the position angle and inclination varying by only 5-10° across the entire galaxy.

maximum of 160 km s^{-1}, then shows signs of decline. The top right panel presents the expansion velocities of the rings. These velocities are negative in the ROTCUR model, but without knowing which side of the disk is closest, it is not possible to determine whether these velocities represent inflow or outflow. There are non-circular velocities at all radii, although only within 20 kpc does each individual point become significant. The average non-circular velocity is -14.4 ± 1.2 km s^{-1}, approximately 9% of the maximum rotation speed of 160.2 ± 7.3 km s^{-1}.

Are these non-circular velocities real and significant? One problem with fitting tilted

ring model rotation curves is that disk geometry is degenerate with non-circular velocities: one can, by varying the position angle and inclination of the disk, allow for any choice of 'expansion velocity' (e.g. Schoenmakers et al. 1997; Sellwood and Sánchez 2010). However, it is well known that the inner regions of real galaxy disks are very flat, and our best-fitting model is also quite flat. The position angle (measured east of north; lower left) and inclination (lower right) only vary by a few degrees over the entire disk, although outside of 20 kpc, the disk shows some slight bending ($\Delta i \sim 10^\circ$). Forcing the non-circular velocities to zero requires the inner disk to twist quite strongly (Δ PA $\sim 15^\circ$), strongly counter-indicating such a model. The inner 10 kpc of our model disk does appear to twist slightly (Δ PA $\sim 5^\circ$), although such changes are within our uncertainties. This small twisting could be an indication of the fit following the bar and spiral arms apparent in the optical image and HI intensity map. Such a twisting is observed in resolved studies of nearby galaxies (e.g., Chemin et al. 2009 and Corbelli et al. 2010). However, unlike those authors' findings, fixing the position angle in the inner disk does not remove the effect.

Second, note that while the tilted ring model implemented by ROTCUR can probe some non-circular motions, it is primarily designed to model flat disks dominated by rotational motions with possible warping at large radii; the only non-circular motions it can account for are axisymmetric radial flows. To supplement the ROTCUR results, I use the DiskFit package (Spekkens and Sellwood 2007; Sellwood and Sánchez 2010; Kuzio de Naray et al. 2012), which fits more realistic flat disk models to the observed data. I fit three models using DiskFit: a pure rotational model, a model which allows for radial flows, and one which models bisymmetric (bar-like) flows. The flat disk geometry is allowed to vary in the models, and in all cases I find values that are consistent with the average values obtained by ROTCUR. Figure 5.6 presents the resulting model velocity fields (top) and residuals compared to the moment 1 map (bottom), for the pure rotational (left), radial flow (middle) and bisymmetric flow

(right) models. The model velocity fields have isovelocity contours every 20 km s^{-1}, and the color bar for the residuals spans -10 km s^{-1} to 10 km s^{-1}. As with ROTCUR, a pure rotational model fits the inner disk poorly: the residuals show opposite systematic trends in the east and west halves of the inner disk. By eye, the radial and bisymmetric flow models appear to have nearly identical residuals, and both reproduce the inner velocity field twist (Figure 5.3, bottom panel). Both non-circular flow models present plausible representations of the data: it is not possible to distinguish between the two using the quality of the fit (Spekkens and Sellwood 2007). However, the presence of a weak bar in UGC 9037 (Figure 5.3, top panel) suggests that bar-like flows are the most likely explanation for the observed non-circular motions, although streaming motions toward the galaxy center may also be consistent with the picture that UGC 9037 is on the verge of undergoing intense star formation. All three models show some systematic trends in their residuals at large radii; this may be related to the slight warping seen at large radii in the ROTCUR rotation curve, which has not been taken account in DiskFit.

5.3 UGC 12506: Images and Rotation Curve

Figure 5.7 shows an optical image from the SDSS of UGC12506. It is a spiral galaxy, but so highly inclined ($i \sim 86°$) that more specific classification is not possible from this image alone. Like UGC 9037, we observe a large, blue disk with a red center. Here, however, it is not clear that the redness is due to a large old stellar population rather than extinction due to its extreme inclination. The galaxy is asymmetric optically: the visible emission extends significantly further to the west (right) than to the east (left) from the red center. Directly south of the galaxy is what appears to be a companion galaxy but is actually more likely a higher-redshift background galaxy. I believe this because while the "companion" appears

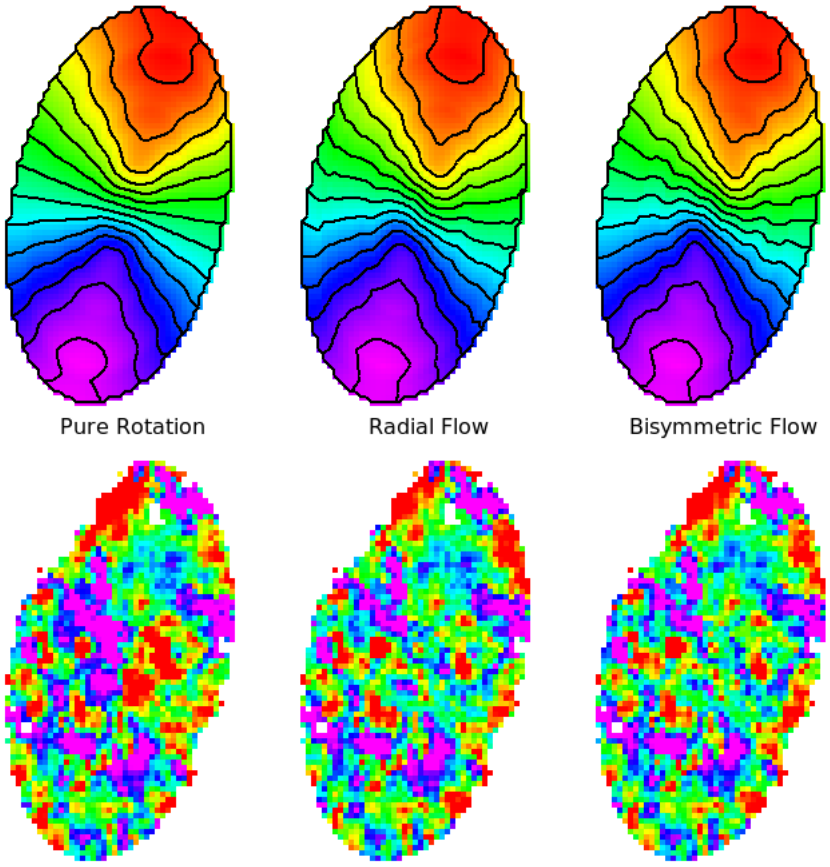

Figure 5.6: (top) Model velocity fields of UGC 9037 created with DiskFit, with solid lines every 20 km s^{-1}; (bottom) residuals with respect to the observed velocity field (see Figure 5.3, bottom panel). The residual color scale ranges from -10 km s^{-1}(purple) to $+10$ km s^{-1}(red). (left) Model with pure rotational velocities, (middle) model allowing for symmetric radial flows, and (right) model allowing for bisymmetric (bar-like) flows. The residuals of the pure rotation model are correlated, and have opposite signs in the east and west halves of the inner disk, showing this model to be a poor fit to the data. The residuals for the radial and bisymmetric flow models are of nearly equal quality.

quite bright and blue in the optical image, I detect neither Hα nor HI coincident with the galaxy at the redshifts of our observations.

In the same format as Figure 5.3, Figure 5.8 presents images of UGC 12506. At the Hubble flow distance of 98 Mpc (assuming $H_0 = 70$km s^{-1} Mpc^{-1}), each arcsecond corresponds to 0.48 kpc, and so with a clean beam of $\sim 6''$, the VLA observations have a resolution of

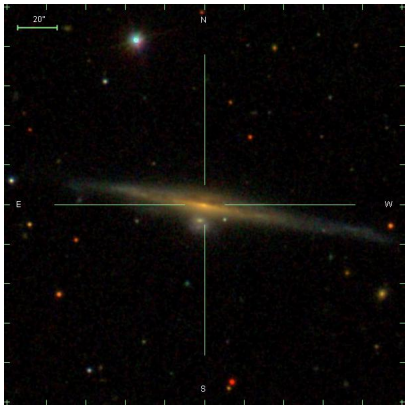

Figure 5.7: An optical false-color SDSS (g, r, and i bands) image of UGC 12506.

roughly 2.9 kpc. The top panel shows HI contours overlaid on a SDSS optical image of UGC 12506. The contours begin at 4σ significance ($N_{\rm HI} = 8.0 \times 10^{20}$ cm^{-2}), and increase by 2σ at each additional contour. UGC 12506 is very large galaxy. Its optical radius is 40 kpc, and the HI can be traced beyond 60 kpc. Like UGC 9037, it has a typical, but lower, $\log(R_{\rm HI}/R_{25}) = 0.16$. Similarly, the predicted HI radius for a galaxy of its HI mass (from Equation 4.2) is 56 ± 4 kpc, in agreement with the observed 58 ± 2 kpc. From the optical and HI radii, the galaxy appears fairly typical for its stellar and HI masses.

In the optical image there are two interlopers, neither of which is connected with UGC 12506. To the east, there is a star nearly coincident with a small overdensity of HI, and to the south, intersecting with UGC 12506 is a galaxy at higher redshift.

The middle panel of Figure 5.8 shows our Hα image of UGC 12506. UGC 12506 shows star formation smoothly spread throughout the disk. The eastern overdensity of HI shows no significant star formation. The bottom panel of Figure 5.8 is the velocity field. Isovelocity contours are spaced every 20 km s^{-1}. The galaxy shows ordered rotation out to the edge of where emission is detectable. The velocity field of UGC 12506 is more complex compared to the smooth UGC 9037. This is an effect of the high inclination of the disk; I do not believe

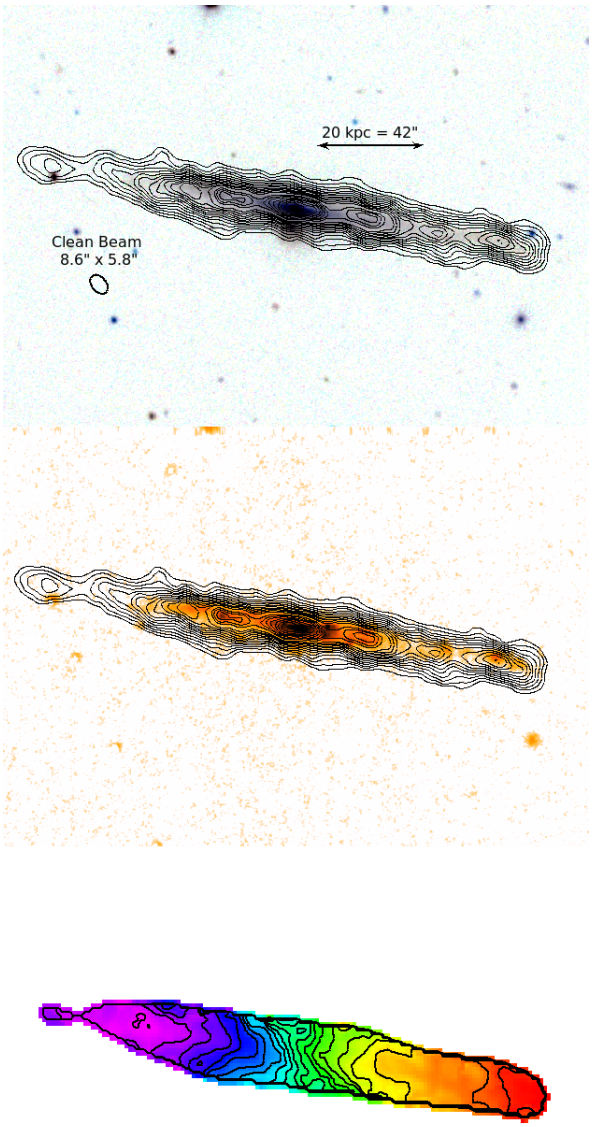

Figure 5.8: Images of UGC 12506, which has an inclination of $\sim 86°$. Panel sequence is analogous to that in Figure 5.3; the 4σ here is $N_{\rm HI} = 8.4 \times 10^{20}$ cm^{-2}. Here the HI is extended beyond the stellar disk ($\log R_{\rm HI}/R_{25} = 0.26$), a value typical for galaxies of similar stellar mass and lower gas fraction (see Wang et al. 2013). The Hα shows that star formation occurs across the entire optical disk.

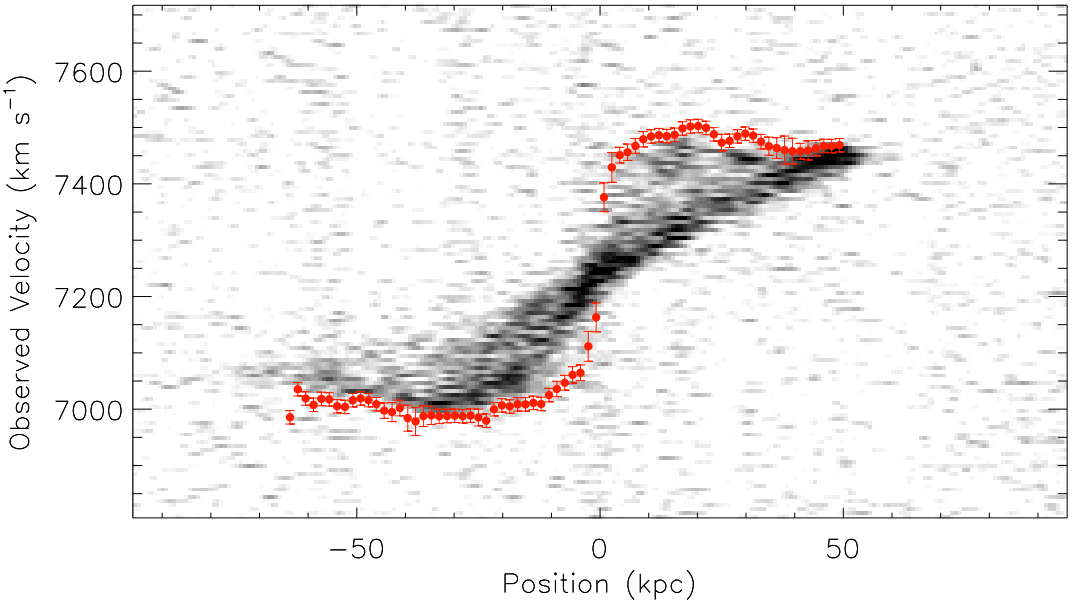

Figure 5.9: Position-Velocity diagram of UGC 12506, depicting a slice taken through the center of the data cube at the position angle of the entire galaxy (-99.7°). Velocities are observed velocities on the sky, not corrected for inclination. Negative positions are east of the galaxy center, positive positions are to the west. Overplotted points are the fitted rotation curve, allowing for the significant asymmetry in the approaching and receding arms, as fit to the PV diagram. UGC 12506's PV diagram shows much more complex structure as emission is not confined to a narrow range of velocities at each position. This is due to the high inclination of UGC 12506 ($i \sim 86°$): at every off-center position a range of projected velocities are compatible with a single rotational velocity.

that the closed contours indicate a real decrease in the rotation curve. The inclination of UGC 12506 is high ($i = 86°$), causing the velocity field to be a poor indicator of the rotational velocity of the galaxy—a position-velocity diagram is required.

Figure 5.9 shows the position-velocity diagram for UGC 12506, produced in the same fashion as Figure 5.3, except that the major axis is along 99.7° west of north. The galaxy's high ($\gtrsim 80°$) inclination combined with the finite HI beam size means that there is a broad range of velocities present at every position along the major axis, rather than a single velocity. The envelope fitting method (see §A.5.2 for details) smoothly traces the maximum observed velocities. There is some asymmetry in the approaching (eastern) and receding (western)

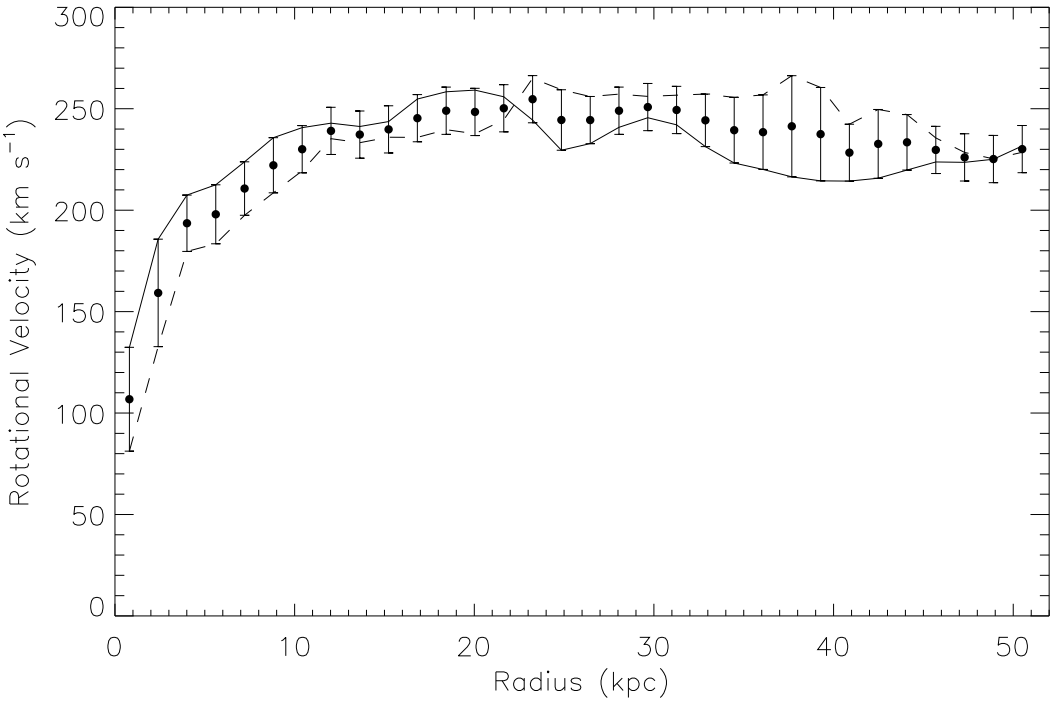

Figure 5.10: Rotation curve of UGC 12506, the average of the approaching and receding sides, as observed in Figure 5.9, and corrected for inclination. The lines represent the rotation curve on the receding (solid) and approaching (dashed) sides of the galaxy, while the points are the average of the two. The entire galaxy is assumed to have a single inclination ($i = 86.4°$) and positional angle ($PA = 99.7°$ west of north). Like UGC 9037, the rotation curve rises rapidly, but unlike UGC 9037 it shows signs of decline at large radii.

sides of the galaxy in both the shape and length of the arms. The receding side is detectable only to $\sim$ 50 kpc from the galaxy center, while the approaching side is detectable to $\sim$ 70 kpc.

UGC 12506's rotation curve, calculated from the PV diagram, is presented in Figure 5.10. The two lines show the receding (solid) and approaching (dashed) arms of the galaxy. The rotation curve rises quickly and reaches a maximum velocity of $\sim$ 250km s^{-1}.

5.4 Gas Stability and Star Formation

Figure 5.11 shows the deprojected HI surface densities (thick black lines) of UGC 9037 (top) and UGC 12506 (bottom) as a function of radius from the center of the galaxy. Also plotted are the thresholds for axisymmetric gravitational instability (Σ_Q; dotted red lines), shear instability (Σ_A; dashed green lines), for a cold phase to form ($\Sigma_{\rm S04}$; dash-dotted purple lines), and where HI is observed to saturate (~ 10 M$_\odot$ pc^{-2}; cyan dashed triple-dotted line).

The central HI density is quite high in UGC 9037, reaching almost 14 M$_\odot$ pc^{-2}, larger than the 10 M$_\odot$ pc^{-2} where HI is observed to saturate. In the THINGS sample, high surface densities are only observed in NGC 3077 (whose gas is highly disturbed and asymmetric) and NGC 4214 (which is an irregular galaxy). Compared to UGC 9037, both have over an order of magnitude less mass in stars and HI ($\rm HI_{HI} \sim M_* \sim 9$). In addition, over the entire disk, the HI density exceeds our Σ_Q criterion, indicating that the gas is marginally unstable. In this interpretation, the non-circular motions detected in the velocity field may represent inflowing gas to fuel the imminent star formation. A detailed investigation of higher-resolution kinematics, such as those afforded by CO interferometry, as well as a determination of the near side of UGC 9037's disk may help distinguish radial inflows from other interpretations of the observed non-circular motions.

Despite having a slightly higher overall HI mass compared to UGC 9037, UGC 12506 has a low density (typically $1-5$ M$_\odot$ pc^{-2}) HI disk out to 60 kpc. Only in the very center of the galaxy (< 5 kpc) do I expect H_2 to be an important component of the interstellar medium. UGC 12506 lies just at the $\Sigma_{\rm HI} = \Sigma_Q$ line except in the inner $\sim$15 kpc, where $\Sigma_{\rm HI}$ becomes strictly less than Σ_Q. However, the Hα imaging does not mirror this: we see healthy star formation throughout the disk, including near the galaxy's center. If H_2 is a significant near the center of the galaxy, it may make up this gap.

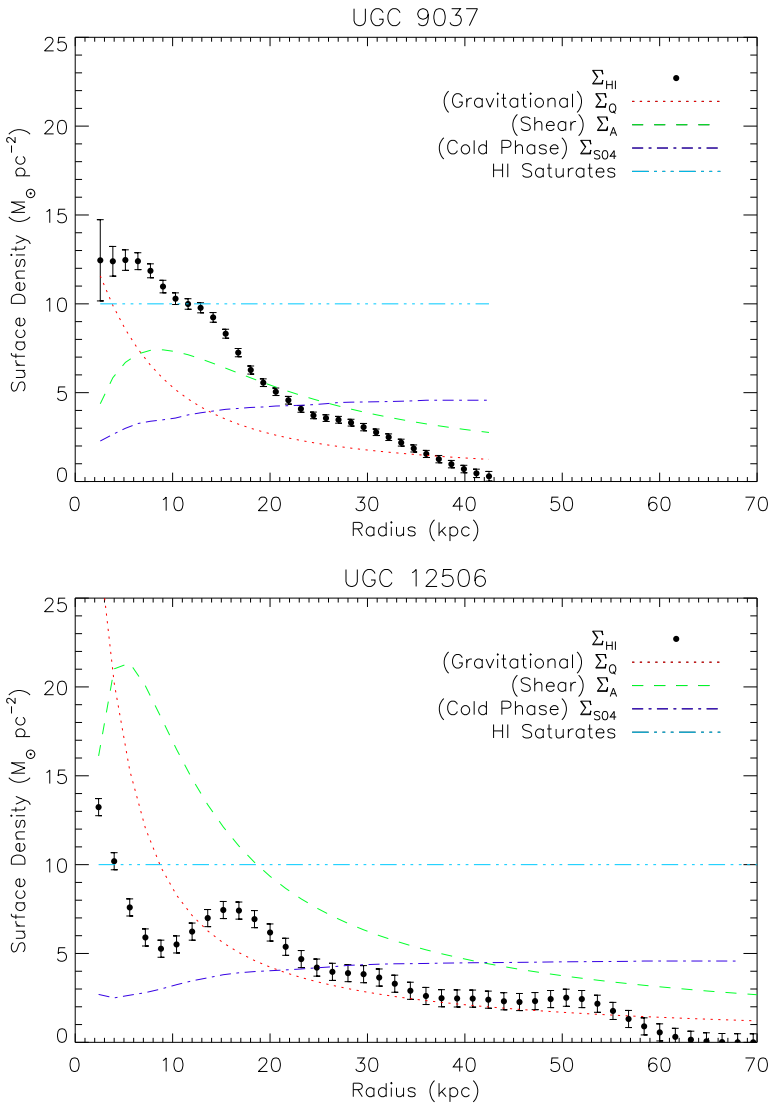

Figure 5.11: HI surface densities as a function of radius for both UGC 9037 (top panel) and UGC 12506 (bottom), on identical axes (thick black lines). Also plotted are critical densities for: ring-like gravitational collapse (Σ_Q; red dotted lines), collapse inhibited by shear (Σ_A; green dashed lines), for a cold phase to form ($\Sigma_{\rm S04}$; purple dashed-dotted lines), and where HI is seen to saturate (HI saturates; cyan dashed triple-dotted lines). The HI in UGC 9037 is more centrally peaked, with surface densities > 10 M$_\odot$ pc^{-2}, while the HI in UGC 12506 is more extended, out to 60 kpc, with typical surface densities of $1 - 4$ M$_\odot$.

Galaxy	NFW Halo			Iso Halo			Spin Parameter
	c	R_{200} kpc	$\chi^2_{\rm NFW}$	ρ_C $10^{-3}{\rm M}_\odot/{\rm pc}^3$	R_C kpc	$\chi^2_{\rm Iso}$	λ
	(1)	(2)	(3)	(4)	(5)	(6)	(7)
UGC 9037	2.67 ± 0.50	121 ± 12	1.29	18.0 ± 2.0	5.16 ± 0.40	0.65	0.07
UGC 12506	14.87 ± 0.60	123.0 ± 1.5	0.21	1150 ± 360	0.91 ± 0.15	0.54	0.15

Table 5.2: Results of fitting both Navarro-Frenk-White (NFW) and pseudo-isothermal (Iso) dark matter halo profiles to the two galaxies. Columns 1-2: Concentration index and characteristic length scale of halo (see Equation A.25); Column 3: χ^2 per degree of freedom of fit to NFW profile; Columns 4-5: central density and core scale length of halo (see Equation A.23); Column 6: χ^2 per degree of freedom of fit to Iso profile; Column 7: Modified spin parameter of the Iso dark matter halo, as discussed in §4.3.3.

Both galaxies have a roughly exponential HI profile, unusual for galaxies in the local universe. Generally, a flat or decreasing density in the inner disk with $\Sigma_{\rm HI}$ stagnating near 10 $M_\odot$ pc^{-2} is observed (e.g. Walter et al. 2008; Leroy et al. 2008). UGC 9037 only begins to flatten in the very inner disk, at approximately 13 $M_\odot$ pc^{-2} of HI. As UGC 12506 barely reaches 10 $M_\odot$ pc^{-2} of HI near its center, and thus could not show a flat profile over any significant range of radii given the resolution of our observations, it is difficult to draw conclusions about its profile. However, the combination of its very high HI mass and low surface densities are very unusual.

For neither galaxy does the shear criterion appear to be a significant predictor of star formation, as for both galaxies $\Sigma_{\rm HI} < \Sigma_A$ across essentially the entire disk despite clear evidence of star formation across the entire disk. Similarly, for both galaxies, the predictions of the model of Schaye (2004) suggest that a cold phase can form only in the inner $10 - 20$ kpc of each galaxy.

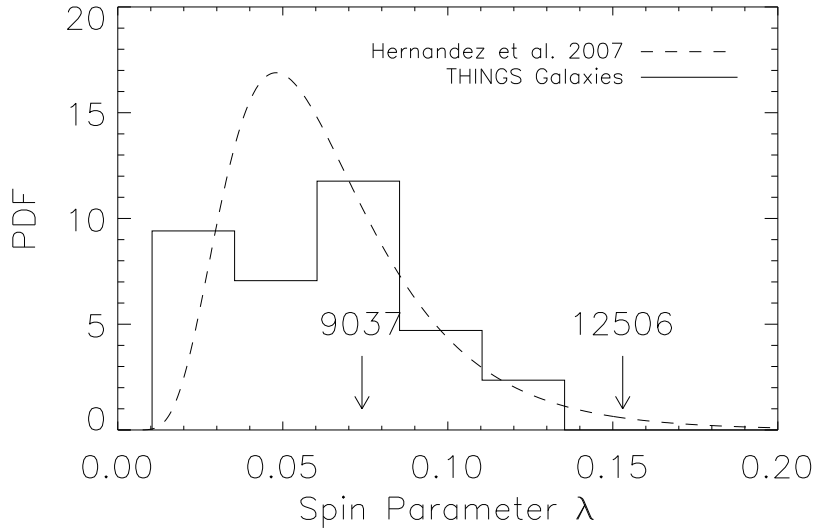

Figure 5.12: Distribution of observed spin parameters of galaxies. The solid histogram shows spin parameters of the THINGS galaxies. The dashed line is the best-fit lognormal distribution of SDSS galaxies by Hernandez et al. (2007). The two very roughly occupy the same range of values. They may be from the same distribution, but with the small number of galaxies in the THINGS sample we cannot tell. Arrows show the calculated spin parameters of UGC 9037 (0.07) and UGC 12506 (0.15). Measured against either standard, UGC 9037 has a typical spin parameter, while UGC 12506's is quite high.

5.5 Dark Matter and Spin Parameters

The parameters obtained from fits of both NFW and ISO halos to our galaxies' rotation curves appear in Table 5.2. Both galaxies are well-fit by both halo models ($\chi^2/\mathrm{dof} \lesssim 1$). An F-test statistic indicates that UGC 9037 shows weak evidence of favoring the ISO model ($\chi^2_{\mathrm{ISO}} = 0.65; \chi^2_{\mathrm{NFW}} = 1.29;\ p = 0.07$), but is not conclusive. For UGC 12506, there is a very significant preference for the NFW model ($\chi^2_{\mathrm{ISO}} = 0.54; \chi^2_{\mathrm{NFW}} = 0.21;\ p = 0.004$). As UGC 12506 is a low surface brightness galaxy (Huang et al. 2014, in review), this result is surprising. In general, LSB galaxies exhibit slowly rising rotation curves and cannot be fit by NFW profiles (e.g. Moore 1994, McGaugh and de Blok 1998), while UGC 12506 exhibits neither of these qualities.

As previously discussed, simulations and semi-analytic models suggest a correlation between gas richness and high spin parameter as suggested observationally by Huang et al. (2012a). Figure 5.12 shows a probability density function of spin parameters of THINGS galaxies calculated according to the method in §4.3.3; the histogram is normalized so that the total area is unity. The range of spin parameters ($0.01 < \lambda < 0.10$) that I calculate for the THINGS galaxies matches up with 'typical' values of spin parameters derived from observation and simulation (Shaw et al. 2006; Macciò et al. 2007; Hernandez et al. 2007). Also plotted in the figure as a dashed line is the best-fit lognormal distribution of the sample of Hernandez et al. (2007). The two are similar in a very rough sense. The disagreement may be due to the differences between our method and that of Hernandez et al. (2007) for calculating spin parameters, but given the small number statistics and uncertainties in the calculation of λ, I hesitate to read further into this.

The spin parameters for our two galaxies, UGC 9037 and UGC 12506 are plotted in Figure 5.12 as arrows. UGC 9037 has a spin parameter of $\lambda = 0.07$, while that of UGC 12506 is $\lambda = 0.15$. Whether we compare to the HI-derived or the optically-derived sample, the results are the same: UGC 9037 has a typical value, while UGC 12506 has a very high spin parameter. If we compare to the results obtained by Huang et al. (2014, in review) for the HIghMass sample as a whole, we find that UGC 9037 has a somewhat low spin parameter, while UGC 12506's spin parameter is still quite high.

5.6 Discussion

5.6.1 UGC 9037: On the Verge of a Starburst?

The specific star formation rate of UGC 9037 is SSFR $\equiv$ SFR/M_* = 3.5×10^{-10} yr^{-1}, which is elevated compared to the typical value for an galaxy with the same stellar mass (0.9×10^{-10} yr^{-1}; Huang et al. 2012a; Huang et al. 2014, in review). The HI and Hα both tell the same story in UGC 9037: this is a galaxy which is entering into a phase of significant star formation. The Hα imaging shows very strong star formation is occurring in the central parts of the galaxy, which is an extremely gas-rich spiral. Across the disk the gas is marginally stable and non-circular flows—possibly inflows—of up to 20 km s^{-1} are detected. High gas surface densities have built up, fueling star formation: interior of 10 kpc, densities are > 10 M$_\odot$ pc^{-2}, with the central surface density reaches nearly 14 M$_\odot$ pc^{-2}, significantly above what is typically observed to be the maximum in local star-forming galaxies. All four of our examined star formation thresholds (axisymmetric gravitational instability, shear, formation of a cold phase, and H_2 dominance) point to strong future star formation ability.

But why does UGC 9037 appear to be just now converting this large, dynamically unstable reservoir of gas into stars? The simplest explanation is that the gas is unstable due to its weak bar, but this does not explain why the galaxy has that feature. UGC 9037 is in the outskirts of the NGC 5416 group (poor cluster MKW 12), and so tidal torques from interactions with the group may have created a bar instability in the disk. It is also possible that UGC 9037 has only recently acquired (or is in the process of acquiring) a substantial reservoir of gas, and its dynamics are unable to sustain the gas without an increase in star formation. Both the overall symmetry of the gas distribution and the regularity of the rotation curve indicate that a recent major merger is highly unlikely, but if it is in the process

of accreting from an extended gaseous halo or, as it is in a group, cold gas along a filament, then this is what we would expect to observe. However, given the lack of a strong warp in UGC 9037, any accreted gas would have to have the same angular momentum as the parent galaxy (e.g. Shen and Sellwood 2006). Given how difficult it is to determine inflow rates in nearby galaxies, it is unclear as to whether it will be undergoing major star formation and gas depletion in the near future, or whether it is in a quasi-static state of elevated, but not extremely high star formation (~ 4 M$_\odot$ yr^{-1}).

5.6.2 UGC 12506: High Spin Parameter

In contrast, every property of UGC 12506 points to it as being a massive galaxy with an unusually high spin parameter, which has maintained its gas reservoir in a relatively diffuse configuration, with $\Sigma_{\rm HI}$ typically typically $1 - 4$ M$_\odot$ pc^{-2}. Its gas dynamics are stable, it has a large rotational velocity, and has uniform low-level star formation. While a cold phase of atomic gas can form at modest radii ($\lesssim 20$ kpc), our star formation thresholds do not suggest that the H_2 becomes the dominant phase of the ISM except the very center of the galaxy. We observe modest star formation rates across the disk, and similarly only modest levels of gravitational instability in the disk ($\Sigma_{\rm HI}/\Sigma_Q \sim 0.45$). Our calculation of its spin parameter as $\lambda = 0.15$, very high compared to galaxies in the local universe, confirms these observations.

5.7 Conclusions

The HIghMass sample is a unique sample of several dozen unusually HI-rich high mass galaxies out of galaxies detected in ALFALFA with HI masses $> 10^{10}$ $M_\odot$. In this chapter, I have presented a first look at two of these galaxies using high-resolution VLA observations combined with previous Hα and optical imaging. I have derived structural and dynamical parameters of the gas distribution and derived dark matter halo properties, including their spin parameters. Future analysis will extend these techniques to the rest of the HIghMass sample.

Our primary question is how galaxies can maintain such large gas reservoirs to the present day without processing them into stars. Of the two galaxies, UGC 9037 appears to be undergoing a period of increasing star formation, possibly stimulated by a bar instability in the inner part of the disk. Given the very high (> 10 $M_\odot$ pc^{-2}) surface densities at the center, we expect to see very high quantities of H_2 present there. The non-circular flows detected in the disk may stem from radially inflowing gas to fuel the star formation, although flows along the weak bar in this galaxy may be the more likely explanation. Its current global rate of star formation (~ 4 $M_\odot$ yr^{-1}) may be sustainable by accretion from its gaseous halo, but if it does undergo rapid star formation in the near future, it may quickly transition toward the red sequence.

The other galaxy, UGC 12506 appears to have a large halo spin parameter ($\lambda = 0.15$), leading to lower gas densities and thus star formation rates over the entire disk. UGC 12506's gas is quite stable, but supporting of modest star formation at all radii. I predict its gas to be HI-dominated at essentially all radii, with relatively little H_2. Overall, the most consistent history of UGC 12506 is that its high spin has prohibited it from reaching high rates of star formation, and its baryonic component remains gas-dominated.

CHAPTER 6

COMBINED HI AND H_2 OBSERVATIONS

So far, I have observed the ^{12}CO(1-0) line with 5 galaxies using CARMA. Only three of them have been successfully detected: UGC 6168, UGC 7899, and UGC 8573 (which is also NGC 5230). Each of these three also has reduced HI observations.

This Chapter presents preliminary results for these three galaxies. The final analysis is incomplete, but this chapter presents many of the basic data products, including moment maps and surface densities for both the HI and H_2. We also speculate on the evolutionary history of the galaxies, so that when the final analysis is complete, we may see how predictive the partial analysis is. In §6.1, I present results for UGC 6168, in §6.2 I present results for UGC 7899, and in §6.3 the results for NGC 5230.

6.1 UGC 6168

6.1.1 Spectra

Figure 6.1 (top) shows the VLA HI spectrum of UGC 6168 (red solid lines). The ALFALFA HI spectrum is overplotted (blue dashed lines) in order to compare the flux recovered by the VLA observations. For UGC 6168, the two spectra agree extremely well, and the VLA observations reproduce the asymmetric features of the ALFALFA spectrum. In Table 6.1, I present the HI and CO spectral properties of the detected galaxies. The VLA and ALFALFA derived $W50$ and $v_{\rm sys}$ agree extremely well. The total integrated fluxes are reasonably close, and the flux value differs by 11%, within typical interferometer agreement. Figure 6.1 (bot-

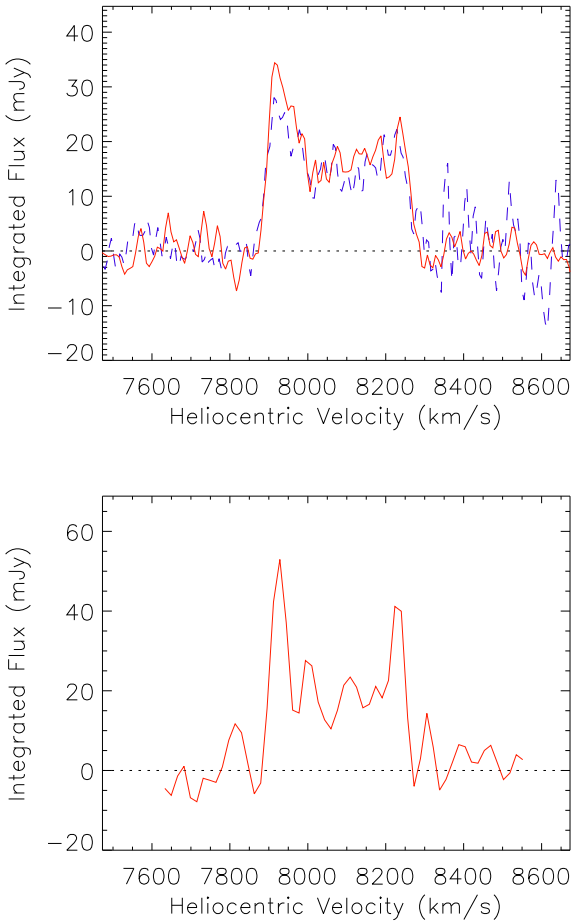

Figure 6.1: HI (top) and CO (bottom) spectra of UGC 6168. For The HI spectrum, both the VLA (red solid lines) and the single-dish ALFALFA (blue dashed lines) are plotted. The VLA and ALFALFA spectra match very nicely, and the CO spectra has similar velocity features.

tom) also presents the CO spectrum of UGC 6168, obtained at CARMA. I find that the CO emission's systemic velocity and W50 are both in good agreement with the ALFALFA values, indicating that there are no obvious kinematic disconnections between the two phases; a better comparison will come when I produce rotation curves for both phases and observe whether they agree in the region where both H_2 and HI are detected.

The H_2 mass is calculated from the CO integrated flux using Equation A.17. The flux of 8.1 Jy km s^{-1} indicates an H_2 mass of $10^{9.0}$ $M_\odot$, or an H_2 gas fraction of $M_{H_2}/M_{HI} = 0.04$.

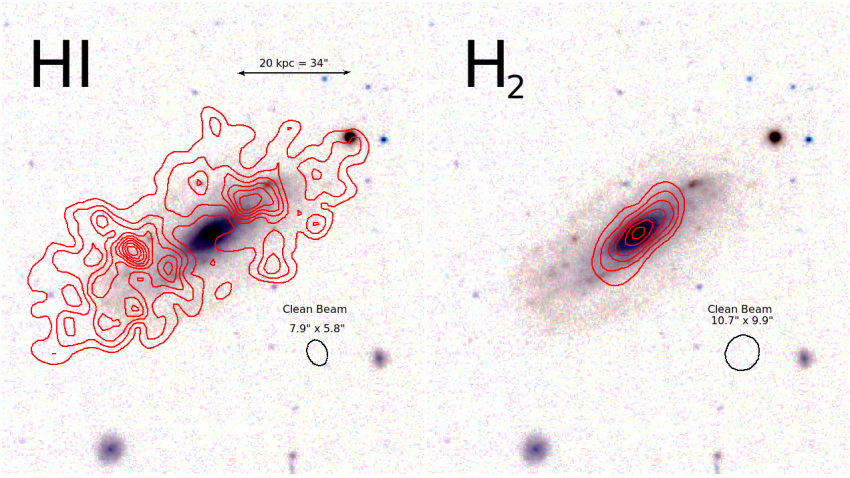

Figure 6.2: HI (left) and CO (right) integrated flux maps of UGC 6168. Because of low signal to noise in both phases, I have chosen to plot the first contour at 2σ, and increase by 2σ at each successive contour. Both images are overlaid on an inverted SDSS image in the g, r, and i bands.

The COLD GASS galaxies have similar stellar masses to the HIghMass sample, but lower gas fractions (Saintonge et al. 2011a). For the COLD GASS sample the average H_2 gas fraction is 0.3, significantly higher than the 0.04 found for UGC 6168. Such a low H_2 gas fraction suggests that the star formation bottleneck exists in the HI to H_2 conversion.

6.1.2 Images and Moment Maps

Figure 6.2 presents the integrated flux maps of UGC6168, both from the VLA HI observations (left) and the CARMA CO observations (right) overlaid on SDSS images. The optical images show that UGC 6168 is a spiral galaxy with moderate inclination. Visually, the HI and CO are not particularly remarkable: they meet the expectation for a massive galaxies with a healthy star formation rate. That is, the HI is extended beyond the optical radius of the galaxy and is in the shape of a ring, with the galaxy's center depleted of HI. Inside the ring, we observe a significant mass of H_2: the hydrogen is not gone from the center of the galaxy, but is in a cold, dense form that is conducive to star formation in the near future.

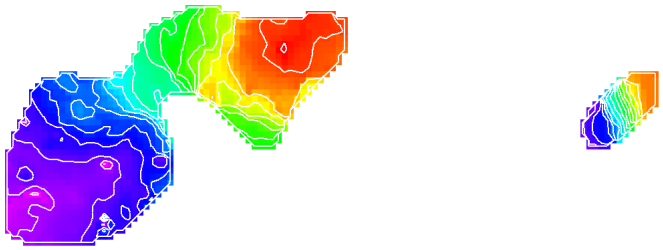

Figure 6.3: HI (left) and CO (right) velocity fields of UGC 6168. The isovelocity contours are spaced every 20 km s^{-1}.

Figure 6.3 presents HI (left) and CO (right) velocity fields for UGC 6168. The HI moment map looks mostly smooth, although there are a few isolated pixels with unusual velocities—indicative of poor masking rather than any real kinematic anomalies. It is difficult to judge the presence of any non-circular velocities from the velocity field alone, but the strong "S" shape in the contours along the southern half of the galaxy suggest some non-circularities. For the CO, there are too few beams across the CO emission in order to make any definite statements. Any rotation curve derived from the CO alone will have only one or two data points, but it is possible to combine the HI and CO into a unified rotation curve using DiskFit.

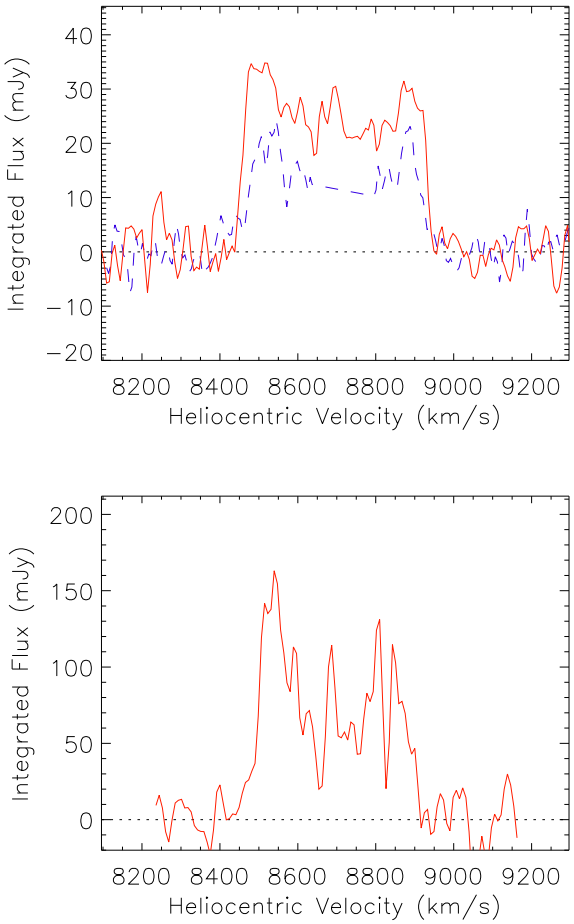

Figure 6.4: HI (top) and CO (bottom) spectra of UGC 7899. For The HI spectrum, both the VLA (red solid lines) and the single-dish ALFALFA (blue dashed lines) are plotted. The VLA spectrum contains nearly twice the flux of the ALFALFA spectrum.

6.2 UGC 7899

6.2.1 Spectra

Figure 6.4 presents the HI (top) and CO (bottom) spectra of UGC 7899. The ALFALFA spectrum is plotted along with the VLA spectrum, as for Figure 6.1. There is a clear discrepancy between the two HI spectra, as the VLA spectrum has roughly twice the flux

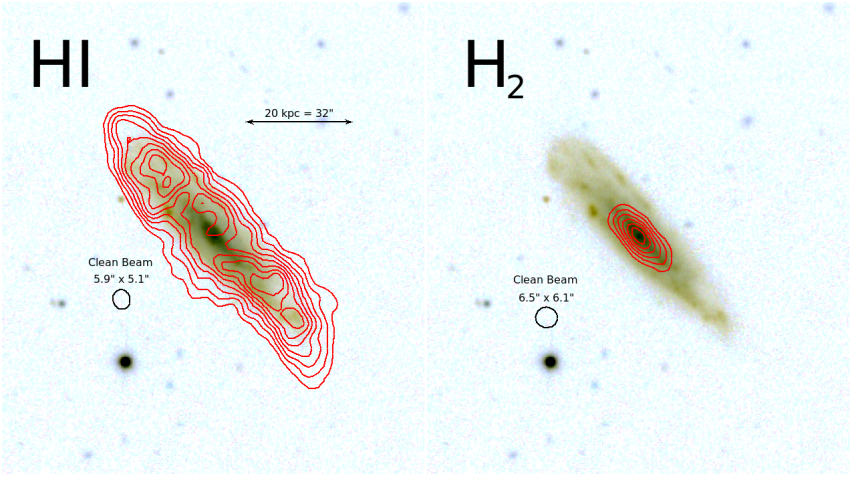

Figure 6.5: HI (left) and CO (right) integrated flux maps of UGC 7899. Both contours use our usual 4σ first contour plus 2σ at each successive contour scheme. Both images are overlaid on an inverted SDSS image in the g, r, and i bands.

of the ALFALFA spectrum. This may be due to poor calibration, or due to the way that the clean task projected the total flux in the image. Feathering the ALFALFA flux with the VLA flux may be a solution. In any case, more investigation is clearly required.

The difference in widths between the VLA and ALFALFA profiles is quite large ($\sim$ 40 km s^{-1}), but due to the large uncertainty in the ALFALFA profile, they agree reasonably. The $W50$ agreement between the CARMA and ALFALFA spectra are similar, but there is likewise a $\sim$ 40 km s^{-1} difference between the two. As CO tends to be centrally located, it is unsurprising that it would have a lower maximum rotational velocity (leading to a lower W50). We cannot detect any differences between the three systemic velocities at any reasonable significance level. The integrated CO flux is 36.6 Jy km s^{-1}, indicating an H_2 mass of $10^{9.7}$ $M_\odot$. The corresponding H_2 gas fraction is 0.2, slightly lower than observed in the COLD GASS sample.

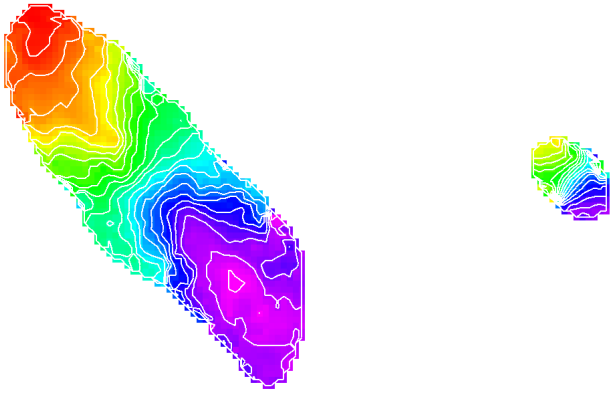

Figure 6.6: HI (left) and CO (right) velocity fields of NGC 7899. The isovelocity contours are spaced every 20 km s^{-1}.

6.2.2 Images and Moment Maps

Integrated flux maps for both the HI (left) and CO (right) can be found in Figure 6.5. As with UGC 6168, we detect a significant reservoir of centrally located CO. Unlike UGC 6168 there is no obvious ring. However, as UGC 7899 is a highly inclined galaxy, it will not be clear whether a ring exists until a deprojected surface density is derived.

Figure 6.6 presents velocity fields for UGC 7899 for both our HI (left) and CO (right) observations. As UGC 7899 is highly inclined, the velocity fields are not representative of the full rotation curve and a PV diagram is required to fit a rotation curve. However, we can still note general trends from the velocity field. Both velocity fields are very smooth, showing well-ordered rotation. The closed contours in the HI velocity field suggest a declining rotation curve at large radii (especially in the southern half of the galaxy). There are no signs of non-circular motion, but for a highly inclined galaxy, the only way to confirm this is by using software such as TiRiFiC (Józsa et al. 2007), which fits directly to the data cube. The CO is not resolved enough to make any significant statements.

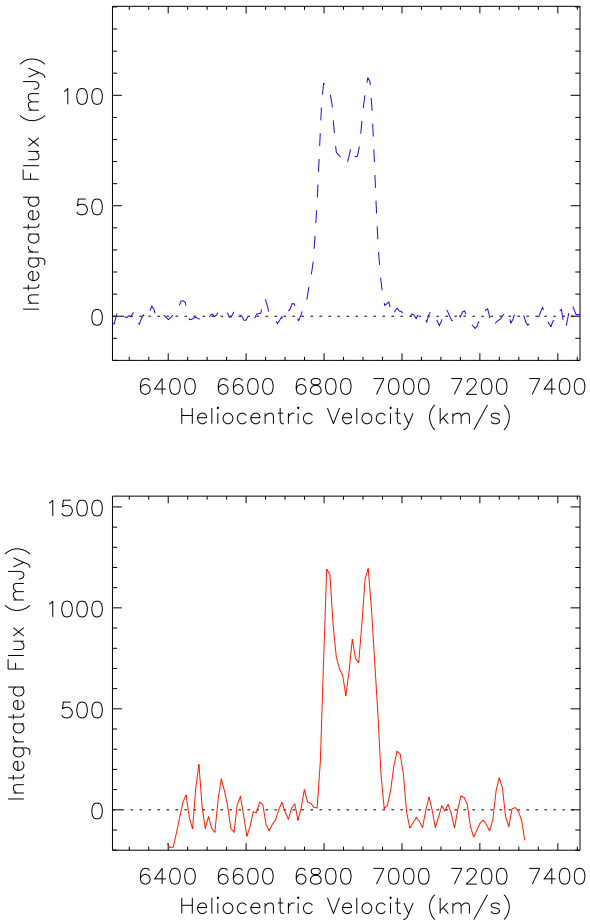

Figure 6.7: HI (top) and CO (bottom) spectra of NGC 5230. For The HI spectrum, only the single-dish ALFALFA (blue dashed lines) is available.

6.3 NGC 5230

6.3.1 Spectra

Figure 6.7 presents our HI (top) and CO (bottom) spectra for NGC 5230. For the GMRT HI observations of NGC 5230, only the integrated flux map and velocity field are available, and so only the ALFALFA HI spectrum is plotted. Bye eye, the CARMA CO spectrum

shares many features with the ALFALFA HI spectrum: because the galaxy is nearly face-on and quite massive in both HI and CO, both spectra are very tall and narrow. However, we detect significant differences between both the velocity width and the systemic velocity (see 6.1). As the CO is confined to the center of the galaxy (see §6.3.2), if the two phases are kinematically linked, it is unsurprising that the velocity width for CO is narrower. I cannot account for why the systemic velocities disagree significantly. But, in practical terms the 8 km s^{-1} difference is approximately the size of a single channel in either the ALFALFA or CARMA observations, and thus is likely unimportant.

The CO flux of the CARMA spectrum is 129.8 Jy km s^{-1}, which corresponds to a total H_2 mass of 10^{10} $M_\odot$, or an H_2 gas fraction of 0.31. This puts NGC 5230 just at the average H_2 gas fraction value observed by Saintonge et al. (2011a).

6.3.2 Images and Moment Maps

In Figure 6.8, I present our integrated flux maps of NGC 5230, both in HI (left) and CO (right), both overlaid on SDSS images. NGC 5230 is a nearly face-on massive spiral galaxy with well-defined arms. Like the other HIghMass galaxies, we can trace the HI emission well beyond the optical disk of the galaxy. Like UGC 6168, there is a clear hole in the HI in the center of the galaxy, which is filled with H_2. Because NGC 5230 is nearly face-on, the hole effect is much more obvious. Interestingly, there appears to be little CO emission in the southern arm of the galaxy: what process is suppressing star formation there, as compared with the other spiral arms?

We must be careful in interpreting the extend of the CO emission. Compared to the other galaxies observed with CARMA, the CO emission is very extended, reaching the well

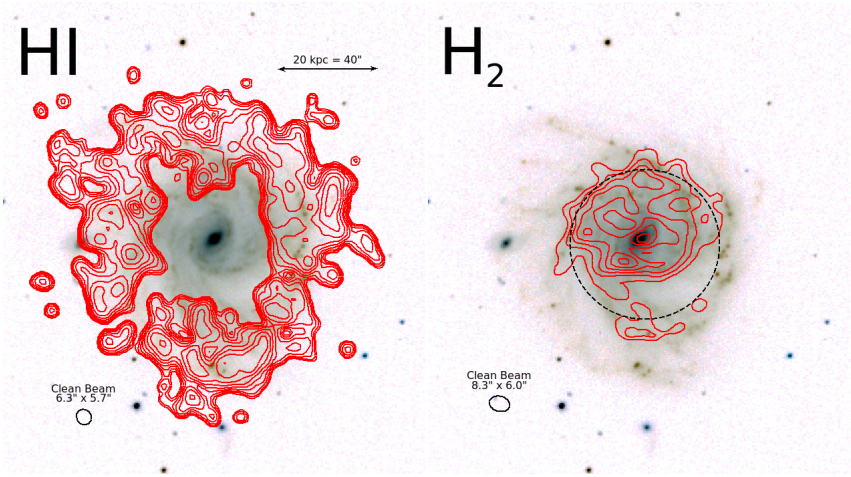

Figure 6.8: HI (left) and CO (right) integrated flux maps of NGC5230. Because of the extremely high signal to noise of the GMRT HI observations, the contours begin at 4σ and then each successive contour is $\sqrt{2}$ times the previous contour. The CO observations use our usual 4σ first contour plus 2σ at each successive contour scheme. The black dashed line indicates the primary beam size of CARMA, approximately $1'$. Both images are overlaid on an inverted SDSS image in the g, r, and i bands.

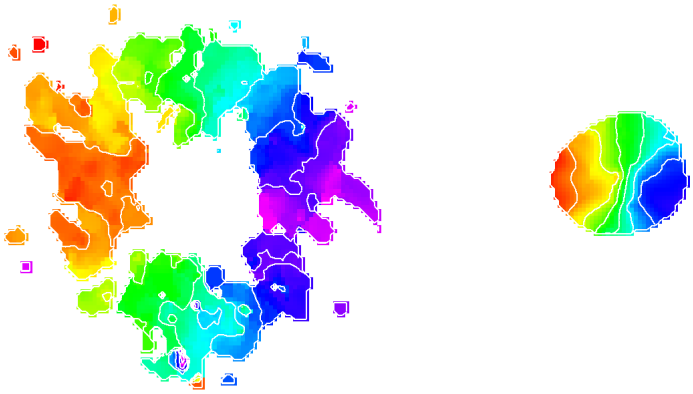

Figure 6.9: HI (left) and CO (right) velocity fields of NGC5230. Isovelocity contours are spaced every 20 km s^{-1}.

beyond the half power primary beam of CARMA ($1'$, the black dashed circle); I have chosen to image out to the 20% response contour. However, preliminary CO observations of this galaxy, which imaged further to the east, suggest that the emission would not be detectable beyond the 20% response contour.

Galaxy	Instrument	Flux	W50	V_{sys}
		Jy km s^{-1}	kms s^{-1}	kms s^{-1}
		(1)	(2)	(3)
UGC 6168	VLA	7.36 ± 0.28	362.9 ± 3.1	8078.7 ± 2.2
	ALFALFA	6.53 ± 0.12	363 ± 4	8073 ± 3
	Difference (σ)	2.7	0.02	1.53
	CARMA	8.11 ± 0.60	368.0 ± 7.7	8079.2 ± 5.4
	Difference (σ)	—	0.57	0.09
UGC 7899	VLA	12.56 ± 0.34	473.0 ± 3.5	8694.1 ± 2.5
	ALFALFA	6.70 ± 0.13	433 ± 22	8696 ± 16
	Difference (σ)	9.7	1.8	0.12
	CARMA	36.6 ± 2.1	390.9 ± 7.5	8696.3 ± 4.3
	Difference (σ)	—	1.9	0.01
NGC 5230	ALFALFA	13.97 ± 0.09	152 ± 2	6857 ± 1.4
	CARMA	129.8 ± 5.7	131.9 ± 2.0	6865.5 ± 1.4
	Difference (σ)	—	7.1	4.3

Table 6.1: Comparison of derived quantities from the VLA, ALFALFA, and CARMA spectra of each galaxy. Derivation of ALFALFA measurements is discussed in Haynes et al. (2011); VLA measurements are derived from spectra in the same way, but with $W50$ measurements corrected for instrumental broadening as discussed Springob et al. (2005); Column 1: The total integrated flux density of the galaxy; Column 2: The full velocity width at half of the peak emission; Column 3: The systemic heliocentric velocity of the galaxy, using the optical convention. All reported errors are 1-σ uncertainties using standard propagation of uncertainty.

Galaxy	log M_{HI}	log M_{H_2}	log(M_{H_2}/M_{HI})
	$M_\odot$	$M_\odot$	kms s^{-1}
	(1)	(2)	(3)
UGC 6168	10.35	8.96	-1.39
UGC 7899	10.42	9.68	-0.74
NGC 5230	10.53	10.02	-0.51

Table 6.2: HI and H_2 masses and gas fractions. The HI masses are from ALFALFA, while the H_2 masses are calculated from CO fluxes according to Equation A.17.

Figure 6.9 shows the GMRT HI (left) and CARMA CO (right) velocity fields. The CO field is extremely smooth, but we can see some irregularities in the HI. As NGC 5230 is nearly face-on, these irregularities may be due to the turbulence in the gas rather than a deviation from ordered rotation. Unlike UGC 6168 and 7899, there are several beams across the CO emission in NGC 5230, and so I will be able to make an independent rotation curve for the CO. The twisting of the major axis at small radii suggest noncircular motions in the CO.

CHAPTER 7

FUTURE WORK

While much work has been done on both the Virgo ETDs and the HIghMass galaxies projects, there are still many avenues of inquiry which remain. In this chapter, I present further work which I intend to do on both the Virgo ETDs and the HIghMass sample.

7.1 Virgo Dwarf Galaxies

The combination of the Virgo cluster's proximity ($\sim$ 16 Mpc) and richness ($>$ 1000 members) compared with the low ($\lesssim 10^8$ $M_\odot$) HI masses and rarity (6 out of $>$ 300) of the red gas-bearing ETDs suggests that finding additional gas-bearing ETDs in other clusters is difficult at best. Instead, future work will focus upon better constraining the evolutionary histories of this sample via deeper observations and simulations.

7.1.1 Resolved HI Observations

Recently, I have begun a campaign of VLA observations to resolve the HI emission in the red ETDs in order to better constrain their origins. In particular, there are three features that I want to investigate closely: extended or truncated emission, rotational structure, and the symmetry of the gas distribution.

It is well-known that HI disks of stripped galaxies in Virgo are truncated (e.g., Giovanelli and Haynes 1983, Cayatte et al. 1990; Chung et al. 2007; Chung et al. 2009). If the gas is newly accreted and not yet settled, we expect HI emission to extend significantly beyond the

optical radius of the galaxy. However, observing only extended HI emission would also be consistent with an unstripped galaxy; we would expect our HI-detected LTDs to also exhibit extended emission, for example.

Flat, rotating, star-forming disks observed are observed even in highly stripped Virgo galaxies, from massive spirals to dwarfs (Chung et al. 2007; Chung et al. 2009; Toloba et al. 2011). If the gas is newly accreted, there is no requirement for the gas to have the same angular momentum as the rest of the disk, and large warps are possible.

Finally, resolving the emission allows us to examine how symmetrical the gas is and possibly determine the form of accretion. Hot-mode accretion, believed to dominate in clusters, is roughly spherically symmetric while cold-mode accretion, which dominates for low-mass galaxies, is directed along gas filaments and is asymmetrical. If accretion is not spherically symmetric, the centroid of gas emission is expected to be significantly offset from the optical disk of the galaxy. We would also observe these significant offsets if the atomic gas were recently acquired during an encounter with an HI-bearing galaxy or a free HI cloud in the Virgo cluster (Kent et al. 2007; Kent et al. 2009). If the gas is not recent, then we expect it to appear either quite symmetric (if unstripped), or with a tail pointing away from the center of the cluster (if being stripped).

Figure 7.1 presents a preliminary integrated flux map of the HI in VCC 190. It is overlaid on an SDSS r-band image, with the optical image heavily adjusted to improve contrast. The contours clearly show that the HI emission appears coincident, but offset from the optical emission in the galaxy. Ott et al. (2012) made use of the VLA to observe the HI in the dwarf galaxies studied by Weisz et al. (2011), including several dwarf transitionals. Suggestively, the dwarf transitional DDO 6 this sample also shows this highly asymmetric, offset emission.

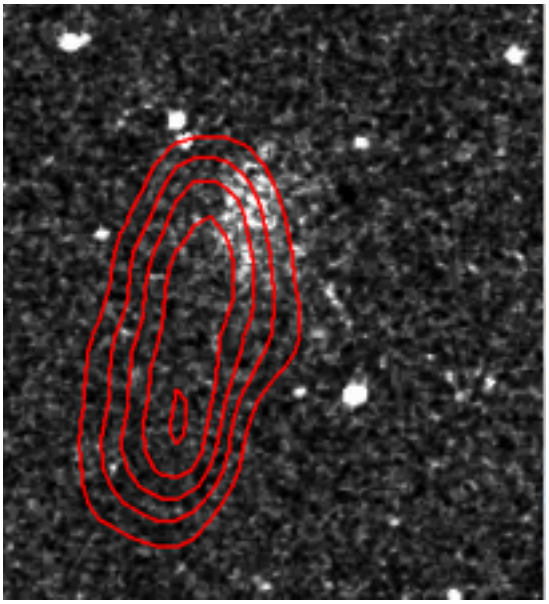

Figure 7.1: A (very) preliminary integrated flux map of VCC 190, overlaid on an SDSS r-band optical image.

7.1.2 Simulations

The reaccreted HI gas hypothesis leaves several questions unresolved, including two which I find particularly difficult. First, how capable is a dwarf galaxy of accreting diffuse gas? Perhaps the gas needs to be already in a large HI cloud complex, such as that observed by Kent et al. (2007) and Kent et al. (2009). Such clouds can contain $> 10^8$ $M_\odot$ of HI, more than any of the individual ETDs. Second, how is it that the ETDs have acquired just the right mass of gas, putting them at typical gas fractions for their stellar mass?

One way that these questions can be answered is via simulations. A recent paper by Verbeke et al. (2014) investigates a similar situation of a gas-rich dwarf galaxy accreting a cloud of HI. After accreting it, the cloud ignites star formation after some latency period. I intend to follow their methods, but with the initial conditions of a head-on merger between a gas-poor ETD and HI clouds of varying masses and observing how much gas is actually

acquired by the galaxy, and how long before a star formation event occurs.

7.2 HIghMass

Aside from acquiring and reducing more HI, CO, and other wavelength observations of the HIghMass galaxies, there are several ways that the data reduction pipeline could be improved. In some cases, these methods are not available in the standard data reduction software (either CASA or GIPSY), and must be developed independently. The following sections, on improving the rotation curves, H_2 mass distribution estimates, and dark matter profiles, are a few of these possible routes for improvement.

7.2.1 Rotation Curves

While velocity fields fail to capture the rotation of highly inclined galaxies, they are not the only way to produce rotation curves. The PV diagram fitting method, as described in §A.5.1 is one such method. However, both the tilted ring fitting of velocity fields and the PV diagram first reduce a three dimensional data cube to a two dimensional problem which both greatly reduces the amount of computation required, but also removes a great deal of information.

I plan to do future data reduction using TiRiFiC (Józsa et al. 2007; Józsa 2007). The strategy of TiRiFiC is to follow the standard assumptions of a tilted ring fit, but to operate on a data cube rather than a velocity field. This removes the ambiguity of the velocity field (multiple velocity structures at high inclination) and the difficulties of fitting a PV diagram (one single inclination and position angle must be assumed). In addition, it is much more

straightforward to enforce a flat inner disk geometry in TiRiFiC than for the ROTCUR task.

7.2.2 Unseen H_2 Masses

Despite our carefully estimated CO integrated fluxes based on the work of Saintonge et al. (2011a), not all of the galaxies observed in CO using CARMA were detected. This is unsurprising: the work of Saintonge et al. (2011a) examines a sample of galaxies chosen by high stellar mass ($> 10^{10}$ $M_\odot$) galaxies, while the HIghMass sample is specifically gas-rich galaxies which appear to be under-performing in star formation. They thus have less mass in H_2 compared to galaxies of similar colors and stellar masses. However, these non-detections are not a failure. In addition to the CARMA CO observations, the same galaxies have also been observed in CO using the IRAM 30m single dish telescope, and were successfully detected. Because IRAM has a 22" beam, we can smooth or taper the interferometer observations to different resolutions to constrain the emission.

We have seen that the local SFE for the HIghMass galaxies is similar to that observed in local galaxies of varying masses (Leroy et al. 2008; Saintonge et al. 2011b), although the spread is not negligible. For galaxies without observed CO, we can assume a SFE and investigate whether or not the inferred surface densities match our expectations of total gas mass. Galaxies which significantly deviate from expectations make excellent candidates for future observations.

7.2.3 Dark Matter Profiles

The Einasto profile (Einasto 1965), originally intended to model the distribution of stellar light in galaxies, has been proposed by Navarro et al. (2004) as a better model fit to simulated ΛCDM dark matter profiles. It has been shown to be a significant improvement over either the ISO or NFW profile when fit to both simulated (Navarro et al. 2010) dark matter halos and also the derived halos of the THINGS galaxies (Chemin et al. 2011). The Einasto profile takes the form:

$$\rho(r) = \rho_{-2} e^{-2n\left[\left(\frac{r}{r_{-2}}\right)^{1/n} - 1\right]} \tag{7.1}$$

Where r_{-2} is the radius where the slope of the profile becomes $\propto r^{-2}$, and ρ_{-2} is the density at that radius. n is known as the shape parameter of the Einasto profile. Unfortunately, the Einasto profile must be numerically evaluated, and as such, is not included as part of the GIPSY ROTMAS package.

APPENDIX A

DETAILED DESCRIPTION OF DATA REDUCTION

A.1 Observations and Observing Strategy

The details of each galaxy's synthesis observations are given in Table A.1.[1] Only the VLA and CARMA data were reduced by me. The WSRT produces data cubes for its users, and the GMRT observations were performed and reduced by collaborators. The following discussion will thus only concern the VLA and CARMA observations.

The VLA cycles through several configurations in an 18 month cycle, from configuration A (the most extended; highest resolution; lowest sensitivity per unit time) to D (the most compact; lowest resolution; highest sensitivity per unit time). To combine the benefits of high sensitivity and resolution, we observed using the D, C, and B configurations for 2, 4, and 9.5 hours, respectively. This gives us the same sensitivity as The HI Nearby Galaxy Survey (THINGS; Walter et al. 2008), although because their galaxies are much closer ($d \sim 10$ Mpc compared to $d \sim 100$ Mpc), we have less ability to resolve structure. Because of technical limitations during the VLA upgrade project, observations were performed in multiple spectral windows which were later combined to produce a single 8.5 MHz wide window (see Figure A.1). Each channel has a native width of 1.7 km s^{-1} later smoothed to 7 km s^{-1}. The full bandwidth of this combined window is ~ 1800 km s^{-1}, enough to both completely encompass each galaxy's HI emission and to fully determine any continuum emission.

CARMA has a similar configuration cycle, varying from A to E. These observations were performed solely in configuration E, which at 115 GHz nearly matches the VLA spatial

[1]Much of this Appendix is an excerpt from Hallenbeck et al. (2014), which has recently been accepted for publication in the AJ.

Galaxy Name	Telescope (1)	Observations (2)	Status (3)
UGC 5543	VLA	D (2 hr), C (4 hr), B (9 hr)	-
UGC 5711	VLA	D (2 hr), C (4 hr), B (9 hr)	-
UGC 6066	VLA	D (2 hr), C (4 hr), B (9 hr)	-
UGC 6168	VLA	D (2 hr), C (4 hr), B (9 hr)	D
UGC 7220	VLA	D (2 hr), C (4 hr), B (9 hr)	D
UGC 7899	VLA	D (2 hr), C (4 hr), B (9 hr)	D
UGC 8789	VLA	D (2 hr), C (4 hr), B (9 hr)	-
UGC 9037	VLA	D (2 hr), C (4 hr), B (9 hr)	D
UGC 9334	VLA	D (2 hr), C (4 hr), B (9 hr)	-
UGC 12506	VLA	D (2 hr), C (4 hr), B (9 hr)	D
UGC 6168	CARMA	E (23.4)	D
UGC 7220	CARMA	E (7 hr)	N
UGC 7686	CARMA	E (11 hr)	D
UGC 7899	CARMA	E (13.6 hr)	N
UGC 8573	CARMA	E (4.2 hr)	D

Table A.1: Observations of the HIghMass galaxies undertaken at the VLA and CARMA. Column 1: telescope used for observations; the VLA observed the HI line, and CARMA the ^{12}CO(1-0) transition as a tracer of H_2; Column 2: duration of observations in each telescope configuration; Column 3: detection status. "D" galaxies were successfully detected, while "N" galaxies are non-detections. "-" galaxies have not been reduced yet.

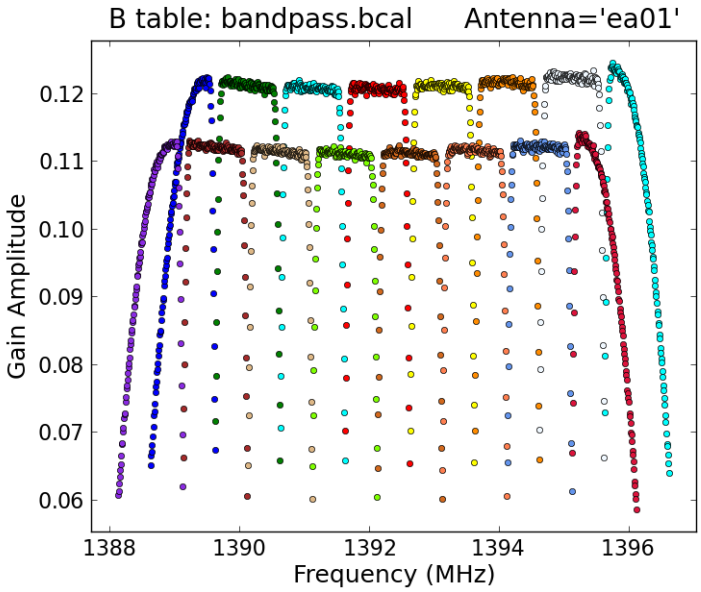

Figure A.1: The 16 subbands and their uncalibrated response to a flat continuum source during one observation. After calibration, the low sensitivity window edges are removed and the 16 subbands are combined into one 8.5 MHz window during data reduction.

resolution at 1.4 GHz. For the VLA observations, the total HI integrated flux density was both known and quite large. However, for the CO observations, the total integrated flux density was unknown and suspected to be quite small. I estimate H_2 masses using the scaling relationships between M_{H_2}/M_* and $u-r$ color found by Saintonge et al. (2011a) for massive, relatively gas-rich galaxies. This allows us to vary integration times based on how much H_2 each galaxy is expected to contain. CARMA's capabilities are such that a single 250 MHz in 3 bit mode (79-channels, ~ 8.2 km s^{-1} channel width at 115 GHz) is enough to contain the emission and sufficient channels to fit continuum emission; thus no multi-window splicing is required.

A.2 Data Pipeline

Data reduction is done mostly using NRAO's CASA[2] software. As CASA is still under development and current routines are aimed for continuum, rather than spectral line analysis, I supplement CASA with the older GIPSY[3] software when necessary.

A.2.1 Flagging and Calibration

The flagging and calibration of visibilities is done using standard CASA tasks. I use PLOTMS to view slices of the visibilities and FLAGCMD to execute multiple flagging commands at one time. Our bandpass shapes and fluxes are calibrated using the standard BANDPASS, GAINCAL, SETJY, and FLUXCAL tasks from observations of the standard VLA calibrators. CARMA observations additionally use planets for bandpass and flux calibration when avail-

[2]The Common Astronomy Software Applications package is under development by the NRAO.
[3]The Groningen Image Processing SYstem was developed at the Kapteyn Astronomical Institute.

able.

A.2.2 Continuum Subtraction

The sky at L-band is littered with faint continuum sources. Thus, accurate continuum subtraction is vital for our VLA observations. There are multiple methodologies for continuum subtraction in interferometric data. These include subtraction in the visibility domain using UVCONTSUB, subtraction in the image domain using IMCONTSUB, and a more complex method that combines the two, utilizing UVSUB.[4]

UVCONTSUB attempts to characterize the continuum by fitting polynomials to line-free channels in the complex visibilities themselves. IMCONTSUB fits and subtracts polynomials at each sky position in the final data cube. In many cases, the two methods are of similar quality, but subtleties can be found in which one method performs more accurately. For example, UVCONTSUB has largest artifacts of continuum subtraction near the continuum source, with such errors falling off with angular distance from the source while IMCONTSUB has the opposite effect (Sault 1994). Both, however, face a similar restriction in that they perform best in a small field of view given by (Cornwell et al. 1992):

$$\theta \ll \frac{\nu}{\Delta\nu}\theta_c \tag{A.1}$$

Where ν is the observation frequency, $\Delta\nu$ is the bandwidth, and θ_c is the clean beam size. For our VLA observations ($\nu = 1.4$ GHz; $\Delta\nu = 8.5$ MHz; $\theta_c \approx 6''$), this scale is $16'$, about half the $30'$ field of view of the VLA at 1.4 GHz. For CARMA ($\nu = 115$ GHz; $\Delta\nu = 250$ MHz; $\theta_c \approx 8''$), this scale is $60'$, much larger than CARMA's $1'$ field of view at 115 GHz. Thus, I choose to use UVCONTSUB for our CARMA data, but not for the VLA.

[4]While I use the CASA names for each of these tasks, each is an adaptation of tasks implemented in AIPS: UVLIN, IMLIN, and UVSUB, respectively, and are referred to as such in the articles cited in this section.

The methodology used of the task UVSUB, works in both the visibility and image domain. First, a continuum image is produced using line-free channels. Then, a model of the continuum emission as a collection of point sources is produced by CLEANing the continuum image. This model is then converted back into visibility domain and subtracted from the visibilities. UVSUB avoids the narrow-field restriction of the previous two methods, but suffers from the drawbacks of CLEAN, notably that it is incredibly slow and does not adequately characterize extended sources of emission.

I thus use UVSUB to perform continuum subtraction for our VLA observations, supplemented by IMCONTSUB when the final image cube proves to have remaining residual emission, either because cleaning deeply enough to remove fainter sources is too time intensive, or because the continuum sources are extended, as recommended by Cornwell et al. (1992).

A.2.3 Data Cube Production

It is at this stage, after each set of visibilities has been individually calibrated and continuum-subtracted, that the visibility sets for each galaxy are combined into a single image cube and cleaned down to twice the image cube rms using CLEAN. I find that a Briggs robustness weighting of $0.5 - 1.0$ gives the best tradeoff between noise and beam size for our VLA observations. For CARMA which are of lower signal-to-noise, I vary the robustness depending on the strength of the emission. For one galaxy (UGC 6168), the emission is so weak that I apply a tapering to the visibilities, throwing away those with baselines longer than 10 kλ.

The response of both the VLA and CARMA as a function of angular distance from pointing center is well known, and can be accounted for during cleaning of the image, by multiplying each pixel by (sensitivity%)$^{-1}$. For the VLA, the HI emission of our galaxies fills

a small ($\sim 1' - 2'$) portion of the $30'$ primary beam, never going below the 99% sensitivity isophote, and so I do not apply this correction. For CARMA, the size of CO emission ($\lesssim 1'$) is comparable to the $1'$ primary beam, and so this primary beam correction is highly significant and applied. I choose to image out to the 20% response isophote of CARMA, and so the noise at the edge of the CARMA images is 5 times larger tahn for the center of the pointing.

The standard clean methodology is to model emission as a collection of point sources. While this works well for unresolved or partially resolved targets, I expect the HI (and to a lesser extent, the H_2) to be quite extended, and so I use multi-scale clean (Cornwell 2008). Instead of the typical assumption of the source being simply a collection of point sources, multi-scale clean models additionally allows the source to be made of two-dimensional Gaussians of varying sizes, usually the beam width and a few times the size of the beam. In addition to this being a more physical model of the distribution of the HI emission, multi-scale clean is shown to reduce effects related to over- and under-cleaning the image cubes (Rich et al. 2008).

A.3 Moment Maps

Because 3-D data cubes are difficult both to visualize and to operate on computationally, moment maps are traditionally made. Such maps collapse the data cube along the frequency to produce a 2-D image. They are generally of the form:

$$M_i(x, y) = \sum_j S_j(x, y) \Delta v (v_j)^i \tag{A.2}$$

Where $M_i(x, y)$ is the ith moment map at a given (x, y) sky position, $S_j(x, y)$ is the cleaned data cube flux in the jth channel and given sky position, in units of Jy beam^{-1}. Δv is the

channel width in km s^{-1}, and v_j is the velocity corresponding to the jth channel of the data cube. Even though the channel width is technically constant only in frequency space, rather than velocity space, it is often treated this way. The CASA task IMMOMENTS is used to create these moment maps.

Because our methods often part from the strict definition of the moment maps given above, and to give them more physically motivated names, I refer to them as integrated flux maps (moment 0) and velocity fields (moment 1).

A.3.1 Integrated Flux Maps

An integrated flux map is a quick way of examining the location and strength of emission of a galaxy, as projected onto the sky, ignoring the possibly complex velocity structure. The trivial way of producing integrated flux maps is given in A.2, with $j = 0$.

However, galaxies do not occupy the same position on the sky in each channel. Because of each galaxy's ordered rotation, any one sky position will only contain a few channels with any significant emission. As the noise on summing over N channels goes as $\sqrt{N}$, simply adding the intensities of all channels which contain any emission anywhere in the image would leave us with higher than necessary noise. Instead, we wish to sum each pixel over only the channels where there is emission, taking into account how this will change with position in the image. To do this, I mask out pixels without emission before performing the sum. To create this mask, I first smooth the image cube with a Gaussian with twice the size of the restoring beam, clip the smoothed image at the 3σ level, then apply this mask to the original image cube. The cube, after masking this way, is then used to make a standard moment 0 map. For the VLA observations, this method works quite well. However, our CARMA data

is of lower signal-to-noise ratio, and also nearly fills the primary beam of CARMA. Near the edge of the CARMA images, the cube noise is multiplied by a factor of 5 (see §A.2.3), which makes applying a single signal-to-noise cutoff less effective. I choose to take the masked data cube and manually mask out the most obvious noise, which significantly increases the quality of all moment maps.

A.3.2 Velocity Fields

Velocity fields give an impression of the 'typical' velocity at each sky position, discarding the information about the strength of emission. They are typically produced via A.2, with $j = 1$, and normalized to the total flux along the line of sight, so that the map has units of km s^{-1}:

$$M_1(x, y) = \frac{\sum_j S_j(x, y)(\Delta v)v_j}{\sum_j S_j(x, y)(\Delta v)} \tag{A.3}$$

Once again, I argue that performing a masking as in A.3.1 produces the cleanest possible moment 1 map.

However, there are alternate methods of note to compute velocity fields. Such methods include fitting Gauss-Hermite Polynomials along each line of sight, which I will now discuss. Gauss-Hermite polynomials are gaussians modified to include an additional skewness parameter, and have the form (van der Marel and Franx 1993):

$$f(v) = \frac{\tilde{A}}{2\pi} e^{-\frac{y^2}{2}} \left[1 + \frac{\tilde{h}_3}{\sqrt{3}} \left(2y^3 - 3y\right)\right]; \qquad y \equiv \frac{v - \tilde{V}}{\tilde{\sigma}} \tag{A.4}$$

where the fit parameters $\tilde{A}$, $\tilde{V}$, $\tilde{\sigma}$ correspond roughly, but not exactly, to the more familiar amplitude, central velocity, and width of a simple Gaussian fit. $\tilde{h}_3$ a measure of the skewness, and is the coefficient of the fit corresponding to the 3rd Hermite polynomial. The desired value at each point, $V(x, y)$, is the location of the peak of this distribution, and can be

calculated from the fit parameters, and is done automatically by the GIPSY task XGAUFIT. The addition of this skewness parameter allows for a more robust measure of $V(x, y)$ than the simpler methods of taking a simple weighted average, the frequency of peak emission, or the fitting of a Gaussian to the spectrum. This is especially true for galaxies with irregular profiles, and where emission is weak and the signal-to-noise ratio is low (van der Marel and Franx 1993; de Blok et al. 2008). I will note for each galaxy when the standard moment 1 velocity field is used, and when the Gauss-Hermite velocity field is superior, based on later investigation.

A.3.3 Position-Velocity Diagrams

A Position-Velocity (PV) Diagram is another way of rendering a 3-D data cube into a 2-D image. However, instead of removing the velocity axis, a position axis is instead removed. This is done by taking a few arcsecond wide slice through the data cube. Usually, this slice is aligned along the major axis. A PV diagram is useful for investigating complex velocity structure not encapsulated by the velocity map and for asymmetries in the galaxy. For highly inclined (inclination $\gtrsim 80°$) galaxies, a PV diagram is often used for obtaining rotation curves, rather than a velocity field.

A.4 Comparison with ALFALFA Spectra

Interferometers, unlike single dish telescopes, are known to "miss" flux on the largest scales, meaning that for resolved objects such as nearby galaxies, there is significant uncertainty (on the order of 5%-10%) on the total integrated flux of the galaxy. In order to understand

the impact of this missing flux, as well as how well our data accurately represents the true emission of each galaxy, I compare our VLA HI observations with those of ALFALFA, and our CARMA CO observations with single dish observations performed at IRAM.

However, the ALFALFA and IRAM observations are unresolved, and thus give only both global (that is, unresolved spatially) spectra and spectra-derived quantities such as the total integrated flux density and velocity width. In order to perform a comparison, we must find a method of converting a data cube into a spectrum. One method would be to take the masked data cube (as described in §A.3.1) and integrate over each channel. This method has one major problem: the noise in such a spectrum is always positive, as it is added up only where emission (or noise above the 3σ level) is present, and not gaussian and zero-centered as is generally assumed for fitting analysis. Instead, I use the integrated flux map to produce a uniform mask on every channel of our original data cube, and the spectrum is produced by integrating over this region. This final spectrum has the expected gaussian noise. As the IRAM 30m dish has a beam size of $22''$, I further restrict our integration to a $22''$diameter circle in order to produce a fair comparison.

The CASA task FEATHER seeks to combine the more stable "true" flux from a single dish observation with the flux observed with an interferometer (or any two data cubes at different resolution). It does this by converting the two observations back into visibility data, then creating a new image from the combined visibilities. Unfortunately the task is still experimental and suffers from a few idiosyncrasies when attempting to combine ALFALFA and the VLA data, and is at this time still unsuitable.

A.4.1 Spectral Properties

The fitted properties of the ALFALFA spectra are: the total integrated flux density (F_{21}), the velocity width at half of peak emission ($W50$), and the optical recessional velocity ($v_{\rm sys}$). Discussions of how fluxes and line widths for ALFALFA are derived can be found in Giovanelli et al. (2005) and Haynes et al. (2011). I use the same method, except that I correct for instrumental broadening using the method derived by Springob et al. (2005), which is not specific to the particular correlator setup of ALFALFA. Integrated 21 cm fluxes (F_{21}) are calculated from the individual channels of the spectra (S_i) where emission is observed:

$$F_{21} = \sum_{i=j}^{j+N} S_i \Delta v \tag{A.5}$$

Where Δv is the channel width in km s^{-1}, assumed to be constant across the galaxy width.

Straight lines are fit to the outer edges of the HI profile between 15% and 85% of peak emission from each horn. I then use this fit to determine the velocity corresponding to where the profile reaches 50% of peak emission on the red- and blue-shifted sides of the profile, v_R and v_B. The velocity width, $W50$, and systemic (or recessional) velocity, $v_{\rm sys}$, are then defined as

$$W50 \equiv v_R - v_B \tag{A.6}$$

$$v_{\rm sys} \equiv \frac{v_R + v_B}{2} \tag{A.7}$$

The velocity widths are then corrected for instrumental broadening based upon their signal-to-noise ratio (See Table 2 in Springob et al. 2005); ALFALFA uses a simpler single-correction factor method. Like ALFALFA, I do not include a $1 + z$ correction for redshift broadening, or corrections for inclination or turbulent motion. All errors reported are 1σ uncertainties using standard propagation of uncertainties, assuming that the spectral rms is the dominant source of error.

A.5 Rotation Curves

A rotation curve indicates the characteristic orbital velocity in a galaxy at a given radius from the center. In general, it is assumed that orbits in a galaxy are circular, with any deviation from circular orbits thrown into the catch-all category "non-circular motion," which encompasses everything from elliptical orbits to widespread inflows. For some galaxy inclinations, it is possible to further characterize these non-circular velocities, and look for trends in the inclination and position angle as a function of radius.

In the following analyses, I will separate the analysis methodologies to be applied to galaxies in three separate categories: nearly edge-on galaxies ($i \gtrsim 80°$), nearly face-on galaxies($i \lesssim 40°$), and inclined galaxies (with $40° \lesssim i \lesssim 70°$).

A.5.1 Nearly Face-On Galaxies & Inclined Galaxies

For galaxies which are face-on to inclined, each line of sight crosses only a single structure in the galaxy. That is, each pixel in the velocity field can be treated as containing only a single piece of information, independent from every other pixel (modulo the effects of a finite beam size). This can be seen quite clearly in the PV diagram of UGC 9037 in Figure 5.4, a galaxy with an inclination of 60°.

For these galaxies I fit tilted ring models following the method of Begeman (1989), using the gipsy task ROTCUR. This model assumes that the gas can be modeled as a series of solid, concentric rings centered at image coordinates (x_o, y_o) and the same systemic velocity ($V_{\rm sys}$) about which they rotate. Each ring j is allowed to have an independent rotational velocity ($V_{{\rm rot},\,j}$), expansion or contraction speed ($V_{{\rm exp},\,j}$), inclination (i_j), and position angle (PA$_j$).

The velocity field is then modeled as (Begeman 1989):

$$\hat{V}(x,y) = V_{\rm sys} + V_{{\rm rot},\,j}\cos\theta\sin i_j + V_{{\rm exp},\,j}\sin\theta\sin i_j \tag{A.8}$$

$$\cos\theta \equiv \frac{-(x-x_o)\sin{\rm PA}_j + (y-y_o)\cos{\rm PA}_j}{r_j} \tag{A.9}$$

$$\sin\theta \equiv \frac{-(x-x_o)\cos{\rm PA}_j + (y-y_o)\sin{\rm PA}_j}{r_j} \tag{A.10}$$

I choose to Nyquist sample the VLA beam, and so each ring has a width of half the VLA beam size, or $3''$[5]. At a typical HIghMass galaxy distance of 100 Mpc, this corresponds to $\sim$1.5 kpc.

In practice, finding the best fit to all of these parameters simultaneously is intractable: a $1'$ radius galaxy has 20 rings and thus 83 free parameters. Instead, I run ROTCUR multiple times, each time allowing different sets of parameters to vary: $(x_o, y_o, V_{\rm sys})$, $(V_{{\rm rot},\,j},\, V_{{\rm exp},\,j})$, or $(i_j,\, {\rm PA}_j)$, until the fit no longer improves.

de Blok et al. (2008) argue that the formal fit uncertainties under-represent the actual uncertainty in the ring velocities. In general, the rotational and expansion velocity uncertainties $\sigma_{\rm Vrot}$ and $\sigma_{\rm Vexp}$ are typically $\sim 1-5$ km s^{-1}, while from the velocity field residuals $\hat{V}-V$, I calculate typical standard deviations $\sigma_{\rm res}$ of $\sim 10-15$ km s^{-1}. Other traditional methods, such as fitting a receding and approaching side, and choosing the uncertainty to be half the difference in the two velocities, only work for significantly asymmetric galaxies. When reporting rotation curves, I use $\sigma_{\rm res}$ as the uncertainty on the velocities reported. This means that our uncertainties are not just on how uncertain our estimate of the rotational velocity of each ring is, but are also a measure of how appropriate a rigid rotating ring model is. For nearly face-on galaxies, these uncertainties are dominated by the random vertical motions of the gas, $\sim$ 11km s^{-1}, and are accepted as an irreducible uncertainty. Reported

[5]In order to make the VLA and CARMA observations directly and trivially comparable, I use $3''$ for the CARMA observations as well, even though half the beam size is closer to $4''$

uncertainties on the inclination and position angle are formal fit uncertainties. It should be kept in mind that the actual uncertainties on the inclination and position angle are unknown but somewhat larger. As the uncertainties on the inclination and position angle are not used in further calculations, this rough characterization of the uncertainty is sufficient.

In the end, I find that the moment 1 velocity field to produce significantly smaller residuals than the Gauss-Hermite velocity field (for UGC 9037, $\sigma_{\mathrm{mom1}} \sim 6$ km s^{-1} and $\sigma_{\mathrm{g\text{-}h}} \sim 13$ km s^{-1}), and is used in our analysis.

Characterization of Non-Circular Velocities

The tilted model implemented by ROTCUR is designed to model mostly flat disks (i.e. relatively constant i and PA) with possible warps at large radii, and not to account in detail for non-circular motions: inflows and outflows, whether radially or bisymmetric (i.e. bar-shaped), all appear the same. For flat galaxies with small or insignificant non-circular velocities, ROTCUR does its job well. For larger non-circular velocities, a more complex solution is required. One such solution is the GIPSY task RESWRI, which extends (A.8) with additional, higher-order harmonic velocity terms:

$$\hat{V}(x,y) = V_{\mathrm{sys}} + \sum_{k=1} m_{j,k} \cos(k\theta) \sin i_j + n_{j,k} \sin(k\theta) \sin i_j \tag{A.11}$$

Where the $m_{j,k}$ and $n_{j,k}$ are the velocity coefficients for each higher-order term. Note that $m_{j,k=1}$ is identical to the previous rotational velocity coefficients $V_{\mathrm{rot},\,j}$, and is often evaluated separately.

While RESWRI can account for different kinds of non-circular flows, it still suffers from a problem common to all tilted-ring models: disk geometry is degenerate with non-circular velocities: one can, by varying the position angle and inclination of the disk, allow for any

choice of 'expansion velocity' (e.g. Schoenmakers et al. 1997; Sellwood and Sánchez 2010). However, it is well known that the inner regions of real galaxy disks are very flat. Instead, I use the physically-motivated DiskFit package (Spekkens and Sellwood 2007; Sellwood and Sánchez 2010; Kuzio de Naray et al. 2012). DiskFit fits more realistic flat disk models to the observed data. For each galaxy with significant non-circular flows, we fit three models using DiskFit: a pure rotational model, a model which allows for radial flows, and one which models bisymmetric (bar-like) flows.

Even with the usage of RESWRI or the DiskFit package, one degeneracy remains: without knowing which side of the galaxy is closest to the observer, inflows are indistinguishable from outflows. Instead, we must rely on contextual clues to make an argument about whether non-circular flows are inward or outward. Such clues include looking for regions with large gaseous surface densities (see §A.6.1) and for marginal stability in the gaseous disk (§4.3.4).

A.5.2 Nearly Edge-On Galaxies

For nearly edge-on galaxies, each line of sight through the galaxy will observe structures at multiple velocities, causing the velocity field to be an inaccurate representation of the velocity. Rotation curves from velocity fields systematically underestimate the rotational velocities. For such galaxies, the usual method is to fit to the "envelope," the highest velocities observed at each position in a position-velocity (PV) diagram, either by fitting gaussians or tracing a particular isophote (Sancisi and Allen 1979; Sofue and Rubin 2001). I use the velocity field and ROTCUR to estimate a single inclination and position angle for the galaxy, and take use the position-velocity field at the fitted position angle. At each position along the PV diagram, I extract a spectrum and fit a 3rd order Gauss-Hermite polynomial. The final rotation curve is the velocity value for which the integrated area under the curve

is 3.3% from either the approaching or receding edge. For a gaussian fit (which our fit reduces to for a skew parameter of 0), this is equivalent to the 40% isophote for this slice, a commonly chosen value. The actual area chosen has a relatively small effect on the fit: our fits are consistent within errors with those produced by using 1 to 8% of the total area. The velocity is then adjusted for inclination:

$$v_{\rm rot} = \frac{v_{\rm obs}}{\sin i} \tag{A.12}$$

We note that for $i \sim 90^\circ$, the exact value of i has little effect on the correction:

$$v_{\rm rot} \approx \frac{v_{\rm obs}}{1 - \frac{1}{2}(\Delta i)^2} \approx v_{\rm obs}\,(1 + \Delta i) \tag{A.13}$$

Where the approximations are made under the assumption that $\Delta i \equiv \pi/2 - i$ is small. The final rotation curve's uncertainties are taken to be half the difference in the approaching and receding rotation curves.

This method diverges from the standard global isophote-tracing method (e.g. Sofue and Rubin 2001) because its results do not work with low signal-to-noise galaxies. The standard method is to choose a uniform intensity isophote to trace via

$$I_{\rm iso} = \sqrt{(\eta I_{\rm peak})^2 + (3\sigma)^2} \tag{A.14}$$

where η is some fraction of the peak intensity, and $I_{\rm peak}$ and σ are the peak intensity and rms of the PV diagram, respectively. Values of $\eta = 0.4$ are typical, but even for $\eta = 0$, we lose the ability to map the furthest tails of our galaxies, where emission is still clearly visible to the eye.

A.6 Mass Models

I treat each galaxy as being composed of up to five different components: HI, H_2, Helium, Stars, and Dark Matter. The Helium is assumed to be well-mixed with the hydrogen, and is merely a 1.33 multiplicative conversion factor to the HI and H_2 masses, and thus I only consider four independent components. I ignore the dust and metal masses as insignificant.

A.6.1 HI

Nearly Face-On and Inclined Galaxies

As discussed in §A.5.1, for nearly face-on and inclined galaxies, each pixel in the velocity field (and intensity map) correspond to a single structure in the galaxy, and so determining the surface densities is quite straightforward. I can calculate profiles of either the HI or H_2 from using the GIPSY task ELLINT, which integrates the moment 0 map in rings using the tilted ring fit. For HI we can simply use the standard conversion of flux to total mass:

$$\frac{M_{\rm HI}}{\rm M_\odot} = 2.36 \times 10^5 \frac{S_{\rm int}}{\rm Jy\ km\ s^{-1}} \times \left(\frac{d}{\rm Mpc}\right)^2 \tag{A.15}$$

Where $S_{\rm int}$ is the flux integrated over a particular ring, and d is the distance to the galaxy. This can be converted to a surface density by dividing by the area of the ring. The gas is assumed to be in an infinitely thin disk, and so face-on gas surface densities are simply a factor of $\cos i$ smaller than the observed values. The derived gas surface densities are largely insensitive to the exact tilted ring fit parameters, with the inclination i being the most important.

Nearly Edge-On Galaxies

For highly inclined galaxies, I use the Lucy-Richardson deconvolution (Lucy 1974; Warmels 1988; GIPSY task RADIAL). This method was specifically designed for galaxies which are only resolved along the major axis. Briefly, this method involves first summing the intensity map along the minor axis, reducing the observed intensities to a one dimensional distribution. A model of axisymmetric, uniform density, coplanar rings is then computed, taking into account that at each line of sight, multiple rings are contributing to the observed intensities. This model is iteratively changed until it matches the observed distribution. The final densities do not require any estimate of the inclination of the galaxy, only a kinematic center and position angle. Note, however, that because Lucy-Richardson deconvolution requires a galaxy of coplanar concentric rings, galaxies with significant warps are not well-modeled by the Lucy Method.

HI Radii

Broeils and Rhee (1997) found a tight linear relationship between a galaxy's total HI mass (log M_{HI}) and the diameter at which its deprojected surface density. This relationship was later extended to higher gas-fraction objects of the 'BlueDisks' sample (Wang et al. 2013; see Equation 3 of Broeils and Rhee 1997):

$$\log R_{\rm HI} = 0.51 \log M_{\rm HI} - 3.63 \tag{A.16}$$

I calculate an HI radius for each galaxy by fitting an exponential profile to the HI density and using it to estimate the radius where where $\Sigma_{\rm HI} = 1\ {\rm M}_\odot\ {\rm pc}^{-2}$. For galaxies which do not have an approximately exponential profile, I fit a straight line over a few radii near where the surface density crosses $1\ {\rm M}_\odot\ {\rm pc}^{-2}$.

A.6.2 Molecular Hydrogen (H_2)

For the H_2 masses, calculations are a bit more complex. H_2 has no detectable emission lines, except in regions where the H_2 is shocked. Instead, as is commonly done, I use CO as a tracer, specifically the ^{12}CO(1-0) rotational line. We must assume a conversion factor between the observed CO luminosity $L'_{\rm CO}$ (in units of K km s^{-1} pc^2) and the total H_2 mass, known as $\alpha_{\rm CO}$ (also known as $X_{\rm CO}$ in some of the literature). The conversion factor is known to vary significantly with metallicity and redshift (e.g. Wilson 1995, Arimoto et al. 1996) . Even though the HIghMass galaxies are gas-dominated and have poor star formation rates, they all have stellar masses $\gtrsim 10^{10}$ M$_\odot$, and thus I expect them to have metallicities similar to the Milky Way. I follow Saintonge et al. (2011a) and use a Milky Way value for $\alpha_{\rm CO}$ averaged over several recent measurements (Strong and Mattox 1996; Dame et al. 2001; Blitz et al. 2007; Draine et al. 2007; Heyer et al. 2009; Abdo et al. 2010), $\alpha_{\rm CO} = 3.2{\rm M}_\odot$(K km s^{-1} pc^2)$^{-1}$. Given the conversion factor, I can then compute the total H_2 mass following Solomon et al. (1997):

$$M_{\rm H_2} = L'_{\rm CO}\alpha_{\rm CO} = 3.25 \times 10^7 \alpha_{\rm CO} S_{\rm CO} \nu^{-2} d^2 \tag{A.17}$$

where $S_{\rm CO}$ is the total integrated CO flux in Jy km s^{-1} (which are our intensity map units) and ν is the rest frequency of the line in GHz, which for ^{12}CO(1-0) is 115.271 GHz. With this conversion made, the deprojected surface densities of H_2 can be calculated in a manner analogous to that of HI, depending on whether the galaxy is nearly face-on, inclined, or nearly edge-on.

Galaxies without CO Observations

The galaxies targeted for CARMA observations were specifically chosen to have the highest CO fluxes given their stellar masses and $u - r$ color (Saintonge et al. 2011a). Among those galaxies, NGC 5230 has the highest M_{H_2}/M_{HI} with ~ 0.4, meaning that while there is a significant H_2 mass in the galaxy, it is not the major contributor to the kinematics. Additionally, both the resolved CARMA observations and the CO single-dish observations of the HIghMass galaxies by Emmanouil Papastergis (Proposal PI: Amélie Saintonge) using the IRAM 30m telescope indicate that the HIghMass galaxies have typical molecular gas depletion timescales of approximately $t_{\rm dep} \equiv M_{H_2}/$ SFR $= 10^9$ yr (e.g. Leroy et al. 2008; Saintonge et al. 2011b). For the galaxies without direct CO observations, I infer that the H_2 in these galaxies makes up only $\sim 1 - 10\%$ of the total baryonic mass.

A.6.3 Stellar Masses

Compared to our global stellar mass estimates (Huang et al. 2012a; Huang et al. 2012b), finding from optical photometry a robust measure of how a galaxy's stellar mass distribution is more complex. Among other considerations, it requires an understanding of how the metallicity and extinction change with radius. However, our primary interest in a stellar mass density model is in determining its contribution to rotation curves in order to model each galaxy's dark matter content. Since the HIghMass galaxies have $M_{HI} \sim M_*$ and stellar mass is more concentrated towards the center of galaxies compared to the gas, the accuracy of the local stellar mass model is less important than the total stellar mass. To that end, we roughly approximate stellar mass using the following method: elliptical apertures are fit to the optical SDSS image and corrected for Galactic extinction. Internal extinction is

ignored because its variation with radius is unknown. Then, the magnitudes are converted into stellar masses using the the M_*/L_i and $g-r$ color relations and diet Salpeter initial mass function of Bell et al. (2003). The surface densities are deprojected by rescaling the stellar mass surface densities such that the total integrated mass is equal to the global value. This procedure assumes that the stars are distributed in a infinitely thin disk. I again stress that this method is not intended to give the most accurate distribution of stellar mass, but rather to give a rough estimate of where the bulk of the stellar mass is located.

A.6.4 Dark Matter

I use the GIPSY task ROTMAS to fit dark matter distributions to rotation curves. The ROTMOD task calculates the gaseous (HI, Helium, and, where detected, H_2) and stellar contributions to the galaxy rotation, assuming an infinitely thin disk for both. I find that varying models to allow for finite thickness of the stellar disk has little or no effect for the galaxies. The amplitude of rotation unaccounted for by the stellar and atomic gas components is ascribed to the dark matter:

$$V_{\rm obs}^2 = V_{\rm gas}^2 + V_*^2 + V_{\rm DM}^2 \tag{A.18}$$

I model two different spherically symmetric dark matter density profiles: the pseudo-isothermal model (ISO), an observationally motivated profile, and the Navarro-Frenk-White (NFW; Navarro et al. 1997) model, a theoretically motivated profile.

The Pseudo-Isothermal Model

Given that, at large radii, spiral galaxies are often observed to have flat, or very nearly flat rotation curves, the simplest observationally-motivated model is the pure isothermal model,

with a constant velocity profile:

$$V_{\rm DM}^{\rm P\text{-}ISO}(r) = V_\infty \tag{A.19}$$

and corresponding density profile:

$$\rho(r) = \frac{\rho_0}{(r/r_C)^2} \tag{A.20}$$

With ρ_0 being a reference density at some distance r_C. As I have the constraint that the velocity at all radii is V_∞, there is technically only one free parameter, either V_∞ or the product $\rho_0 \cdot r_C^2$, related by:

$$V_\infty = r_C\sqrt{4\pi G\rho_0} \tag{A.21}$$

However, the rotation curves of real galaxies are observed to go to 0 km s^{-1} at their center, and so the ISO model is a modification of the pure isothermal model to match observations, notably by adding a central core with constant density ρ_0:

$$\rho(r) = \frac{\rho_0}{1 + \left(\frac{r}{r_C}\right)^2} \tag{A.22}$$

with corresponding velocity profile

$$V_{\rm DM}^{\rm ISO}(r) = V_\infty\sqrt{\left[1 - \frac{R_C}{r}\arctan\left(\frac{r}{R_C}\right)\right]} \tag{A.23}$$

With V_∞ defined as in (A.21). Here, the velocity profile rises linearly near $r = 0$, and reaches V_∞ after several core scale lengths r_C. Because of the additional degree of freedom, the ISO model is a two-parameter model, with the free parameters generally chosen to be ρ_0 and r_C.

The Navarro-Frenk-White Model

The other profile I use is the Navarro-Frenk-White model (NFW; Navarro et al. 1997), which is motivated by distributions of ΛCDM halos observed in numerical simulations. It has a

density profile:

$$\rho(r) = \frac{\rho_i}{(r/r_s)\,(1 + r/r_s)^2} \tag{A.24}$$

Where ρ_i is a characteristic density, and r_s is a characteristic length scale of the halo. For convenience in writing the velocity form, I use the concentration parameter c instead of the characteristic density ρ_i, and the radius where the average halo density is 200 times the critical density R_{200} instead of the scale radius r_s when writing the velocity profile (Navarro et al. 1997):

$$V_{\rm DM}^{\rm NFW}(r) = V_{200}\sqrt{\frac{1}{x}\frac{\ln(1+cx) - cx/(1+cx)}{\ln(1+c) - c/(1+c)}} \tag{A.25}$$

where c is a parameter giving the central concentration of the halo; only $c > 1$ corresponds to physical models. $x \equiv r/R_{200}$, where R_{200} is a characteristic length scale. It produces a velocity curve which quickly rises to a maximum velocity at approximately $x \sim 2/c$, and then decreases slowly to 0 km s^{-1} at very large radii. V_{200} is defined as $V(R_{200})$ and is fixed for given c and R_{200}. The NFW profile is thus also a two-parameter family.

Comparison of the Two Models

One significant difference between the NFW and the ISO density models is that the is the presence of a central cusp ($\rho \propto r^{-\alpha}$) in the NFW profile and a core ($\rho \approx$ constant) in the ISO. While the NFW model is theoretically supported by ΛCDM cosmological simulations and the ISO model is not, in the literature it is observed that NFW profiles do a very poor job of fitting the rotation curves of both gas-rich dwarf galaxies (e.g. Weldrake et al. 2003; Salucci et al. 2003; Trachternach et al. 2008) and low surface brightness galaxies (LSB; e.g. McGaugh and de Blok 1998; Kuzio de Naray et al. 2008; Kuzio de Naray et al. 2009). For a recent review see de Blok (2010).

For our observations, typical beam sizes are ~ 3 kpc in size. Such poor resolution over

the inner few kpc of a galaxy has the effect of shallowing the rise of the rotation curve, and so prevents us from commenting on whether the very central region of the dark matter halo is a cusp or a central core. I can, however, still investigate the goodness of fit (χ^2) to both dark matter profile's overall fit to the rotation curve of each galaxy.

A.7 Stability and Star Formation Thresholds

I use three theoretical measures to investigate where star formation is expected to occur, in order to compare with our Hα imaging: the Toomre Q parameter (Toomre 1964), a threshold motivated by galactic shear (Hunter et al. 1998), and a model by Schaye (2004) designed to identify where in a galaxy a cold phase of HI can form. I also consider the gas surface densities at which HI becomes saturated and H_2 is observationally found to dominate over HI.

An oft-cited criterion for star formation is the Toomre Q parameter. For a thin, differentially rotating disk of pure gas or stars, the dynamics are dominated by pressure, self-gravity, and angular momentum. The gas is stable or unstable to radial (i.e. ring-like) perturbations for certain ranges of surface density and rotational velocities. The condition for stability is (Toomre 1964):

$$Q_g = \frac{\sigma_g \kappa}{\pi G \Sigma_g} \geq 1 \tag{A.26}$$

where σ_g is the velocity dispersion in the gas, G is Newton's gravitational constant, and Σ_g is the deprojected surface density of the gas. I take the gas velocity dispersion to be the constant $\sigma_g = 11$ km s^{-1} found by (Leroy et al. 2008) from their relatively face-on galaxies. Our galaxies both have $i > 60°$, making our own measurements of σ_g poor at best. κ is the

epicyclic frequency:

$$\kappa^2 = \frac{2\Omega}{r}\frac{d}{dr}\left(r^2\Omega\right) \tag{A.27}$$

where r is the distance from the center of the galaxy and $\Omega(r)$ is the angular speed at radius r.

Beyond just gas, one can define analogous Q_*, Q_{H_2} and so on for the various components of the disk. Many prescriptions exist for combining these various Q_i parameters into one effective Q. Perhaps the best known is the so-called Wang-Silk approximation, where the *instabilities* of the phases add linearly, or $Q^{-1} = Q_g^{-1} + Q_*^{-1}$ (Wang and Silk 1994). More rigorous prescriptions are given by Rafikov (2001), who take into account the wavenumber of such perturbations, as well as Romeo and Wiegert (2011) and refinements in Romeo and Falstad (2013) which weight each of the Q_i based on both the vertical and radial velocity dispersion of each component of the galactic disk. I have found, for each of these three prescriptions, that the Q_g term dominates for our galaxies, and so I approximate $Q \approx Q_g$. In particular, I rearrange Equation (A.26) to express the instability as a critical density above which the gas is unstable against inflow (Kennicutt 1989):

$$\Sigma_Q = \alpha_Q \frac{\sigma_g \kappa}{\pi G} \tag{A.28}$$

where α_Q is a dimensionless parameter equal to the average $\langle 1/Q \rangle$ where star formation occurs; again, $\alpha_Q = 1$ in the ideal case. Many tests of this parameter have been done in the literature, with the consensus being that star formation occurs in regions for which $\alpha_Q < 1$. As a few examples, Kennicutt (1989)[6] found $\alpha_Q = 0.63$, Martin and Kennicutt (2001) found $\alpha_Q = 0.69$, though they both assume $\sigma_g = 6$ km s^{-1}, which more closely matches the dispersion of the cold phase alone. Changing this assumption to our own $\sigma_g = 11$ km s^{-1} yields $\alpha_Q = 0.34$ and $\alpha_Q = 0.38$. Leroy et al. (2008) found $\alpha_Q \approx 0.4$ for their massive spiral

[6]They report that $\alpha_Q = 0.67$, but they have a slightly different definition of Σ_Q.

galaxies, using the same assumptions that I do. I choose $\alpha_Q = 0.4$ as a typical 'marginally unstable' threshold as observed in the literature. The deviation of α_Q from unity may be an indication that star formation can occur long before the gas is dense enough to cause axisymmetric inflow of the gas. Alternatively, other parameters, such as the presence of stars (e.g. Jog and Solomon 1984, Jog and Solomon 1992) have significant impacts on the stability. This discrepancy may also be due to using global properties, such as the rotation curve and averaged gas densities to predict star formation, which is ultimately a local process (e.g. Krumholz et al. 2012).

Hunter et al. (1998) take a different approach to star formation than large-scale collapse in the gaseous disk. They examine the case where the HI clouds lose angular momentum along magnetic field lines. In this case, the dominant effect preventing collapse becomes the shear in the disk. Schaye (2004) comes to a similar conclusion arguing that the shear timescale must be greater than the dynamical timescale for collapse to occur. This critical density can be expressed as:

$$\Sigma_A = \alpha_A \frac{\sigma_g A}{\pi G} \tag{A.29}$$

where α_A is an uncertain dimensionless parameter, similar to α_Q. A is Oort's A constant, defined as:

$$A = -0.5 r \frac{d}{dr}\Omega(r) \tag{A.30}$$

Hunter et al. (1998) chose $\alpha_A = 2.5$ based on a rough argument that perturbations must grow by a factor of 100 to be significant, while Schaye (2004) implies $\alpha_A = 1$ at the onset of instability. In a sample of 30 nearby spirals, Martin and Kennicutt (2001) suggest $\alpha_A = 2.0$. I use $\alpha_A = 2.5$ as a baseline for the maximum required surface density. Note that if in the outer disk of a galaxy the rotation curve is flat, as is the case with our sample, Σ_A reduces to a form identical to Σ_Q, up to choices of α_Q and α_A. They become equal for $\alpha_Q/\alpha_A = \pi/2\sqrt{2} \approx 1.11$.

A third approach to star formation, taken by Schaye (2004), is to instead consider the regions in the disk where a cold phase of gas and the production of H_2 can occur. This cold phase will have a lower velocity dispersion, 3 km $s^{-1} < \sigma_{\rm cold} < 6$ km s^{-1}, compared to that in the dominant warm phase, $\sigma_{\rm gas} = 11$ km s^{-1}, and such a phase has a Σ_Q and Σ_A correspondingly lower. Schaye (2004) derives criteria under which a cold phase can form. These criteria can be expressed as:

$$\Sigma_{\rm S04} \approx 6.1 \frac{\Sigma_{\rm gas}}{\Sigma_{\rm gas} + \Sigma_*} {\rm M}_\odot \ {\rm pc}^{-2} \tag{A.31}$$

for an assumed constant metallicity of 0.1 $Z_\odot$ and interstellar flux of ionizing photons 10^6 cm^{-2} s^{-1}.

Finally, it has long been observed that HI surface densities of $\sim 9 - 10$ $M_\odot$ pc^{-2} are 'saturated,' (e.g. Martin and Kennicutt 2001, Bigiel et al. 2008, Leroy et al. 2008) in the local universe, and densities exceeding this value are rarely observed; excess gas exists in the molecular phase. This does not appear to be a threshold for star formation, only a location where the star formation efficiency becomes roughly constant (Leroy et al. 2008).

BIBLIOGRAPHY

K. N. Abazajian, J. K. Adelman-McCarthy, M. A. Agüeros, S. S. Allam, C. Allende Prieto, D. An, K. S. J. Anderson, S. F. Anderson, J. Annis, N. A. Bahcall, and et al. The Seventh Data Release of the Sloan Digital Sky Survey. *ApJS*, 182:543, June 2009. doi: 10.1088/0067-0049/182/2/543.

A. A. Abdo, M. Ackermann, M. Ajello, L. Baldini, J. Ballet, G. Barbiellini, D. Bastieri, B. M. Baughman, K. Bechtol, R. Bellazzini, B. Berenji, E. D. Bloom, E. Bonamente, A. W. Borgland, J. Bregeon, A. Brez, M. Brigida, P. Bruel, T. H. Burnett, S. Buson, G. A. Caliandro, R. A. Cameron, P. A. Caraveo, J. M. Casandjian, C. Cecchi, Ö. Çelik, A. Chekhtman, C. C. Cheung, J. Chiang, S. Ciprini, R. Claus, J. Cohen-Tanugi, L. R. Cominsky, J. Conrad, C. D. Dermer, F. de Palma, S. W. Digel, E. d. C. e. Silva, P. S. Drell, R. Dubois, D. Dumora, C. Farnier, C. Favuzzi, S. J. Fegan, W. B. Focke, P. Fortin, M. Frailis, Y. Fukazawa, S. Funk, P. Fusco, F. Gargano, N. Gehrels, S. Germani, G. Giavitto, B. Giebels, N. Giglietto, F. Giordano, T. Glanzman, G. Godfrey, I. A. Grenier, M.-H. Grondin, J. E. Grove, L. Guillemot, S. Guiriec, A. K. Harding, M. Hayashida, D. Horan, R. E. Hughes, M. S. Jackson, G. Jóhannesson, A. S. Johnson, W. N. Johnson, T. Kamae, H. Katagiri, J. Kataoka, N. Kawai, M. Kerr, J. Knödlseder, M. Kuss, J. Lande, L. Latronico, M. Lemoine-Goumard, F. Longo, F. Loparco, B. Lott, M. N. Lovellette, P. Lubrano, A. Makeev, M. N. Mazziotta, J. E. McEnery, C. Meurer, P. F. Michelson, W. Mitthumsiri, T. Mizuno, C. Monte, M. E. Monzani, A. Morselli, I. V. Moskalenko, S. Murgia, P. L. Nolan, J. P. Norris, E. Nuss, T. Ohsugi, A. Okumura, N. Omodei, E. Orlando, J. F. Ormes, D. Paneque, V. Pelassa, M. Pepe, M. Pesce-Rollins, F. Piron, T. A. Porter, S. Rainò, R. Rando, M. Razzano, A. Reimer, O. Reimer, T. Reposeur, A. Y. Rodriguez, F. Ryde, H. F.-W. Sadrozinski, D. Sanchez, A. Sander, P. M. Saz Parkinson, C. Sgrò, E. J. Siskind, P. D. Smith, G. Spandre, P. Spinelli, J.-L. Starck, M. S. Strickman, A. W. Strong, D. J. Suson, H. Takahashi, T. Tanaka, J. B. Thayer, J. G. Thayer, D. J. Thompson, L. Tibaldo, D. F. Torres, G. Tosti, A. Tramacere, Y. Uchiyama, T. L. Usher, V. Vasileiou, N. Vilchez, V. Vitale, A. P. Waite, P. Wang, B. L. Winer, K. S. Wood, T. Ylinen, M. Ziegler, and Fermi/LAT Collaboration. Fermi Observations of Cassiopeia and Cepheus: Diffuse Gamma-ray Emission in the Outer Galaxy. *ApJ*, 710: 133–149, February 2010. doi: 10.1088/0004-637X/710/1/133.

E. A. K. Adams, R. Giovanelli, and M. P. Haynes. A Catalog of Ultra-compact High Velocity Clouds from the ALFALFA Survey: Local Group Galaxy Candidates? *ApJ*, 768:77, May 2013. doi: 10.1088/0004-637X/768/1/77.

N. Arimoto, Y. Sofue, and T. Tsujimoto. CO-to-H_2 Conversion Factor in Galaxies. *PASJ*, 48:275–284, April 1996. doi: 10.1093/pasj/48.2.275.

R. Auld, R. F. Minchin, J. I. Davies, B. Catinella, W. van Driel, P. A. Henning, S. Linder, E. Momjian, E. Muller, K. O'Neil, S. Sabatini, S. Schneider, G. Bothun, L. Cortese, M. Disney, G. L. Hoffman, M. Putman, J. L. Rosenberg, M. Baes, W. J. G. de Blok,

A. Boselli, E. Brinks, N. Brosch, J. Irwin, I. D. Karachentsev, V. A. Kilborn, B. Koribalski, and K. Spekkens. The Arecibo Galaxy Environment Survey: precursor observations of the NGC 628 group. *MNRAS*, 371:1617–1640, October 2006. doi: 10.1111/j.1365-2966.2006.10761.x.

D. G. Barnes, L. Staveley-Smith, W. J. G. de Blok, T. Oosterloo, I. M. Stewart, A. E. Wright, G. D. Banks, R. Bhathal, P. J. Boyce, M. R. Calabretta, M. J. Disney, M. J. Drinkwater, R. D. Ekers, K. C. Freeman, B. K. Gibson, A. J. Green, R. F. Haynes, P. te Lintel Hekkert, P. A. Henning, H. Jerjen, S. Juraszek, M. J. Kesteven, V. A. Kilborn, P. M. Knezek, B. Koribalski, R. C. Kraan-Korteweg, D. F. Malin, M. Marquarding, R. F. Minchin, J. R. Mould, R. M. Price, M. E. Putman, S. D. Ryder, E. M. Sadler, A. Schröder, F. Stootman, R. L. Webster, W. E. Wilson, and T. Ye. The HI Parkes All Sky Survey: southern observations, calibration and robust imaging. *MNRAS*, 322:486–498, April 2001. doi: 10.1046/j.1365-8711.2001.04102.x.

C. M. Baugh. A primer on hierarchical galaxy formation: the semi-analytical approach. *Reports on Progress in Physics*, 69:3101–3156, December 2006. doi: 10.1088/0034-4885/69/12/R02.

M. A. Beasley, A. J. Cenarro, J. Strader, and J. P. Brodie. Evidence for the Disky Origin of Luminous Virgo Dwarf Ellipticals from the Kinematics of Their Globular Cluster Systems. *AJ*, 137:5146–5153, June 2009. doi: 10.1088/0004-6256/137/6/5146.

K. G. Begeman. H I rotation curves of spiral galaxies. I - NGC 3198. *A&A*, 223:47–60, October 1989.

E. F. Bell, D. H. McIntosh, N. Katz, and M. D. Weinberg. The Optical and Near-Infrared Properties of Galaxies. I. Luminosity and Stellar Mass Functions. *ApJS*, 149:289–312, December 2003. doi: 10.1086/378847.

A. J. Benson. Galaxy formation theory. *Phys. Rep.*, 495:33–86, October 2010. doi: 10.1016/j.physrep.2010.06.001.

F. Bigiel, A. Leroy, F. Walter, E. Brinks, W. J. G. de Blok, B. Madore, and M. D. Thornley. The Star Formation Law in Nearby Galaxies on Sub-Kpc Scales. *AJ*, 136:2846–2871, December 2008. doi: 10.1088/0004-6256/136/6/2846.

B. Binggeli, A. Sandage, and G. A. Tammann. Studies of the Virgo Cluster. II - A catalog of 2096 galaxies in the Virgo Cluster area. *AJ*, 90:1681–1759, September 1985. doi: 10.1086/113874.

B. Binggeli, C. C. Popescu, and G. A. Tammann. The kinematics of the Virgo cluster revisited. *A&AS*, 98:275–296, April 1993.

J. Binney and S. Tremaine. *Galactic Dynamics: Second Edition*. Princeton University Press, 2008.

L. Blitz, Y. Fukui, A. Kawamura, A. Leroy, N. Mizuno, and E. Rosolowsky. Giant Molecular Clouds in Local Group Galaxies. *Protostars and Planets V*, pages 81–96, 2007.

H. Böhringer, U. G. Briel, R. A. Schwarz, W. Voges, G. Hartner, and J. Trümper. The structure of the Virgo cluster of galaxies from Rosat X-ray images. *Nature*, 368:828–831, April 1994. doi: 10.1038/368828a0.

S. Boissier and N. Prantzos. Chemo-spectrophotometric evolution of spiral galaxies - II. Main properties of present-day disc galaxies. *MNRAS*, 312:398–416, February 2000. doi: 10.1046/j.1365-8711.2000.03133.x.

A. Boselli and G. Gavazzi. Environmental Effects on Late-Type Galaxies in Nearby Clusters. *PASP*, 118:517–559, April 2006. doi: 10.1086/500691.

A. Boselli, L. Cortese, J. M. Deharveng, G. Gavazzi, K. S. Yi, A. Gil de Paz, M. Seibert, S. Boissier, J. Donas, Y.-W. Lee, B. F. Madore, D. C. Martin, R. M. Rich, and Y.-J. Sohn. UV Properties of Early-Type Galaxies in the Virgo Cluster. *ApJ*, 629:L29–L32, August 2005. doi: 10.1086/444534.

A. Boselli, S. Boissier, L. Cortese, and G. Gavazzi. The Origin of Dwarf Ellipticals in the Virgo Cluster. *ApJ*, 674:742–767, February 2008a. doi: 10.1086/525513.

A. Boselli, S. Boissier, L. Cortese, and G. Gavazzi. The origin of the $< \mu_e > -M_B$ and Kormendy relations in dwarf elliptical galaxies. *A&A*, 489:1015–1022, October 2008b. doi: 10.1051/0004-6361:200809546.

A. H. Broeils and M.-H. Rhee. Short 21-cm WSRT observations of spiral and irregular galaxies. HI properties. *A&A*, 324:877–887, August 1997.

G. Bruzual and S. Charlot. Stellar population synthesis at the resolution of 2003. *MNRAS*, 344:1000–1028, October 2003. doi: 10.1046/j.1365-8711.2003.06897.x.

D. Burstein, N. Krumm, and E. E. Salpeter. Neutral-hydrogen observations and maps of early-type galaxies. *AJ*, 94:883–898, October 1987. doi: 10.1086/114523.

N. Caldwell. Dwarf elliptical galaxies in the Fornax cluster. I - A catalog and luminosity function. *AJ*, 94:1116–1125, November 1987. doi: 10.1086/114549.

J. M. Cannon, R. Giovanelli, M. P. Haynes, S. Janowiecki, A. Parker, J. J. Salzer, E. A. K. Adams, E. Engstrom, S. Huang, K. B. W. McQuinn, J. Ott, A. Saintonge, E. D. Skillman, J. Allan, G. Erny, P. Fliss, and A. Smith. The Survey of H I in Extremely Low-mass Dwarfs (SHIELD). *ApJ*, 739:L22, September 2011. doi: 10.1088/2041-8205/739/1/L22.

B. Catinella, D. Schiminovich, G. Kauffmann, S. Fabello, J. Wang, C. Hummels, J. Lemonias, S. M. Moran, R. Wu, R. Giovanelli, M. P. Haynes, T. M. Heckman, A. R. Basu-Zych, M. R. Blanton, J. Brinchmann, T. Budavári, T. Gonçalves, B. D. Johnson, R. C. Kennicutt,

B. F. Madore, C. D. Martin, M. R. Rich, L. J. Tacconi, D. A. Thilker, V. Wild, and T. K. Wyder. The GALEX Arecibo SDSS Survey - I. Gas fraction scaling relations of massive galaxies and first data release. *MNRAS*, 403:683–708, April 2010. doi: 10.1111/j.1365-2966.2009.16180.x.

V. Cayatte, J. H. van Gorkom, C. Balkowski, and C. Kotanyi. VLA observations of neutral hydrogen in Virgo Cluster galaxies. I - The Atlas. *AJ*, 100:604–634, September 1990. doi: 10.1086/115545.

B. Cervantes-Sodi and X. Hernández. Chemical abundances and gas content in disk galaxies: correlations with the λ spin parameter. *Rev. Mexicana Astron. Astrofis.*, 45:75–84, April 2009.

G. Chabrier. Galactic Stellar and Substellar Initial Mass Function. *PASP*, 115:763–795, July 2003. doi: 10.1086/376392.

L. Chemin, C. Carignan, and T. Foster. H I Kinematics and Dynamics of Messier 31. *ApJ*, 705:1395–1415, November 2009. doi: 10.1088/0004-637X/705/2/1395.

L. Chemin, W. J. G. de Blok, and G. A. Mamon. Improved Modeling of the Mass Distribution of Disk Galaxies by the Einasto Halo Model. *AJ*, 142:109, October 2011. doi: 10.1088/0004-6256/142/4/109.

A. Chung, J. H. van Gorkom, J. D. P. Kenney, and B. Vollmer. Virgo Galaxies with Long One-sided H I Tails. *ApJ*, 659:L115–L119, April 2007. doi: 10.1086/518034.

A. Chung, J. H. van Gorkom, J. D. P. Kenney, H. Crowl, and B. Vollmer. VLA Imaging of Virgo Spirals in Atomic Gas (VIVA). I. The Atlas and the H I Properties. *AJ*, 138: 1741–1816, December 2009. doi: 10.1088/0004-6256/138/6/1741.

J. J. Condon, W. D. Cotton, E. W. Greisen, Q. F. Yin, R. A. Perley, G. B. Taylor, and J. J. Broderick. The NRAO VLA Sky Survey. *AJ*, 115:1693–1716, May 1998. doi: 10.1086/300337.

C. J. Conselice, J. S. Gallagher, III, and R. F. G. Wyse. Galaxy Populations and Evolution in Clusters. I. Dynamics and the Origin of Low-Mass Galaxies in the Virgo Cluster. *ApJ*, 559:791–811, October 2001. doi: 10.1086/322373.

C. J. Conselice, K. O'Neil, J. S. Gallagher, and R. F. G. Wyse. Galaxy Populations and Evolution in Clusters. IV. Deep H I Observations of Dwarf Elliptical Galaxies in the Virgo Cluster. *ApJ*, 591:167–184, July 2003. doi: 10.1086/375216.

E. Corbelli, S. Lorenzoni, R. Walterbos, R. Braun, and D. Thilker. A wide-field H I mosaic of Messier 31. II. The disk warp, rotation, and the dark matter halo. *A&A*, 511:A89, February 2010. doi: 10.1051/0004-6361/200913297.

T. J. Cornwell. Multiscale CLEAN Deconvolution of Radio Synthesis Images. *IEEE Journal of Selected Topics in Signal Processing*, 2:793–801, November 2008. doi: 10.1109/JSTSP.2008.2006388.

T. J. Cornwell, J. M. Uson, and N. Haddad. Radio-interferometric imaging of spectral lines - The problem of continuum subtraction. *A&A*, 258:583–590, May 1992.

L. Cortese and T. M. Hughes. Evolutionary paths to and from the red sequence: star formation and HI properties of transition galaxies at z ˜ 0. *MNRAS*, 400:1225–1240, December 2009. doi: 10.1111/j.1365-2966.2009.15548.x.

L. Cortese, B. Catinella, S. Boissier, A. Boselli, and S. Heinis. The effect of the environment on the H I scaling relations. *MNRAS*, 415:1797–1806, August 2011. doi: 10.1111/j.1365-2966.2011.18822.x.

L. L. Cowie and C. F. McKee. The evaporation of spherical clouds in a hot gas. I - Classical and saturated mass loss rates. *ApJ*, 211:135–146, January 1977. doi: 10.1086/154911.

L. L. Cowie and A. Songaila. Thermal evaporation of gas within galaxies by a hot intergalactic medium. *Nature*, 266:501–503, April 1977. doi: 10.1038/266501a0.

L. L. Cowie, A. Songaila, E. M. Hu, and J. G. Cohen. New Insight on Galaxy Formation and Evolution From Keck Spectroscopy of the Hawaii Deep Fields. *AJ*, 112:839, September 1996. doi: 10.1086/118058.

T. M. Dame, D. Hartmann, and P. Thaddeus. The Milky Way in Molecular Clouds: A New Complete CO Survey. *ApJ*, 547:792–813, February 2001. doi: 10.1086/318388.

J. Davies, R. Minchin, S. Sabatini, W. van Driel, M. Baes, P. Boyce, W. J. G. de Blok, M. Disney, R. Evans, V. Kilborn, R. Lang, S. Linder, S. Roberts, and R. Smith. A multibeam HI survey of the Virgo cluster - two isolated HI clouds? *MNRAS*, 349:922–932, April 2004. doi: 10.1111/j.1365-2966.2004.07568.x.

R. D. Davies and B. M. Lewis. Neutral hydrogen in Virgo cluster galaxies. *MNRAS*, 165: 231–244, 1973.

W. J. G. de Blok. The Core-Cusp Problem. *Advances in Astronomy*, 2010:789293, 2010. doi: 10.1155/2010/789293.

W. J. G. de Blok, F. Walter, E. Brinks, C. Trachternach, S.-H. Oh, and R. C. Kennicutt, Jr. High-Resolution Rotation Curves and Galaxy Mass Models from THINGS. *AJ*, 136: 2648, December 2008. doi: 10.1088/0004-6256/136/6/2648.

G. de Vaucouleurs. Structure of the Virgo Cluster of Galaxies. *ApJS*, 6:213, May 1961. doi: 10.1086/190064.

A. Dekel and J. Silk. The origin of dwarf galaxies, cold dark matter, and biased galaxy formation. *ApJ*, 303:39–55, April 1986. doi: 10.1086/164050.

S. di Serego Alighieri, G. Gavazzi, C. Giovanardi, R. Giovanelli, M. Grossi, M. P. Haynes, B. R. Kent, R. A. Koopmann, S. Pellegrini, M. Scodeggio, and G. Trinchieri. The HI content of early-type galaxies from the ALFALFA survey. I. Catalogued HI sources in the Virgo cluster. *A&A*, 474:851–855, November 2007. doi: 10.1051/0004-6361:20078205.

B. T. Draine, D. A. Dale, G. Bendo, K. D. Gordon, J. D. T. Smith, L. Armus, C. W. Engelbracht, G. Helou, R. C. Kennicutt, Jr., A. Li, H. Roussel, F. Walter, D. Calzetti, J. Moustakas, E. J. Murphy, G. H. Rieke, C. Bot, D. J. Hollenbach, K. Sheth, and H. I. Teplitz. Dust Masses, PAH Abundances, and Starlight Intensities in the SINGS Galaxy Sample. *ApJ*, 663:866–894, July 2007. doi: 10.1086/518306.

M. J. Drinkwater, M. D. Gregg, and M. Colless. Substructure and Dynamics of the Fornax Cluster. *ApJ*, 548:L139–L142, February 2001. doi: 10.1086/319113.

P.-A. Duc, J. Braine, U. Lisenfeld, E. Brinks, and M. Boquien. VCC 2062: an old tidal dwarf galaxy in the Virgo cluster? *A&A*, 475:187–197, November 2007. doi: 10.1051/0004-6361:20078335.

K. Duprie and S. E. Schneider. Neutral Hydrogen Around Early-Type Galaxies. *AJ*, 112: 937, September 1996. doi: 10.1086/118067.

J. Einasto. On the Construction of a Composite Model for the Galaxy and on the Determination of the System of Galactic Parameters. *Trudy Astrofizicheskogo Instituta Alma-Ata*, 5:87–100, 1965.

S. Fabello, B. Catinella, R. Giovanelli, G. Kauffmann, M. P. Haynes, T. M. Heckman, and D. Schiminovich. ALFALFA H I data stacking - I. Does the bulge quench ongoing star formation in early-type galaxies? *MNRAS*, 411:993–1012, February 2011. doi: 10.1111/j.1365-2966.2010.17742.x.

F. Fraternali and J. J. Binney. A dynamical model for the extraplanar gas in spiral galaxies. *MNRAS*, 366:449–466, February 2006. doi: 10.1111/j.1365-2966.2005.09816.x.

F. Fraternali and J. J. Binney. Accretion of gas on to nearby spiral galaxies. *MNRAS*, 386: 935–944, May 2008. doi: 10.1111/j.1365-2966.2008.13071.x.

C. Ftaclas, M. F. Struble, and M. N. Fanelli. Velocity distribution of Virgo Cluster galaxies. *ApJ*, 282:19–28, July 1984. doi: 10.1086/162172.

G. Gavazzi, A. Boselli, A. Donati, P. Franzetti, and M. Scodeggio. Introducing GOLDMine: A new galaxy database on the WEB. *A&A*, 400:451–455, March 2003. doi: 10.1051/0004-6361:20030026.

G. Gavazzi, A. Boselli, W. van Driel, and K. O'Neil. Completing H I observations of galaxies in the Virgo cluster. *A&A*, 429:439–447, January 2005. doi: 10.1051/0004-6361:20041678.

G. Gavazzi, R. Giovanelli, M. P. Haynes, S. Fabello, M. Fumagalli, B. R. Kent, R. A. Koopmann, N. Brosch, G. L. Hoffman, J. J. Salzer, and A. Boselli. HI content and other structural properties of galaxies in the Virgo cluster from the Arecibo Legacy Fast ALFA Survey. *A&A*, 482:43–52, April 2008. doi: 10.1051/0004-6361:200809382.

G. Gavazzi, M. Fumagalli, V. Galardo, F. Grossetti, A. Boselli, R. Giovanelli, M. P. Haynes, and S. Fabello. Hα3: an Hα imaging survey of HI selected galaxies from ALFALFA. I. Catalogue in the Local Supercluster. *A&A*, 545:A16, September 2012. doi: 10.1051/0004-6361/201218788.

G. Gavazzi, M. Fumagalli, M. Fossati, V. Galardo, F. Grossetti, A. Boselli, R. Giovanelli, and M. P. Haynes. Hα3: an Hα imaging survey of HI selected galaxies from ALFALFA. II. Star formation properties of galaxies in the Virgo cluster and surroundings. *A&A*, 553: A89, May 2013. doi: 10.1051/0004-6361/201218789.

H. Gerola, P. E. Seiden, and L. S. Schulman. Theory of dwarf galaxies. *ApJ*, 242:517–527, December 1980. doi: 10.1086/158485.

R. Giovanelli and M. P. Haynes. The H I extent and deficiency of spiral galaxies in the Virgo cluster. *AJ*, 88:881–908, July 1983. doi: 10.1086/113376.

R. Giovanelli, M. P. Haynes, B. R. Kent, P. Perillat, A. Saintonge, N. Brosch, B. Catinella, G. L. Hoffman, S. Stierwalt, K. Spekkens, M. S. Lerner, K. L. Masters, E. Momjian, J. L. Rosenberg, C. M. Springob, A. Boselli, V. Charmandaris, J. K. Darling, J. Davies, D. Garcia Lambas, G. Gavazzi, C. Giovanardi, E. Hardy, L. K. Hunt, A. Iovino, I. D. Karachentsev, V. E. Karachentseva, R. A. Koopmann, C. Marinoni, R. Minchin, E. Muller, M. Putman, C. Pantoja, J. J. Salzer, M. Scodeggio, E. Skillman, J. M. Solanes, C. Valotto, W. van Driel, and L. van Zee. The Arecibo Legacy Fast ALFA Survey. I. Science Goals, Survey Design, and Strategy. *AJ*, 130:2598–2612, December 2005. doi: 10.1086/497431.

R. Giovanelli, M. P. Haynes, B. R. Kent, A. Saintonge, S. Stierwalt, A. Altaf, T. Balonek, N. Brosch, S. Brown, B. Catinella, A. Furniss, J. Goldstein, G. L. Hoffman, R. A. Koopmann, D. A. Kornreich, B. Mahmood, A. M. Martin, K. L. Masters, A. Mitschang, E. Momjian, P. H. Nair, J. L. Rosenberg, and B. Walsh. The Arecibo Legacy Fast ALFA Survey. III. H I Source Catalog of the Northern Virgo Cluster Region. *AJ*, 133:2569–2583, June 2007. doi: 10.1086/516635.

R. Giovanelli, M. P. Haynes, E. A. K. Adams, J. M. Cannon, K. L. Rhode, J. J. Salzer, E. D. Skillman, E. Z. Bernstein-Cooper, and K. B. W. McQuinn. ALFALFA Discovery of the Nearby Gas-rich Dwarf Galaxy Leo P. I. H I Observations. *AJ*, 146:15, July 2013. doi: 10.1088/0004-6256/146/1/15.

M. Grossi, S. di Serego Alighieri, C. Giovanardi, G. Gavazzi, R. Giovanelli, M. P. Haynes, B. R. Kent, S. Pellegrini, S. Stierwalt, and G. Trinchieri. The Hi content of early-type galaxies from the ALFALFA survey. II. The case of low density environments. *A&A*, 498: 407–417, May 2009. doi: 10.1051/0004-6361/200810823.

J. E. Gunn and J. R. Gott, III. On the Infall of Matter Into Clusters of Galaxies and Some Effects on Their Evolution. *ApJ*, 176:1, August 1972. doi: 10.1086/151605.

G. Hallenbeck, E. Papastergis, S. Huang, M. P. Haynes, R. Giovanelli, A. Boselli, S. Boissier, S. Heinis, L. Cortese, and S. Fabello. Gas-bearing Early-type Dwarf Galaxies in Virgo: Evidence for Recent Accretion. *AJ*, 144:87, September 2012. doi: 10.1088/0004-6256/144/3/87.

G. Hallenbeck, S. Huang, K. Spekkens, M. P. Haynes, R. Giovanelli, E. A. K. Adams, J. Brinchmann, J. Chengalur, L. K. Hunt, K. L. Masters, and A. Saintonge. HIghMass - High HI Mass, HI-rich Galaxies at z˜0: High-Resolution VLA Imaging of UGC 9037 and UGC 12506. *ArXiv e-prints*, July 2014.

M. P. Haynes and R. Giovanelli. The pattern of H I deficiency in the Virgo cluster. *ApJ*, 306:466–482, July 1986. doi: 10.1086/164357.

M. P. Haynes, R. Giovanelli, J. J. Salzer, G. Wegner, W. Freudling, L. N. da Costa, T. Herter, and N. P. Vogt. The I-Band Tully-Fisher Relation for SC Galaxies: Optical Imaging Data. *AJ*, 117:1668–1687, April 1999. doi: 10.1086/300817.

M. P. Haynes, R. Giovanelli, and B. R. Kent. NGC 4254: An Act of Harassment Uncovered by the Arecibo Legacy Fast ALFA Survey. *ApJ*, 665:L19–L22, August 2007. doi: 10.1086/521188.

M. P. Haynes, R. Giovanelli, A. M. Martin, K. M. Hess, A. Saintonge, E. A. K. Adams, G. Hallenbeck, G. L. Hoffman, S. Huang, B. R. Kent, R. A. Koopmann, E. Papastergis, S. Stierwalt, T. J. Balonek, D. W. Craig, S. J. U. Higdon, D. A. Kornreich, J. R. Miller, A. A. O'Donoghue, R. P. Olowin, J. L. Rosenberg, K. Spekkens, P. Troischt, and E. M. Wilcots. The Arecibo Legacy Fast ALFA Survey: The α.40 H I Source Catalog, Its Characteristics and Their Impact on the Derivation of the H I Mass Function. *AJ*, 142: 170, November 2011. doi: 10.1088/0004-6256/142/5/170.

X. Hernandez, C. Park, B. Cervantes-Sodi, and Y.-Y. Choi. Empirical distributions of galactic λ spin parameters from the Sloan Digital Sky Survey. *MNRAS*, 375:163–170, February 2007. doi: 10.1111/j.1365-2966.2006.11274.x.

M. Heyer, C. Krawczyk, J. Duval, and J. M. Jackson. Re-Examining Larson's Scaling Relationships in Galactic Molecular Clouds. *ApJ*, 699:1092–1103, July 2009. doi: 10.1088/0004-637X/699/2/1092.

G. L. Hoffman, J. Glosson, G. Helou, E. E. Salpeter, and A. Sandage. H I detection survey of a complete magnitude-limited sample of dwarf irregular galaxies in the Virgo Cluster area. *ApJS*, 63:247–264, February 1987. doi: 10.1086/191164.

P. F. Hopkins, D. Kereš, and N. Murray. Accretion does not drive the turbulence in galactic discs. *MNRAS*, 432:2639–2646, July 2013. doi: 10.1093/mnras/stt472.

S. Huang, M. P. Haynes, R. Giovanelli, and J. Brinchmann. The Arecibo Legacy Fast ALFA Survey: The Galaxy Population Detected by ALFALFA. *ApJ*, 756:113, September 2012a. doi: 10.1088/0004-637X/756/2/113.

S. Huang, M. P. Haynes, R. Giovanelli, J. Brinchmann, S. Stierwalt, and S. G. Neff. Gas, Stars, and Star Formation in ALFALFA Dwarf Galaxies. *AJ*, 143:133, June 2012b. doi: 10.1088/0004-6256/143/6/133.

S. Huang, M. P. Haynes, R. Giovanelli, G. Hallenbeck, M. G. Jones, E. A. K. Adams, J. Brinchmann, J. Chengalur, L. K. Hunt, K. L. Masters, S. Matsushita, A. Saintonge, and K. Spekkens. HIghMass — High HI Mass, Gas-Rich Galaxies at z$\sim$0: Sample Definition, Optical and Hα Imaging, and Star Formation Properties. *ApJ*, 2014, in review.

W. K. Huchtmeier and O.-G. Richter. HI-observations of galaxies in the Virgo cluster of galaxies. I - The data. *A&AS*, 64:111–130, April 1986.

D. A. Hunter, B. G. Elmegreen, and A. L. Baker. The Relationship between Gas, Stars, and Star Formation in Irregular Galaxies: A Test of Simple Models. *ApJ*, 493:595–612, January 1998. doi: 10.1086/305158.

R. Jimenez, P. Padoan, F. Matteucci, and A. F. Heavens. Galaxy formation and evolution: low-surface-brightness galaxies. *MNRAS*, 299:123–138, August 1998. doi: 10.1046/j.1365-8711.1998.01731.x.

C. J. Jog and P. M. Solomon. A galactic disk as a two-fluid system - Consequences for the critical stellar velocity dispersion and the formation of condensations in the gas. *ApJ*, 276: 127–134, January 1984. doi: 10.1086/161598.

C. J. Jog and P. M. Solomon. A triggering mechanism for enhanced star formation in colliding galaxies. *ApJ*, 387:152–161, March 1992. doi: 10.1086/171067.

G. I. G. Józsa. Kinematic modelling of disk galaxies. II. A case-study of symmetrically warped galaxy disks. *A&A*, 468:903–917, June 2007. doi: 10.1051/0004-6361:20066165.

G. I. G. Józsa, F. Kenn, U. Klein, and T. A. Oosterloo. Kinematic modelling of disk galaxies. I. A new method to fit tilted rings to data cubes. *A&A*, 468:731–774, June 2007. doi: 10.1051/0004-6361:20066164.

R. C. Kennicutt, Jr. The star formation law in galactic disks. *ApJ*, 344:685–703, September 1989. doi: 10.1086/167834.

B. R. Kent, R. Giovanelli, M. P. Haynes, A. Saintonge, S. Stierwalt, T. Balonek, N. Brosch, B. Catinella, R. A. Koopmann, E. Momjian, and K. Spekkens. Optically Unseen H I Detections toward the Virgo Cluster Detected in the Arecibo Legacy Fast ALFA Survey. *ApJ*, 665:L15–L18, August 2007. doi: 10.1086/521100.

B. R. Kent, R. Giovanelli, M. P. Haynes, A. M. Martin, A. Saintonge, S. Stierwalt, T. J. Balonek, N. Brosch, and R. A. Koopmann. The Arecibo Legacy Fast Alfa Survey. VI. Second HI Source Catalog of the Virgo Cluster Region. *AJ*, 136:713–724, August 2008. doi: 10.1088/0004-6256/136/2/713.

B. R. Kent, K. Spekkens, R. Giovanelli, M. P. Haynes, E. Momjian, J. R. Cortés, E. Hardy, and A. A. West. The Arecibo Legacy Fast ALFA Survey. VII. A Neutral Hydrogen Cloud Complex in the Virgo Cluster. *ApJ*, 691:1595–1610, February 2009. doi: 10.1088/0004-637X/691/2/1595.

D. Kereš, N. Katz, D. H. Weinberg, and R. Davé. How do galaxies get their gas? *MNRAS*, 363:2–28, October 2005. doi: 10.1111/j.1365-2966.2005.09451.x.

S. Kim, S.-C. Rey, T. Lisker, and S. T. Sohn. Color-Magnitude Relations of Early-type Dwarf Galaxies in the Virgo Cluster: An Ultraviolet Perspective. *ApJ*, 721:L72–L77, September 2010. doi: 10.1088/2041-8205/721/1/L72.

M. R. Krumholz, A. Dekel, and C. F. McKee. A Universal, Local Star Formation Law in Galactic Clouds, nearby Galaxies, High-redshift Disks, and Starbursts. *ApJ*, 745:69, January 2012. doi: 10.1088/0004-637X/745/1/69.

R. Kuzio de Naray, S. S. McGaugh, and W. J. G. de Blok. Mass Models for Low Surface Brightness Galaxies with High-Resolution Optical Velocity Fields. *ApJ*, 676:920–943, April 2008. doi: 10.1086/527543.

R. Kuzio de Naray, S. S. McGaugh, and J. C. Mihos. Constraining the NFW Potential with Observations and Modeling of Low Surface Brightness Galaxy Velocity Fields. *ApJ*, 692: 1321–1332, February 2009. doi: 10.1088/0004-637X/692/2/1321.

R. Kuzio de Naray, C. A. Arsenault, K. Spekkens, J. A. Sellwood, M. McDonald, J. D. Simon, and P. Teuben. Searching for non-axisymmetries in NGC 6503: a weak end-on bar. *MNRAS*, 427:2523–2536, December 2012. doi: 10.1111/j.1365-2966.2012.22126.x.

R. B. Larson, B. M. Tinsley, and C. N. Caldwell. The evolution of disk galaxies and the origin of S0 galaxies. *ApJ*, 237:692–707, May 1980. doi: 10.1086/157917.

J. C. Lee, A. Gil de Paz, R. C. Kennicutt, Jr., M. Bothwell, J. Dalcanton, J. José G. Funes S., B. D. Johnson, S. Sakai, E. Skillman, C. Tremonti, and L. van Zee. A GALEX Ultraviolet Imaging Survey of Galaxies in the Local Volume. *ApJS*, 192:6, January 2011. doi: 10.1088/0067-0049/192/1/6.

A. K. Leroy, F. Walter, E. Brinks, F. Bigiel, W. J. G. de Blok, B. Madore, and M. D. Thornley. The Star Formation Efficiency in Nearby Galaxies: Measuring Where Gas Forms Stars Effectively. *AJ*, 136:2782–2845, December 2008. doi: 10.1088/0004-6256/136/6/2782.

D. N. C. Lin and S. M. Faber. Some implications of nonluminous matter in dwarf spheroidal galaxies. *ApJ*, 266:L21–L25, March 1983. doi: 10.1086/183971.

T. Lisker, K. Glatt, P. Westera, and E. K. Grebel. Virgo Cluster Early-Type Dwarf Galaxies with the Sloan Digital Sky Survey. II. Early-Type Dwarfs with Central Star Formation. *AJ*, 132:2432–2452, December 2006a. doi: 10.1086/508414.

T. Lisker, E. K. Grebel, and B. Binggeli. Virgo Cluster Early-Type Dwarf Galaxies with the Sloan Digital Sky Survey. I. On the Possible Disk Nature of Bright Early-Type Dwarfs. *AJ*, 132:497–513, August 2006b. doi: 10.1086/505045.

T. Lisker, E. K. Grebel, B. Binggeli, and K. Glatt. Virgo Cluster Early-Type Dwarf Galaxies with the Sloan Digital Sky Survey. III. Subpopulations: Distributions, Shapes, Origins. *ApJ*, 660:1186–1197, May 2007. doi: 10.1086/513090.

L. B. Lucy. An iterative technique for the rectification of observed distributions. *AJ*, 79: 745, June 1974. doi: 10.1086/111605.

A. V. Macciò, A. A. Dutton, F. C. van den Bosch, B. Moore, D. Potter, and J. Stadel. Concentration, spin and shape of dark matter haloes: scatter and the dependence on mass and environment. *MNRAS*, 378:55–71, June 2007. doi: 10.1111/j.1365-2966.2007.11720.x.

A. M. Martin, E. Papastergis, R. Giovanelli, M. P. Haynes, C. M. Springob, and S. Stierwalt. The Arecibo Legacy Fast ALFA Survey. X. The H I Mass Function and Ω_H I from the 40% ALFALFA Survey. *ApJ*, 723:1359–1374, November 2010. doi: 10.1088/0004-637X/723/2/1359.

C. L. Martin and R. C. Kennicutt, Jr. Star Formation Thresholds in Galactic Disks. *ApJ*, 555:301–321, July 2001. doi: 10.1086/321452.

M. L. Mateo. Dwarf Galaxies of the Local Group. *ARA&A*, 36:435–506, 1998. doi: 10.1146/annurev.astro.36.1.435.

L. Mayer, F. Governato, M. Colpi, B. Moore, T. Quinn, J. Wadsley, J. Stadel, and G. Lake. Tidal Stirring and the Origin of Dwarf Spheroidals in the Local Group. *ApJ*, 547:L123–L127, February 2001a. doi: 10.1086/318898.

L. Mayer, F. Governato, M. Colpi, B. Moore, T. Quinn, J. Wadsley, J. Stadel, and G. Lake. The Metamorphosis of Tidally Stirred Dwarf Galaxies. *ApJ*, 559:754–784, October 2001b. doi: 10.1086/322356.

S. S. McGaugh and W. J. G. de Blok. Testing the Dark Matter Hypothesis with Low Surface Brightness Galaxies and Other Evidence. *ApJ*, 499:41–65, May 1998. doi: 10.1086/305612.

K. B. W. McQuinn, E. D. Skillman, D. Berg, J. M. Cannon, J. J. Salzer, E. A. K. Adams, A. Dolphin, R. Giovanelli, M. P. Haynes, and K. L. Rhode. ALFALFA Discovery of the Nearby Gas-rich Dwarf Galaxy Leo P. IV. Distance Measurement from LBT Optical Imaging. *AJ*, 146:145, December 2013. doi: 10.1088/0004-6256/146/6/145.

K. B. W. McQuinn, J. M. Cannon, A. E. Dolphin, E. D. Skillman, J. J. Salzer, M. P. Haynes, E. Adams, I. Cave, E. C. Elson, R. Giovanelli, J. Ott, and A. Saintonge. Distance Determinations to SHIELD Galaxies from Hubble Space Telescope Imaging. *ApJ*, 785:3, April 2014. doi: 10.1088/0004-637X/785/1/3.

S. Mei, J. P. Blakeslee, P. Côté, J. L. Tonry, M. J. West, L. Ferrarese, A. Jordán, E. W. Peng, A. Anthony, and D. Merritt. The ACS Virgo Cluster Survey. XIII. SBF Distance Catalog and the Three-dimensional Structure of the Virgo Cluster. *ApJ*, 655:144–162, January 2007. doi: 10.1086/509598.

H. J. Mo, S. Mao, and S. D. M. White. The formation of galactic discs. *MNRAS*, 295: 319–336, April 1998. doi: 10.1046/j.1365-8711.1998.01227.x.

B. Moore. Evidence against dissipation-less dark matter from observations of galaxy haloes. *Nature*, 370:629–631, August 1994. doi: 10.1038/370629a0.

B. Moore, N. Katz, G. Lake, A. Dressler, and A. Oemler. Galaxy harassment and the evolution of clusters of galaxies. *Nature*, 379:613–616, February 1996. doi: 10.1038/379613a0.

J. F. Navarro, C. S. Frenk, and S. D. M. White. A Universal Density Profile from Hierarchical Clustering. *ApJ*, 490:493–508, December 1997.

J. F. Navarro, E. Hayashi, C. Power, A. R. Jenkins, C. S. Frenk, S. D. M. White, V. Springel, J. Stadel, and T. R. Quinn. The inner structure of ΛCDM haloes - III. Universality and asymptotic slopes. *MNRAS*, 349:1039–1051, April 2004. doi: 10.1111/j.1365-2966.2004.07586.x.

J. F. Navarro, A. Ludlow, V. Springel, J. Wang, M. Vogelsberger, S. D. M. White, A. Jenkins, C. S. Frenk, and A. Helmi. The diversity and similarity of simulated cold dark matter haloes. *MNRAS*, 402:21–34, February 2010. doi: 10.1111/j.1365-2966.2009.15878.x.

A. F. Neto, L. Gao, P. Bett, S. Cole, J. F. Navarro, C. S. Frenk, S. D. M. White, V. Springel, and A. Jenkins. The statistics of Λ CDM halo concentrations. *MNRAS*, 381:1450–1462, November 2007. doi: 10.1111/j.1365-2966.2007.12381.x.

B. D. Oppenheimer, R. Davé, D. Kereš, M. Fardal, N. Katz, J. A. Kollmeier, and D. H. Weinberg. Feedback and recycled wind accretion: assembling the z = 0 galaxy mass function. *MNRAS*, 406:2325–2338, August 2010. doi: 10.1111/j.1365-2966.2010.16872.x.

J. Ott, A. M. Stilp, S. R. Warren, E. D. Skillman, J. J. Dalcanton, F. Walter, W. J. G. de Blok, B. Koribalski, and A. A. West. VLA-ANGST: A High-resolution H I Survey of Nearby Dwarf Galaxies. *AJ*, 144:123, October 2012. doi: 10.1088/0004-6256/144/4/123.

E. Papastergis, A. M. Martin, R. Giovanelli, and M. P. Haynes. The Velocity Width Function of Galaxies from the 40% ALFALFA Survey: Shedding Light on the Cold Dark Matter Overabundance Problem. *ApJ*, 739:38, September 2011. doi: 10.1088/0004-637X/739/1/38.

E. Papastergis, A. Cattaneo, S. Huang, R. Giovanelli, and M. P. Haynes. A Direct Measurement of the Baryonic Mass Function of Galaxies and Implications for the Galactic Baryon Fraction. *ApJ*, 759:138, November 2012. doi: 10.1088/0004-637X/759/2/138.

E. Papastergis, R. Giovanelli, M. P. Haynes, A. Rodríguez-Puebla, and M. G. Jones. The Clustering of ALFALFA Galaxies: Dependence on H I Mass, Relationship with Optical Samples, and Clues of Host Halo Properties. *ApJ*, 776:43, October 2013. doi: 10.1088/0004-637X/776/1/43.

P. J. E. Peebles. Rotation of Galaxies and the Gravitational Instability Picture. *A&A*, 11: 377, April 1971.

R. R. Rafikov. The local axisymmetric instability criterion in a thin, rotating, multicomponent disc. *MNRAS*, 323:445–452, May 2001. doi: 10.1046/j.1365-8711.2001.04201.x.

K. L. Rhode, J. J. Salzer, N. C. Haurberg, A. Van Sistine, M. D. Young, M. P. Haynes, R. Giovanelli, J. M. Cannon, E. D. Skillman, K. B. W. McQuinn, and E. A. K. Adams. ALFALFA Discovery of the Nearby Gas-rich Dwarf Galaxy Leo P. II. Optical Imaging Observations. *AJ*, 145:149, June 2013. doi: 10.1088/0004-6256/145/6/149.

J. W. Rich, W. J. G. de Blok, T. J. Cornwell, E. Brinks, F. Walter, I. Bagetakos, and R. C. Kennicutt, Jr. Multi-Scale CLEAN: A Comparison of its Performance Against Classical CLEAN on Galaxies Using THINGS. *AJ*, 136:2897, December 2008. doi: 10.1088/0004-6256/136/6/2897.

A. B. Romeo and N. Falstad. A simple and accurate approximation for the Q stability parameter in multicomponent and realistically thick discs. *MNRAS*, 433:1389–1397, August 2013. doi: 10.1093/mnras/stt809.

A. B. Romeo and J. Wiegert. The effective stability parameter for two-component galactic discs: is $Q^{-1} \approx Q_{stars}^{-1} + Q_{gas}^{-1}$? *MNRAS*, 416:1191–1196, September 2011. doi: 10.1111/j.1365-2966.2011.19120.x.

J. L. Rosenberg and S. E. Schneider. The Arecibo Dual-Beam Survey: Arecibo and VLA Observations. *ApJS*, 130:177–199, September 2000. doi: 10.1086/317347.

A. Saintonge, R. Giovanelli, M. P. Haynes, G. L. Hoffman, B. R. Kent, A. M. Martin, S. Stierwalt, and N. Brosch. The Arecibo Legacy Fast Alfa Survey. V. The H I Source Catalog of the Anti-Virgo Region at $\delta = +27°$. *AJ*, 135:588, February 2008. doi: 10.1088/0004-6256/135/2/588.

A. Saintonge, G. Kauffmann, C. Kramer, L. J. Tacconi, C. Buchbender, B. Catinella, S. Fabello, J. Graciá-Carpio, J. Wang, L. Cortese, J. Fu, R. Genzel, R. Giovanelli, Q. Guo, M. P. Haynes, T. M. Heckman, M. R. Krumholz, J. Lemonias, C. Li, S. Moran, N. Rodriguez-Fernandez, D. Schiminovich, K. Schuster, and A. Sievers. COLD GASS, an IRAM legacy survey of molecular gas in massive galaxies - I. Relations between H_2, H I, stellar content and structural properties. *MNRAS*, 415:32–60, July 2011a. doi: 10.1111/j.1365-2966.2011.18677.x.

A. Saintonge, G. Kauffmann, J. Wang, C. Kramer, L. J. Tacconi, C. Buchbender, B. Catinella, J. Graciá-Carpio, L. Cortese, S. Fabello, J. Fu, R. Genzel, R. Giovanelli, Q. Guo, M. P. Haynes, T. M. Heckman, M. R. Krumholz, J. Lemonias, C. Li, S. Moran, N. Rodriguez-Fernandez, D. Schiminovich, K. Schuster, and A. Sievers. COLD GASS, an IRAM legacy survey of molecular gas in massive galaxies - II. The non-universality of the molecular gas depletion time-scale. *MNRAS*, 415:61–76, July 2011b. doi: 10.1111/j.1365-2966.2011.18823.x.

S. Salim, R. M. Rich, S. Charlot, J. Brinchmann, B. D. Johnson, D. Schiminovich, M. Seibert, R. Mallery, T. M. Heckman, K. Forster, P. G. Friedman, D. C. Martin, P. Morrissey, S. G. Neff, T. Small, T. K. Wyder, L. Bianchi, J. Donas, Y.-W. Lee, B. F. Madore, B. Milliard, A. S. Szalay, B. Y. Welsh, and S. K. Yi. UV Star Formation Rates in the Local Universe. *ApJS*, 173:267–292, December 2007. doi: 10.1086/519218.

P. Salucci, F. Walter, and A. Borriello. Lambda CDM and the distribution of dark matter in galaxies: A constant-density halo around DDO 47. *A&A*, 409:53–56, October 2003. doi: 10.1051/0004-6361:20030646.

R. Sancisi and R. J. Allen. Neutral hydrogen observations of the edge-on disk galaxy NGC 891. *A&A*, 74:73–84, April 1979.

R. Sancisi, F. Fraternali, T. Oosterloo, and T. van der Hulst. Cold gas accretion in galaxies. *A&A Rev.*, 15:189–223, June 2008. doi: 10.1007/s00159-008-0010-0.

C. L. Sarazin. X-ray emission from clusters of galaxies. *Reviews of Modern Physics*, 58: 1–115, January 1986. doi: 10.1103/RevModPhys.58.1.

R. J. Sault. An analysis of visibility-based continuum subtraction. *A&AS*, 107:55–69, October 1994.

J. Schaye. Star Formation Thresholds and Galaxy Edges: Why and Where. *ApJ*, 609: 667–682, July 2004. doi: 10.1086/421232.

D. J. Schlegel, D. P. Finkbeiner, and M. Davis. Maps of Dust Infrared Emission for Use in Estimation of Reddening and Cosmic Microwave Background Radiation Foregrounds. *ApJ*, 500:525–553, June 1998. doi: 10.1086/305772.

R. H. M. Schoenmakers, M. Franx, and P. T. de Zeeuw. Measuring non-axisymmetry in spiral galaxies. *MNRAS*, 292:349, December 1997.

J. A. Sellwood and R. Z. Sánchez. Quantifying non-circular streaming motions in disc galaxies. *MNRAS*, 404:1733–1744, June 2010. doi: 10.1111/j.1365-2966.2010.16430.x.

L. D. Shaw, J. Weller, J. P. Ostriker, and P. Bode. Statistics of Physical Properties of Dark Matter Clusters. *ApJ*, 646:815–833, August 2006. doi: 10.1086/505016.

J. Shen and J. A. Sellwood. Galactic warps induced by cosmic infall. *MNRAS*, 370:2–14, July 2006. doi: 10.1111/j.1365-2966.2006.10477.x.

E. D. Skillman, S. Côté, and B. W. Miller. Star Formation in Sculptor Group Dwarf Irregular Galaxies and the Nature of "Transition" Galaxies. *AJ*, 125:593–609, February 2003. doi: 10.1086/345964.

E. D. Skillman, J. J. Salzer, D. A. Berg, R. W. Pogge, N. C. Haurberg, J. M. Cannon, E. Aver, K. A. Olive, R. Giovanelli, M. P. Haynes, E. A. K. Adams, K. B. W. McQuinn, and K. L. Rhode. ALFALFA Discovery of the nearby Gas-rich Dwarf Galaxy Leo P. III. An Extremely Metal Deficient Galaxy. *AJ*, 146:3, July 2013. doi: 10.1088/0004-6256/146/1/3.

R. Smith, J. I. Davies, and A. H. Nelson. How effective is harassment on infalling late-type dwarfs? *MNRAS*, 405:1723–1735, July 2010. doi: 10.1111/j.1365-2966.2010.16545.x.

Y. Sofue and V. Rubin. Rotation Curves of Spiral Galaxies. *ARA&A*, 39:137–174, 2001. doi: 10.1146/annurev.astro.39.1.137.

P. M. Solomon, D. Downes, S. J. E. Radford, and J. W. Barrett. The Molecular Interstellar Medium in Ultraluminous Infrared Galaxies. *ApJ*, 478:144–161, March 1997.

K. Spekkens and J. A. Sellwood. Modeling Noncircular Motions in Disk Galaxies: Application to NGC 2976. *ApJ*, 664:204–214, July 2007. doi: 10.1086/518471.

C. M. Springob, M. P. Haynes, R. Giovanelli, and B. R. Kent. A Digital Archive of H I 21 Centimeter Line Spectra of Optically Targeted Galaxies. *ApJS*, 160:149–162, September 2005. doi: 10.1086/431550.

A. W. Strong and J. R. Mattox. Gradient model analysis of EGRET diffuse Galactic γ-ray emission. *A&A*, 308:L21–L24, April 1996.

R. Taylor, J. I. Davies, R. Auld, and R. F. Minchin. The Arecibo Galaxy Environment Survey - V. The Virgo cluster (I). *MNRAS*, 423:787–810, June 2012. doi: 10.1111/j.1365-2966.2012.20914.x.

R. Taylor, J. I. Davies, R. Auld, R. F. Minchin, and R. Smith. The Arecibo Galaxy Environment Survey - VI. The Virgo cluster (II). *MNRAS*, 428:459–469, January 2013. doi: 10.1093/mnras/sts042.

A. R. Thompson. Fundamentals of Radio Interferometry. In G. B. Taylor, C. L. Carilli, and R. A. Perley, editors, *Synthesis Imaging in Radio Astronomy II*, volume 180 of *Astronomical Society of the Pacific Conference Series*, page 11, 1999.

E. Toloba, A. Boselli, J. Gorgas, R. F. Peletier, A. J. Cenarro, D. A. Gadotti, A. Gil de Paz, S. Pedraz, and U. Yildiz. Kinematic Properties as Probes of the Evolution of Dwarf Galaxies in the Virgo Cluster. *ApJ*, 707:L17–L21, December 2009. doi: 10.1088/0004-637X/707/1/L17.

E. Toloba, A. Boselli, A. J. Cenarro, R. F. Peletier, J. Gorgas, A. Gil de Paz, and J. C. Muñoz-Mateos. Formation and evolution of dwarf early-type galaxies in the Virgo cluster. I. Internal kinematics. *A&A*, 526:A114, February 2011. doi: 10.1051/0004-6361/201015344.

A. Toomre. On the gravitational stability of a disk of stars. *ApJ*, 139:1217–1238, May 1964. doi: 10.1086/147861.

C. Trachternach, W. J. G. de Blok, F. Walter, E. Brinks, and R. C. Kennicutt, Jr. Dynamical Centers and Noncircular Motions in THINGS Galaxies: Implications for Dark Matter Halos. *AJ*, 136:2720, December 2008. doi: 10.1088/0004-6256/136/6/2720.

N. Trentham and R. B. Tully. Dwarf galaxies in the NGC 1023 Group. *MNRAS*, 398: 722–734, September 2009. doi: 10.1111/j.1365-2966.2009.15189.x.

R. B. Tully. The Local Supercluster. *ApJ*, 257:389–422, June 1982. doi: 10.1086/159999.

R. B. Tully and E. J. Shaya. Infall of galaxies into the Virgo cluster and some cosmological constraints. *ApJ*, 281:31–55, June 1984. doi: 10.1086/162073.

O. Urban, N. Werner, A. Simionescu, S. W. Allen, and H. Böhringer. X-ray spectroscopy of the Virgo Cluster out to the virial radius. *MNRAS*, 414:2101–2111, July 2011. doi: 10.1111/j.1365-2966.2011.18526.x.

R. P. van der Marel and M. Franx. A new method for the identification of non-Gaussian line profiles in elliptical galaxies. *ApJ*, 407:525–539, April 1993. doi: 10.1086/172534.

W. van Driel, D. Ragaigne, A. Boselli, J. Donas, and G. Gavazzi. H I observations of galaxies in the Virgo and Coma clusters. *A&AS*, 144:463–468, June 2000. doi: 10.1051/aas:2000220.

L. van Zee, E. D. Skillman, and M. P. Haynes. Rotationally Supported Virgo Cluster Dwarf Elliptical Galaxies: Stripped Dwarf Irregular Galaxies? *AJ*, 128:121–136, July 2004. doi: 10.1086/421368.

R. Verbeke, S. De Rijcke, M. Koleva, A. Cloet-Osselaer, B. Vandenbroucke, and J. Schroyen. Gaseous infall triggering starbursts in simulated dwarf galaxies. *ArXiv e-prints*, May 2014.

B. Vollmer, M. Soida, A. Chung, J. H. van Gorkom, K. Otmianowska-Mazur, R. Beck, M. Urbanik, and J. D. P. Kenney. Pre-peak ram pressure stripping in the Virgo cluster spiral galaxy NGC 4501. *A&A*, 483:89–106, May 2008. doi: 10.1051/0004-6361:20078139.

F. Walter, E. Brinks, W. J. G. de Blok, F. Bigiel, R. C. Kennicutt, Jr., M. D. Thornley, and A. Leroy. THINGS: The H I Nearby Galaxy Survey. *AJ*, 136:2563, December 2008. doi: 10.1088/0004-6256/136/6/2563.

B. Wang and J. Silk. Gravitational instability and disk star formation. *ApJ*, 427:759–769, June 1994. doi: 10.1086/174182.

J. Wang, G. Kauffmann, G. I. G. Józsa, P. Serra, T. van der Hulst, F. Bigiel, J. Brinchmann, M. A. W. Verheijen, T. Oosterloo, E. Wang, C. Li, M. den Heijer, and J. Kerp. The Bluedisks project, a study of unusually H I-rich galaxies - I. H I sizes and morphology. *MNRAS*, 433:270–294, July 2013. doi: 10.1093/mnras/stt722.

R. H. Warmels. The H I properties of spiral galaxies in the Virgo Cluster. I - Westerbork observations of 15 Virgo Cluster galaxies. II - One-dimensional Westerbork observations of 21 galaxies. *A&AS*, 72:19–87, January 1988.

L. H. Wei, S. J. Kannappan, S. N. Vogel, and A. J. Baker. Gas Mass Fractions and Star Formation in Blue-Sequence E/S0 Galaxies. *ApJ*, 708:841–861, January 2010. doi: 10.1088/0004-637X/708/1/841.

D. R. Weisz, J. J. Dalcanton, B. F. Williams, K. M. Gilbert, E. D. Skillman, A. C. Seth, A. E. Dolphin, K. B. W. McQuinn, S. M. Gogarten, J. Holtzman, K. Rosema, A. Cole, I. D. Karachentsev, and D. Zaritsky. The ACS Nearby Galaxy Survey Treasury. VIII. The Global Star Formation Histories of 60 Dwarf Galaxies in the Local Volume. *ApJ*, 739:5, September 2011. doi: 10.1088/0004-637X/739/1/5.

D. T. F. Weldrake, W. J. G. de Blok, and F. Walter. A high-resolution rotation curve of NGC 6822: a test-case for cold dark matter. *MNRAS*, 340:12–28, March 2003. doi: 10.1046/j.1365-8711.2003.06170.x.

C. D. Wilson. The Metallicity Dependence of the CO-to-H 2 Conversion Factor from Observations of Local Group Galaxies. *ApJ*, 448:L97, August 1995. doi: 10.1086/309615.

O. I. Wong, E. V. Ryan-Weber, D. A. Garcia-Appadoo, R. L. Webster, L. Staveley-Smith, M. A. Zwaan, M. J. Meyer, D. G. Barnes, V. A. Kilborn, R. Bhathal, W. J. G. de Blok, M. J. Disney, M. T. Doyle, M. J. Drinkwater, R. D. Ekers, K. C. Freeman, B. K. Gibson, S. Gurovich, J. Harnett, P. A. Henning, H. Jerjen, M. J. Kesteven, P. M. Knezek, B. S. Koribalski, S. Mader, M. Marquarding, R. F. Minchin, J. O'Brien, M. E. Putman, S. D. Ryder, E. M. Sadler, J. Stevens, I. M. Stewart, F. Stootman, and M. Waugh. The Northern HIPASS catalogue - data presentation, completeness and reliability measures. *MNRAS*, 371:1855–1864, October 2006. doi: 10.1111/j.1365-2966.2006.10846.x.

M. A. Zwaan, M. J. Meyer, L. Staveley-Smith, and R. L. Webster. The HIPASS catalogue: Ω_{HI} and environmental effects on the HI mass function of galaxies. *MNRAS*, 359:L30–L34, May 2005. doi: 10.1111/j.1745-3933.2005.00029.x.